Universität der Bundeswehr München
Fakultät für Luft- und Raumfahrttechnik
Institut für Thermodynamik

Numerical Investigation of the Hypersonic Laminar–Turbulent Boundary–Layer Transition around a Blunted Cone in CO_2, Mars and Earth Atmospheres

Fabian Teschner, M.Sc.

Vollständiger Abdruck der von der
Fakultät für Luft- und Raumfahrttechnik
der Universität der Bundeswehr München
zur Erlangung des akademischen Grades eines

Doktor-Ingenieurs (Dr.-Ing.)

genehmigten Dissertation

Vorsitzender:	Univ.–Prof. Dr. rer. nat. Matthias Gerdts
1. Berichterstatter:	Univ.–Prof. Dr.–Ing. Christian Mundt
2. Berichterstatter:	Apl. Prof. Dr.–Ing. Ulrich Rist
3. Berichterstatter:	Univ.–Prof. Dr.–Ing. habil. Markus Klein

Die Dissertation wurde am 05.10.2022 bei der Universität der Bundeswehr München eingereicht und durch die Fakultät für Luft- und Raumfahrttechnik am 03.04.2023 angenommen.

Tag der Prüfung: 12.05.2023

Preface

Die Ihnen hier vorliegende Forschungsarbeit ist in meiner Zeit als wissenschaftlicher Mitarbeiter am Institut für Thermodynamik an der Universität der Bundeswehr München entstanden. Als erstes gilt mein Dank meinem Doktorvater und Betreuer während dieser Zeit Herrn Univ.–Prof. Dr.–Ing. Christian Mundt, welcher mir die Möglichkeit zur Durchführung meines Promotionsvorhabens gegeben hat und welcher die gesamte Arbeit betreut hat und mir bei fachlichen Fragen behilflich war. Weiterhin möchte ich mich auch bei Herrn Apl. Prof. Dr.–Ing. Ulrich Rist und Herrn Univ.–Prof. Dr.–Ing. habil. Markus Klein für die Übernahme des Koreferats und Herrn Univ.–Prof. Dr. rer. nat. Matthias Gerdts für die Übernahme des Prüfungsvorsitzes ganz herzlich bedanken.

Des Weiteren gilt mein Dank Munich Aerospace e.V., welcher Teile meiner Forschungszeit mit einem Stipendium im Rahmen des Forschungsprojekts "Optimierung des Wiedereintritts zur Minimierung der Aufheizung oder der Infrarotsignatur" finanziell unterstützt hat.

Die Zeit am Institut war eine fordernde aber auch sehr schöne Zeit. Einen nicht geringen Anteil an der schönen Zeit hatten die Mitarbeiter des Instituts, weshalb ich mich bei allen bedanken möchte. Ein besonderer Dank geht an Axel Buck und an Christoph Traxinger, welche mir in den vergangenen Jahren bei vielen Fragestellungen hinsichtlich der Implementierung der Löser behilflich waren. Auch bedanken möchte ich mich bei Prof. Dr.-Ing. habil. Tobias Sander, welcher immer ein offenes Ohr hatte, wenn ich vor Schwierigkeiten in der Forschungsarbeit stand. Neben den fachlichen Gesprächen möchte ich mich bei den aktuellen und ehemaligen Kollegen für die tolle Zeit am Institut und besonders auch abseits der Arbeit bedanken. Es haben sich während der Zeit am Institut sehr gute Freundschaften entwickelt. Mein Dank gilt hier besonders Matthias Banholzer, Julian Zips, Christoph Traxinger, Jannis Bonin, Marco Vietze, Axel Buck und Marvin Feike.

Ganz besonders möchte ich mich bei meiner gesamten Familie bedanken. Liebe Mama und lieber Papa, euch gilt ein besonderer Dank, da ihr mir zu jeder Zeit mit einem offenen Ohr und mit jeglicher Unterstützung zur Seite standet. Ohne eure Unterstützung wäre diese Arbeit nicht möglich gewesen!

Zu guter Letzt möchte ich mich bei meiner Partnerin Julia bedanken, die mir mit ihrer Unterstützung und ihren motivierenden Worten zur Seite stand.

München, 29.05.2023

Abstract

In this work, the boundary–layer stability of a blunted cone in different atmospheres and under different free–stream Reynolds numbers will be investigated to examine the influence of the Mars atmosphere on the laminar–turbulent transition. Therefore, a blunted cone, experimentally investigated in a pure CO_2 atmosphere to measure the wall heat flux distribution, was chosen from literature and the linear stability theory and the linear parabolized stability equations were applied for the investigations. To perform the investigations, firstly, a new Navier–Stokes solver, named CONSST3D, to calculate the laminar base–flow solution and a new boundary–layer stability solver, named COSTAS, were developed and will be presented in this work containing the governing equations, the thermodynamic models and the numerical implementation. To validate the two solvers for the perfect gas and the thermo–chemical equilibrium gas regime, calculations were performed for the Stetson Mach 8 blunted cone and a Mach 10 flat plate, respectively. With the successfully validated solvers, the boundary–layer stability calculations were performed for the blunted cone in a pure CO_2 atmosphere, in the Mars atmosphere and in the Earth atmosphere requiring similar free–stream conditions to examine the influence of the atmosphere on the laminar–turbulent transition and to get first insights in the boundary–layer stability of a blunted cone in the Mars atmosphere. The results showed a destabilizing effect of the CO_2 atmosphere and the Mars atmosphere compared to the Earth atmosphere by applying a thermo–chemical equilibrium gas model. Further, the transition onset N–factor was found to be in the typical range of values at the transition onset location for the test case in the CO_2 atmosphere. The comparison with the calculation in the Mars atmosphere showed only small differences in the boundary–layer stability and thus, test campaigns in a pure CO_2 atmosphere were found to be a good approximation of the Mars atmosphere which contain a small additional amount of N_2. Overall, in comparison to the calculations in the Earth atmosphere, higher growth rates and higher N–factors were found in the CO_2 and Mars atmospheres at lower disturbance frequencies. An additional calculation was performed in the CO_2 atmosphere at a different free–stream condition, where the Reynolds number was significantly higher compared to the previous test case. In this case, the results showed a significantly higher N–factor at the transition onset location, which is located further upstream compared to the lower free–stream condition test case.

Kurzfassung

In dieser Arbeit wird die Grenzschichtstabilität eines stumpfen Kegels in verschiedenen Atmosphären und unter verschiedenen Anströmreynoldszahlen untersucht, um den Einfluss der Marsatmosphäre auf die laminar–turbulente Transition zu untersuchen. Hierfür wurde ein stumpfer Kegel aus der Literatur ausgewählt, welcher experimentell in einer CO_2–Atmosphäre untersucht wurde, um die Wandwärmestromverteilung zu messen, und die lineare Stabilitätstheorie und die linearen parabolisierten Stabilitätsgleichungen wurden für die Untersuchungen angewendet. Um die Untersuchungen durchzuführen, wurde zunächst ein neuer Navier–Stokes Löser, CONSST3D genannt, entwickelt, um die laminare Basislösung zu berechnen, und zusätzlich ein neuer Grenzschichtstabilitätslöser, COSTAS genannt, welche in dieser Arbeit hinsichtlich der zu lösenden Gleichungen, der thermodynamischen Modelle und der numerischen Implementierung vorgestellt werden. Um die beiden Löser für den Bereich des perfekten Gases und des Gases im thermo–chemischen Gleichgewicht zu validieren, wurden Berechnungen anhand des Stetson Mach 8 Kegels und einer Mach 10 ebenen Platte durchgeführt. Mit den erfolgreich validierten Lösern wurden die Grenzschichtstabilitätsberechnungen für den stumpfen Kegel in einer reinen CO_2–Atmosphäre, in der Marsatmosphäre und in der Erdatmosphäre durchgeführt, wobei ähnliche Anströmbedingungen gefordert wurden, um den Einfluss der Atmosphäre auf die laminar–turbulente Transition zu untersuchen und um erste Einblicke in die Grenzschichtstabilität eines stumpfen Kegels in der Marsatmosphäre zu sammeln. Die Ergebnisse zeigten einen destabilisierenden Effekt der CO_2–Atmosphäre und der Marsatmosphäre im Vergleich zu der Erdatmosphäre unter Verwendung eines Gasmodels im thermo–chemischen Gleichgewicht. Weiterhin wurde der N–Faktor an der Stelle des Beginns der Transition für den Testfall in der CO_2–Atmosphäre im typischen Bereich ermittelt. Der Vergleich mit der Berechnung in der Marsatmosphäre zeigte nur kleine Unterschiede in der Grenzschichtstabilität, wodurch gezeigt wurde, dass Testkampagnen in einer reinen CO_2–Atmosphäre eine gute Näherung für die Marsatmosphäre mit einem kleinen zusätzlichen Anteil an N_2 sind. Insgesamt wurden im Vergleich zu den Berechnungen in der Erdatmosphäre höhere Wachstumsraten und N–Faktoren bei kleineren Störungsfrequenzen in der CO_2–Atmosphäre und der Marsatmosphäre ermittelt. Eine zusätzliche Berechnung wurde bei höheren Anströmbedingungen in der CO_2–Atmosphäre durchgeführt, wobei die Reynoldszahl signifikant höher war als im vorherigen Testfall. In diesem Fall zeigten die Ergebnisse einen signifikant höheren N–Faktor an der Stelle des Beginns der Transition, welcher weiter stromauf lag als im Testfall mit den niedrigeren Anströmbedingungen.

Contents

List of Figures

List of Tables

Nomenclature

Unless otherwise specified, SI units are used in this work. Thus, the nomenclature does not contain the variable units.

Latin symbols

$\boldsymbol{A}$	Streamwise inviscid flux Jacobian
$\boldsymbol{A_v}$	Streamwise viscous flux Jacobian
$\boldsymbol{A_{x^1}}$	Base–flow matrix of disturbance equations containing x^1 derivatives
A	Disturbance amplitude
A_0	Initial disturbance amplitude
a, b	Coefficients for boundary–layer stability grid distribution
a_0, a_1, a_2, $a_{l,i}$	Coefficients for surface fitting method
$\boldsymbol{B}$	Spanwise inviscid flux Jacobian
$\boldsymbol{B_v}$	Spanwise viscous flux Jacobian
$\boldsymbol{B_{x^2}}$	Base–flow matrix of disturbance equations containing x^2 derivatives
$\boldsymbol{B^+_{x^2}}$	Positive normal base–flow matrix of disturbance equations
$\boldsymbol{b_\zeta}$	Normal NSCBC source vector
$\boldsymbol{C}$	Normal inviscid flux Jacobian
$\boldsymbol{C_v}$	Normal viscous flux Jacobian
$\boldsymbol{C_{x^3}}$	Base–flow matrix of disturbance equations containing x^3 derivatives
c	Speed of sound
c_0, c_1, c_2, c_3, c_4	State surface interpolation coefficients
c_0, c_j, c_k, $c_{j_{\max}}$	Coefficients for Chebyshev spectral collocation method
c_p	Specific heat capacity
c_{RK}	Runge–Kutta stage coefficients
c_r	Phase speed
c_s	Speed of sound in discretization direction
$\boldsymbol{D}$	Diagonal matrix
$\boldsymbol{D_0}$	Base–flow matrix of disturbance equations containing remaining terms
$\boldsymbol{d_\zeta}$	Normal NSCBC characteristic vector
$\boldsymbol{E}$	Streamwise inviscid flux vector
$\boldsymbol{E_{\mathrm{Cheb}}}$	Chebyshev spectral collocation method discretization matrix of first derivative
$\boldsymbol{E_v}$	Streamwise viscous flux vector
E	Disturbance kinetic energy

e	Total energy per unit volume
$\boldsymbol{F}$	Spanwise inviscid flux vector
$\boldsymbol{F_v}$	Spanwise viscous flux vector
f	Frequency
f_p	Pressure function coefficient
f_p^{AUSM}	Pressure based weight function
$\boldsymbol{G}$	Normal inviscid flux vector
$\boldsymbol{G_{\text{Cheb}}}$	Chebyshev spectral collocation method discretization matrix of second derivative
$\boldsymbol{G_v}$	Normal viscous flux vector
$\sqrt{g}$	Metric determinant
g_{km}	Covariant metric tensor
g^{km}	Contravariant metric tensor
$\boldsymbol{H}$	Eigenvalue problem matrix containing remaining terms
$\boldsymbol{H_{x^2}}$	Eigenvalue problem matrix containing x^2 terms
$\boldsymbol{H_{x^2x^2}}$	Eigenvalue problem matrix containing x^2x^2 terms
$\boldsymbol{H_\alpha}$	Eigenvalue problem matrix containing α terms
$\boldsymbol{H_{\alpha x^2}}$	Eigenvalue problem matrix containing αx^2 terms
$\boldsymbol{H_{\alpha\alpha}}$	Eigenvalue problem matrix containing α^2 terms
H_t	Total enthalpy
h	Enthalpy
h_i	Coefficient for the stretching function
$\boldsymbol{I}$	Identity matrix
Imag()	Imaginary part of complex number
J^{-1}	Determinant of the metric Jacobian
$\boldsymbol{k_\zeta}$	Normal NSCBC metric derivative vector
$\boldsymbol{L}$	Lower triangular matrix
$\boldsymbol{L_\zeta}$	Normal wave amplitude vector
$\boldsymbol{L_\Lambda}$	Left eigenvector of normal base–flow matrix of disturbance equations
L	Length
$\boldsymbol{M}^{-1}$	Matrix describing the derivative of the primitive variables with respect to the conservative variables
$\hat{\text{M}}$	AUSM split Mach number
$\boldsymbol{m}$	AUSM numerical convective flux vector
N	N–factor
n	Normal coordinate
n_s	Shock distance
P	AUSM split pressure
$\boldsymbol{p}$	AUSM numerical pressure flux vector
p	Pressure
p_s	Pressure function
$\boldsymbol{Q}$	Conservative state vector
$\boldsymbol{Q^F}$	Conservative state vector from forward sweep
Q	Heat flux

$\boldsymbol{q}$	Primitive state vector
Res	Residuum vector
R	Specific gas constant
Real()	Real part of complex number
R_1, R_2	Distances for overset mesh generation
R_N	Nose radius
R_c	Radius of curvature of bow shock
r	Ratio of gradients
$r_{l,i}$	Distance for surface fitting method
s	Arclength
$\boldsymbol{T_t}$	Base–flow matrix of disturbance equations containing time derivatives
T	Temperature
T_0	Sutherland reference temperature
T_s	Sutherland temperature
t	time
$\boldsymbol{U}$	Upper triangular matrix
u	Velocity component in x–direction
$\boldsymbol{V_{x^1x^1}}$	Base–flow matrix of disturbance equations containing x^1x^1 derivatives
$\boldsymbol{V_{x^2x^2}}$	Base–flow matrix of disturbance equations containing x^2x^2 derivatives
$\boldsymbol{V_{x^3x^3}}$	Base–flow matrix of disturbance equations containing x^3x^3 derivatives
$\boldsymbol{V_{x^1x^2}}$	Base–flow matrix of disturbance equations containing x^1x^2 derivatives
$\boldsymbol{V_{x^1x^3}}$	Base–flow matrix of disturbance equations containing x^1x^3 derivatives
$\boldsymbol{V_{x^2x^3}}$	Base–flow matrix of disturbance equations containing x^2x^3 derivatives
V	Absolute velocity
v	Velocity component in y–direction
v_n	Physical normal velocity component
v_t	Physical streamwise velocity component
v_ζ	Computational normal velocity component
v_η	Computational spanwise velocity component
v_ξ	Computational streamwise velocity component
v^1	Computational contravariant streamwise velocity component
v^2	Computational contravariant normal velocity component
v^3	Computational contravariant spanwise velocity component
w	Velocity component in z–direction
x	x–coordinate
x_a	Axial distance from the virtual sharp nose
x_n	Physical normal distance

x_ζ	Derivative of x–coordinate with respect to computational normal coordinate
x_η	Derivative of x–coordinate with respect to computational spanwise coordinate
x_ξ	Derivative of x–coordinate with respect to computational streamwise coordinate
x^1	Computational contravariant streamwise coordinate
x^2	Computational contravariant normal coordinate
x^3	Computational contravariant spanwise coordinate
y	y-coordinate
y_ζ	Derivative of y–coordinate with respect to computational normal coordinate
y_η	Derivative of y–coordinate with respect to computational spanwise coordinate
y_ξ	Derivative of y–coordinate with respect to computational streamwise coordinate
z	z–coordinate
z_ζ	Derivative of z–coordinate with respect to computational normal coordinate
z_η	Derivative of z–coordinate with respect to computational spanwise coordinate
z_ξ	Derivative of z–coordinate with respect to computational streamwise coordinate

Greek symbols

α	Physical streamwise wave–number
β	Physical spanwise wave–number
β_s	Stretching factor
Γ^k_{mo}	Christoffel symbol of the second kind
γ	Heat capacity ratio
Δ	Difference
Δ_s	Shock standoff distance
δ	Boundary–layer thickness
$\boldsymbol{\delta}^l_m$	Kronecker tensor
ϵ	Internal energy
ϵ_{rad}	Emissivity coefficient
$\boldsymbol{\xi}$	Streamwise metric vector
ζ	Computational normal coordinate
ζ_x	Derivative of computational normal coordinate with respect to x–coordinate
ζ_y	Derivative of computational normal coordinate with respect to y–coordinate
ζ_z	Derivative of computational normal coordinate with respect to z–

	coordinate
η	Computational spanwise coordinate
η_x	Derivative of computational spanwise coordinate with respect to x–coordinate
η_y	Derivative of computational spanwise coordinate with respect to y–coordinate
η_z	Derivative of computational spanwise coordinate with respect to z–coordinate
Θ	Cone half angle
κ	Thermal conductivity
$\mathbf{\Lambda}^+$	Positive eigenvalue matrix of normal base–flow matrix of disturbance equations
$\boldsymbol{\lambda_\zeta}$	Normal eigenvalue vector
λ	Eigenvalue
λ_s	Second viscosity coefficient
λ_ζ	Normal eigenvalue
λ_η	Spanwise eigenvalue
λ_ξ	Streamwise eigenvalue
μ	Dynamic viscosity
μ_0	Sutherland reference viscosity
ξ	Computational streamwise coordinate
ξ_x	Derivative of computational streamwise coordinate with respect to x–coordinate
ξ_y	Derivative of computational streamwise coordinate with respect to y–coordinate
ξ_z	Derivative of computational streamwise coordinate with respect to z–coordinate
ρ	Density
σ	Growth rate
σ_{SB}	Stefan–Boltzmann constant
Φ	Phase function
ϕ	Limiter function
φ	Geometrical angle
Ψ	Stretching function
ω	Angular frequency
ω^{AUSM}	Pressure based weight function

Dimensionless numbers

CFL	Courant–Friedrichs–Lewy number
M	Mach number
M_{x^1}	Streamwise Mach number
Ec	Eckert number
Pr	Prandtl number

Re	Reynolds number
St	Stanton number
Re_{∞,R_N}	Reynolds number with respect to free–stream and nose radius
$\mathrm{Re}_{\mathrm{trans},\infty,s}$	Transition Reynolds number with respect to free–stream and arclength
Re_x	Local Reynolds number

Abbreviations

CEA	Chemical Equilibrium with Applications
CONSST3D	COmpressible Navier–Stokes STeady 3D
COSTAS	COmpressible STAbility Solver
AUSM	Advection Upstream Splitting Method
c.c.	Complex conjugate
DNS	Direct Numerical Simulation
DPLR	Data-Parallel Line Relaxation
LAPACK	Linear Algebra PACKage
LAURA	Langley Upwind Aerothermodynamic Relaxation Algorithm
LPSE	Linear Parabolized Stability Equations
LST	Linear Stability Theory
LU–SGS	Lower–Upper Symmetric–Gauß–Seidel
MUSCL	Monotonic Upstream-Centered Scheme for Conservation Laws
NASA	National Aeronautics and Space Administration
NSCBC	Navier–Stokes Characteristic Boundary Conditions
PG	Perfect Gas
PSE	Parabolized Stability Equations
TCE	Thermo–Chemical Equilibrium
TPS	Thermal Protection Shield
TVD	Total Variation Diminishing

Subscripts

∞	Free–stream variable
,	Covariant derivative
cart	Cartesian
eq	Thermo–chemical equilibrium
i	Grid point number in streamwise direction
j	Grid point number in normal direction
k,m,o,p,r	Indices
L	Left flux vector
l	Grid point number in spanwise direction
max	Maximum value
n	normal direction
new	New variable

old	Old variable
R	Right flux vector
trans	Transition
w	Wall
δ	Boundary–layer edge

Superscripts

$*$	Dimensional variable
$+$	Positive flux vector
$-$	Negative flux vector
$\dagger$	Complex conjugate
k,m,o,p,r	Indices
S	Shock variable

Accents

$'$	Disturbance variable
$\bar{}$	Base–flow variable
$\tilde{}$	Amplitude function of disturbance variable

Chapter 1

Introduction

1.1 Motivation

In the mission planning and the design phase of re–entry maneuvers, the investigation, evaluation and optimization of the laminar–turbulent transition have become crucial design criteria over the last decades, especially with regard to the development and design of the thermal protection shield (TPS). The main reason for the necessity of investigations with regard to the laminar–turbulent transition is the difference in the wall heat flux in a turbulent flow compared to a laminar one, where, in the turbulent flow, the wall heat flux is significantly, respectively, several times, higher compared to the wall heat flux in a laminar flow, see, e.g., [2]. Re–entry maneuvers into the atmospheres of different planets usually take place at high speeds which are in the order of several times the speed of sound. These high velocities result in a discontinuity in the flow, namely, a bow shock, that forms in front of the geometry. Across the bow shock, the flow–field changes significantly, e.g., the velocity decreases and the pressure and temperature increase. Due to the high temperatures downstream of the bow shock, the aforementioned TPS is mandatory in front of the re–entry configuration to enable the safe descend from space to the planet surface avoiding a burn up of the geometry and the payload, e.g., a planetary sample or astronauts. To guarantee the safe re–entry, the TPS has to withstand these high thermal loads. A conservative approach is to design the TPS to withstand the thermal loads of a turbulent flow around the whole surface, respectively, the highest possible wall heat flux. The drawback of this approach is the resulting high weight of the TPS, respectively, the high costs of the overall space mission due to the additional weight that has to be carried into space by the launcher. To lower the costs that arise due to the weight of the TPS, the knowledge of the laminar–turublent transition onset location is mandatory. Further, the spatial delay of this location around the geometry has a cost reduction effect. This is the case because in a laminar flow a thinner TPS can be used due to the lower wall heat flux. With regard to the outlined effects in re–entry maneuvers, investigations and gaining knowledge of the laminar–turbulent transition mechanism are crucial to effectively design the TPS and to reduce the costs of a space mission.

Besides the general motivation for the investigation of the laminar–turbulent transition outlined before, the transition mechanisms occurring in re–entry maneuvers into the Mars atmosphere gained a greater interest in the last years because of exploration missions of the planet, e.g., the Mars Science laboratory [22] and the Mars 2020 mission [16], and future human space flights to Mars, e.g. planned by NASA [95]. Due to the different gas composition of the Mars atmosphere compared to the Earth atmosphere, therefore, further investigations have to be performed on the influences of the Mars atmosphere on the laminar–turbulent transition to enable a safe descent of the space configuration and to reduce the costs of Mars missions.

1.2 Laminar–Turbulent Transition

In this section, a brief summary of the laminar–turbulent transition process will be given as a theoretical basis for the boundary–layer stability investigations in this work. To outline this process, the stages a flow undergoes from a laminar to a turbulent flow are presented for a flat plate, see Fig. 1.1, following [77]. Although different paths to turbulence are possible, presented for example in [18], the stages associated with the investigated hypersonic test cases in this work are outlined.

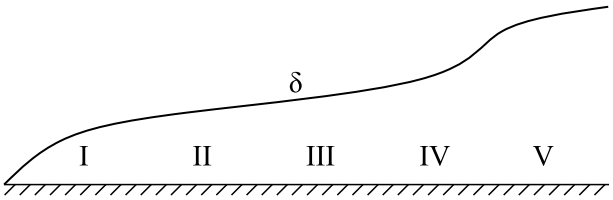

Figure 1.1: Sketch of the laminar–turbulent transition process [77].

Around the tip of the flat plate, represented by stage I, the flow–field is fully laminar without any disturbances. Due to external influences, e.g., the surface roughness or acoustic waves, small disturbances are introduced into the flow–field which can either grow or decay with an increasing distance from the tip. This initial stage, introducing the disturbances, is designated as the boundary–layer receptivity in the literature [18]. If the introduced disturbances start to grow, firstly, two–dimensional primary instabilities, e.g., Tollmien–Schlichting waves for subsonic flows [77] or first and second Mack modes in supersonic flows [18], form in stage II. As these primary instabilities grow further, due to secondary instabilities, three–dimensional disturbances occur in stage III, which are designated as Λ–vortices due to their typical structure. Three types of Λ–vortices are distinguished. The K–type (Klebanoff) Λ–vortices are aligned and show a peak/valley structure [39], whereas the H–type (Herbert) Λ–vortices show a staggered structure [25] and the O–type (oblique) Λ–vortices are staggered and overlap [9, 17]. In stage IV, the breakdown of the vortices starts and turbulent spots arise which finally develop into a fully turbulent flow in stage V, respectively, a significant increase in the boundary–layer thickness δ, the wall heat flux and in the skin friction. In the outlined laminar–turbulent transi-

tion process, it is mandatory that small disturbances are assumed. Otherwise, if the amplitudes of the introduced disturbances exceed a specific limit, the primary instabilities, which show a linear behavior, are bypassed and the initial disturbances are secondary instabilities or turbulent spots. In this case, the linear stability theory and the linear parabolized stability equations, applied in this work, are not valid and, thus, this path to turbulence is not accounted for.

In this work, the boundary–layer stability of super– and hypersonic flows will be investigated. Thus, in stage II, first and second Mack modes occur as the primary instabilities. The first mode is similar to a Tollmien–Schlichting wave, whereas the second and higher Mack modes are acoustic waves trapped inside the boundary–layer [18]. Additional differences between these modes occur especially with respect to the Mach number. In low supersonic flows, the first mode is the dominant mode leading to the laminar–turbulent transition. At higher Mach numbers, e.g. M = 4 for a flat plate [53], the second Mack mode becomes the dominant one. Further, the first mode is an oblique mode. Thus, the maximum growth rate of the first mode appears under a spanwise angle to the centerline of the geometry, where, in contrast, the second mode is a two–dimensional mode and shows the maximum growth rate on the centerline of the geometry [53].

Different methods can be found in the literature to investigate the laminar–turbulent transition such as the DNS (Direct Numerical Simulation), the LST (Linear Stability Theory) and the linear or nonlinear PSE (Parabolized Stability Equations). Applying the DNS, due to solving the full Navier–Stokes equations and resolving small length and time scales, all stages of the laminar–turbulent transition process can be considered. However, due to the very fine mesh, required for these calculations, the computational time exceeds a reasonable limit in a non-scientific environment. Thus, to decrease the computational time for the boundary–layer stability calculations, firstly, the LST and thereafter the linear PSE were developed. These methods allow for the computation of the linear stage II. To further consider the nonlinear stages to the turbulent flow, the nonlinear terms were added to the PSE, resulting in the nonlinear PSE. In this work, as a first step, the LST and the linear PSE were implemented into the boundary–layer stability solver and the investigations will be performed for the linear stage II. In the LST and LPSE, the main quantity to be solved for to characterize the boundary–layer stability is the growth rate. This value describes whether the introduced disturbance grow or decay. To decide if the flow becomes turbulent the semi–empirical e^N–method of Smith & Gamberoni [81] and Van Ingen [97] will be used to calculate the N–factor, which describes the downstream evolution of the disturbance amplitude. At a certain value for the N–factor, the flow field becomes turbulent, where this value depends on several influence parameters, e.g., the free–stream conditions and the geometry, outlined in the next section.

1.3 State of the Art

The initial overview of the laminar–turbulent transition process and of the past investigations on the boundary–layer stability was gained in the lecture series of Schneider

[78]. With this comprehensive overview in mind, the literature review was performed in this work and will be presented in the following.

The first investigations with regard to the boundary–layer stability in the super– and hypersonic flow regime were performed with respect to the free–stream conditions, especially considering the influence of the Mach number. Mack [53] found that, besides the first mode, an additional mode arises at higher Mach numbers which is the so–called second Mack mode. This second mode becomes the dominant mode at Mach numbers above M = 4 for flat plates. Additionally, the results showed that the first mode is an oblique mode, respectively, the maximum in the growth rate appeared under an angle to the centerline of the geometry, whereas the second Mack mode is a 2D–disturbance.

Besides these first observations, numerous investigations on the boundary–layer stability in the super– and hypersonic flow regime were performed, where an overview will be given in the following to emphasize the research in this work. A first influence parameter on the boundary–layer stability, extensively investigated in the last decades, is the nose radius. Famous examples of these investigations are the Stetson Mach 8 cones [84, 85]. In these investigations Stetson et al. examined the differences in the laminar–turbulent transition between a sharp cone and a blunted cone with a small nose radius. The major finding was that blunted cones show significantly higher critical Reynolds numbers and growth rates of the disturbances compared to sharp cones. With regard to these experimental results, numerous numerical investigations were performed on the Stetson blunted cone, e.g., by Esfahanian & Hejranfar [15], Kufner [42], Malik et al. [57], Rosenboom et al. [76], Stilla [88] and Zhong & Ma [105]. To show the influence of the nose radius and, consequently, the entropy–layer swallowing point on the transition onset location, e.g., Kufner [42] performed calculations with respect to the nose radius, where the increase in the nose bluntness and, consequently, a delay in the entropy–layer swallowing point resulted in a delay of the transition onset location. This phenomenon was also observed for different test case configurations considering small nose bluntnesses, e.g., [83]. In contrast, for large nose bluntnesses the reverse effect can be observed, respectively, the transition onset location moves upstream, e.g., described by Ericsson [13] and Softley et al. [82].

Due to differences in the results between the outlined numerical investigations and the experiment of Stetson et al. [85], among other investigated influence parameters, the influence of the wall temperature condition was examined, respectively, an isothermal wall was set in contrast to an adiabatic wall. One of these investigations was performed by Liang et al. [49] on the blunted Stetson Mach 8 cone. The results showed that a wall cooling results in a destabilizing effect on the second Mack mode and a stabilizing effect on the first mode, where similar observations with regard to the wall cooling were made by Kufner [42] and Mack [53] and in experimental investigations by Stetson et al. [87].

With regard to the free–stream parameters, the Reynolds number is a crucial influence parameter. Stetson et al. [86] observed that, with an increasing Reynolds number in the free–stream, the most amplified disturbance frequency increase. Further, Stainback [83] found that the transition onset location moves further upstream

with an increasing free–stream Reynolds number.

One of the main goals in the laminar–turbulent transition analysis is the spatial delay of the transition onset location. Therefore, the injection of CO_2 into the boundary–layer of a sharp cone was investigated by Leyva et al. [46], where two main observations were made. Firstly, if a premixed test gas of CO_2/N_2 or CO_2/Air was used, a significant delay in the transition onset location was found in experiments. Secondly, computations showed that the injection of CO_2 into air can have a stabilizing effect on the boundary-layer stability due to thermo–chemical non–equilibrium effects of CO_2 that absorb the acoustic energy, respectively, damp the second Mack mode. Further studies based on these first numerical investigations have been performed by Wagnild et al. [99]. In this study, it was found that the injection of cold CO_2 results in an immediate transition of the flow but by applying a pre–heated injection and a longer transpiration interval, a delay in the transition was observed. An additional investigation on this test case has been performed by Federov et al. [19], where among other things an influence of the injection rate and the injector shaping on the transition was found. Federov et al. found a stabilizing effect on the boundary–layer transition by injecting air into air if low injection rates were used. In this case, the near field around the injection is only slightly influenced by the injection and a stabilizing effect can evolve in the mid and far field, where this effect is assumed to be enhanced by the injection of CO_2.

Another important influence parameter on the boundary–layer stability, which gained greater interest in the research in the last years, is the thermodynamic model applied in the numerical calculations, respectively, the consideration of chemical reactions and vibrational excitation. A first test case which takes into account the thermo–chemical equilibrium gas model and to perform a comparison with the perfect gas model was the Mach 10 flat plate investigated by Malik & Anderson [56]. Several observations were made with regard to the thermodynamic model. Firstly, a destabilizing effect on the second Mack mode was observed by applying the linear stability theory considering a thermo–chemical equilibrium gas model in comparison to the perfect gas model, where in addition the disturbance frequency shifts to lower values. Secondly, an additional unstable Mack mode, the third mode, was found in the thermo–chemical equilibrium model calculation for higher disturbance frequencies which can not be observed in the perfect gas case. In addition to Malik & Anderson, Marxen et al. [58] and Zanus et al. [104] performed investigations on the same flat plate applying the thermo–chemical equilibrium gas model, where the former performed direct numerical simulations to calculate the boundary–layer stability along the plate and the results agreed well with the results of Malik & Anderson. The latter applied the linear stability theory and the parabolized stability equations along the plate, where also in this case the destabilizing effect of the second Mack mode was shown with a slightly smaller maximum growth rate compared to Malik & Anderson. Further, a stabilizing effect on the first Mack mode was found in their investigations. Additional investigations on the influence of the thermodynamic model have been performed on the same flat plate by Kline et al. [41], where in addition to the perfect gas and the thermo–chemical equilibrium gas model, a finite rate chemistry model

and a thermo–chemical non–equilibrium gas model were considered. In their work, the same destabilizing effect on the second Mack mode in the equilibrium gas model was observed. By applying a finite rate chemistry model, the destabilizing effect was further increased. In contrast, by considering a thermo–chemical non–equilibrium gas model, a reverse trend was found, respectively, the maximum growth rate shows smaller values compared to the finite rate chemistry model. Further examples of research on the thermodynamic model that can be found in the literature have been performed by Chang et al. [12], Hudson et al. [31], Johnson & Candler [35] and Stuckert & Reed [89] with the same observations on a flat plate.

To account for more realistic flight conditions that occur during re–entry maneuvers into the Earth atmosphere, respectively, high–hypersonic Mach numbers, numerical investigations have been performed on the Re–entry F cone free flight experiment [33] in the last years. Firstly, Malik [54] performed LST and PSE calculations applying a perfect gas, thermo–chemical equilibrium gas and finite rate chemistry model to the Re–entry F configuration at an altitude of 30.48 km. The calculations showed high transition onset N–factors applying the PSE of $N = 7.3$ for the perfect gas, $N = 9.8$ for the thermo–chemical equilibrium gas and $N = 9.5$ by applying the finite rate chemistry model. Additionally, for high disturbance frequencies an unstable third mode was recognized in the N–factor distributions of the LST computation which led to an additional increase in the N–factor distributions. Johnson & Candler [34] performed PSE calculations around the Re–entry F cone at two altitudes during the re–entry maneuver, 24.384 km and 30.48 km respectively. In contrast to Malik [54], a thermo–chemical non–equilibrium gas model was applied in the calculations. In this case an N–factor of $N = 8.7$ was found at the transition onset location for an altitude of 30.48 km, respectively a stabilizing effect can be recognized compared to the thermo–chemical equilibrium and finite rate chemistry results of Malik [54]. Further, in their work the effect of surface ablation, that occurred during the re–entry maneuver, was considered at an altitude of 24.384 km, where, with a decreasing nose radius, the transition onset location moved upstream similar to the observations made for the Stetson cone. Similar to Johnson & Candler, Mortensen [62] and Mortensen & Zhong [63] applied a thermo–chemical non–equilibrium model but to compute the LST around the Re–entry F cone. Two different cases were considered in these works applying a 5–species model and an 11–species model, where in the first an N–factor of $N = 7.8$ and in the latter of $N = 7.7$ was found, respectively, smaller values compared to the former presented PSE calculations.

Investigations of the boundary–layer stability in the Mars atmosphere are very rare in the literature. One of these investigations was performed by Kline et al. [40] who investigated the boundary–layer stability over a Mach 10 flat plate. In their work, they performed a comparison between different thermodynamic models, respectively, a finite rate chemistry model and a thermo–chemical non–equilibrium gas model, applied to a 5–species air atmosphere and an 8–species Mars atmosphere. The results of the LST computations showed that the Mars atmosphere has a destabilizing effect on the maximum growth rate compared to air if a finite rate chemistry model is applied but a stabilizing effect by applying a thermo–chemical non–equilibrium gas

model. Thus, also in the N–factor distributions of the LST calculations, the laminar–turbulent transition would occur further downstream in air compared to a Mars atmosphere by applying a finite rate chemistry model but the reverse trend occurs by applying a thermo–chemical non–equilibrium gas model. Another work, found in the literature, was performed by Hollis et al. [29]. In this work, experimental investigations in a high-enthalpy shock tunnel were performed to determine the transition onset location of the Mars Science Laboratory in a CO_2 atmosphere. Further, a comparison with the NASA LAURA code was performed applying laminar, transitional and turbulent flow models to reproduce the measured wall heat flux distributions. The results considering a laminar reacting CO_2 flow showed comparable heat flux distributions along the geometry but the turbulent computations over–predicted the experimental data. Further, Hollis et al. concluded that additional experimental investigations are mandatory to get further insights in the transition of the Mars Science Laboratory to validate their laminar–turbulent transition correlation. Further experimental and numerical investigations with regard to the wall heat flux were performed by Hollis et al. [28] around a sharp and a blunted cone under several free–stream conditions in a CO_2 atmosphere. Similar to the previous investigations, different numerical calculations were performed with the NASA LAURA and DPLR codes, applying laminar, transitional or turbulent flow models, to reproduce the heat flux distributions of the experiments. In addition, first numerical calculations were also performed for the Mars Science Laboratory test run of Hollis et al. [30]. In the results of this work, similar distributions of the heat flux were observed between the experiments and the numerical computations for the laminar and turbulent flow test cases but the computations over–predicted the heat flux in the transitional test cases. Besides these investigations, first boundary–layer stability calculations of the Mars Science Laboratory Run 11 test case of Hollis et al. [29], by applying the LST and the PSE, can be found in the work of Johnson et al. [36] but for air. In the LST calculations an unstable first mode was detected around the stagnation point. Further, their PSE calculations showed that this unstable first mode has a greater growth rate compared to the second Mack mode and, thus, by assuming an N–factor of $N = 5$, this first mode likely leads to the laminar–turbulent transition around the measured transition onset location in the experiment. However, because LST and PSE calculations considering a CO_2 atmosphere were not performed in this work, future investigations are necessary.

1.4 Research Topic and Outline of the Work

Due to the lack of investigations of the boundary–layer stability under Mars atmosphere conditions, this work aims to gather first insights in the transition mechanisms under these conditions. Therefore, stability calculations applying the linear stability theory and the linear parabolized stability equations were performed around a blunted cone. To investigate the influence of the atmosphere on the boundary–layer stability, calculations in different atmospheres, a pure CO_2, the Mars atmosphere and the Earth atmosphere, were performed. Further, different free–stream conditions were

set to examine their influence in the pure CO_2 atmosphere.

To perform the investigations, firstly, a base–flow solver to calculate the laminar base–flow solution and a boundary–layer stability solver to perform the boundary–layer stability calculations were developed in this work, where the implementation of the former will be presented in Sec. 2. In this section, an overview of the governing equations, the thermodynamic models and the numerical implementation containing the spatial and temporal discretization, the boundary conditions, the mesh adaption to capture the shock accurately, the treatment of the singular line and the generation of the grid and the initial solution will be given. Thereafter, the boundary–layer stability solver will be presented in Sec. 3. Similar to the base–flow solver, the governing equations, the thermodynamic models and the numerical implementation will be outlined. The overview of the numerical implementation contains the spatial discretization schemes, the methods applied to the linear stability theory and the linear parabolized stability equations, the boundary conditions, the solution for the step size restriction and the generation of the grid for the stability calculations as well as the interpolation of the base–flow solution onto the new grid. Further, the calculation of the growth rate of the disturbances and the resulting N–factor calculation will be presented. In Sec. 4, validation calculations will be presented which were performed to show the correct implementation of the solvers and the accuracy of the results. To perform the validation of the solvers for the perfect gas model and the thermo–chemical equilibrium gas model, two test cases were selected, respectively, the Stetson Mach 8 cone and a Mach 10 flat plate. After the presentation of the validation results, the boundary–layer transition investigations of the pure CO_2, the Mars, and the Earth atmospheres will be presented in Sec. 5. Firstly, the investigations of the Shot 2 test case in the pure CO_2 atmosphere of Hollis et al. [28] will be presented. Secondly, the Shot 2 results will be compared with results considering the same geometry and similar free–stream conditions but by assuming the Mars atmosphere which contains a small amount of N_2. Thirdly, an additional comparison with regard to the Earth atmosphere will be presented to show the influence of the different gas compositions of the two planets. Lastly, to investigate the influence of the free–stream parameters, the Shot 4 test case of Hollis et al. [28] was calculated and the results will be compared to the Shot 2 results. The work will be concluded by summarizing the observations and by giving an outlook for possible future investigations.

Chapter 2

Base–Flow Solver

2.1 Governing Equations

The investigation of the boundary–layer stability requires an accurate laminar base–flow solution. For this purpose, a parallelized finite–difference Navier–Stokes solver, named CONSST3D (COmpressible Navier–Stokes STeady 3D), was developed in this work [90]. The governing equations of this solver are the conservative, compressible Navier-Stokes equations in general curvilinear coordinates. In the non–dimensional form, based on the derivation in [71], these equations read

$$\frac{\partial J^{-1}\boldsymbol{Q}}{\partial t}+\frac{\partial \mathbf{E}}{\partial \xi}+\frac{\partial \boldsymbol{F}}{\partial \eta}+\frac{\partial \boldsymbol{G}}{\partial \zeta}=\frac{1}{\mathrm{Re}_\infty}\left(\frac{\partial \boldsymbol{E_v}}{\partial \xi}+\frac{\partial \boldsymbol{F_v}}{\partial \eta}+\frac{\partial \boldsymbol{G_v}}{\partial \zeta}\right), \tag{2.1}$$

where

$$\boldsymbol{Q}=\left[\rho,\rho u,\rho v,\rho w,e\right]^T, \tag{2.2}$$

$$\boldsymbol{E}=J^{-1}\begin{bmatrix}\rho v_\xi\\ \rho u v_\xi+\xi_x p\\ \rho v v_\xi+\xi_y p\\ \rho w v_\xi+\xi_z p\\ \rho v_\xi H_t\end{bmatrix},\ \boldsymbol{F}=J^{-1}\begin{bmatrix}\rho v_\eta\\ \rho u v_\eta+\eta_x p\\ \rho v v_\eta+\eta_y p\\ \rho w v_\eta+\eta_z p\\ \rho v_\eta H_t\end{bmatrix},\ \boldsymbol{G}=J^{-1}\begin{bmatrix}\rho v_\zeta\\ \rho u v_\zeta+\zeta_x p\\ \rho v v_\zeta+\zeta_y p\\ \rho w v_\zeta+\zeta_z p\\ \rho v_\zeta H_t\end{bmatrix} \tag{2.3}$$

and

$$\boldsymbol{E_v},\,\boldsymbol{F_v},\,\boldsymbol{G_v}=J^{-1}\begin{bmatrix}0\\ \mu\left(k_x^2+k_y^2+k_z^2\right)\frac{\partial u}{\partial k}+\frac{\mu}{3}\left(k_x\frac{\partial u}{\partial k}+k_y\frac{\partial v}{\partial k}+k_z\frac{\partial w}{\partial k}\right)k_x\\ \mu\left(k_x^2+k_y^2+k_z^2\right)\frac{\partial v}{\partial k}+\frac{\mu}{3}\left(k_x\frac{\partial u}{\partial k}+k_y\frac{\partial v}{\partial k}+k_z\frac{\partial w}{\partial k}\right)k_y\\ \mu\left(k_x^2+k_y^2+k_z^2\right)\frac{\partial w}{\partial k}+\frac{\mu}{3}\left(k_x\frac{\partial u}{\partial k}+k_y\frac{\partial v}{\partial k}+k_z\frac{\partial w}{\partial k}\right)k_z\\ \left(k_x^2+k_y^2+k_z^2\right)\left(\frac{\mu}{2}\frac{\partial(u^2+v^2+w^2)}{\partial k}+\frac{c^*_{p\infty}T^*_\infty}{\mathrm{Pr}_\infty V^{*2}_\infty}\kappa\frac{\partial T}{\partial k}\right)\\ +\frac{\mu}{3}(k_x u+k_y v+k_z w)\left(k_x\frac{\partial u}{\partial k}+k_y\frac{\partial v}{\partial k}+k_z\frac{\partial w}{\partial k}\right)\end{bmatrix}. \tag{2.4}$$

In Eq. (2.4), k represents the curvilinear coordinate ($k=\xi,\,\eta,\,\zeta$) of the respective viscous flux. The non–dimensional flow variables are calculated by dividing the dimensional variable by the respective free–stream value, where the only exception is

the pressure for which the dynamic pressure $\rho_\infty V_\infty^2$ is used [71]. Further, the Prandtl number and the Reynolds number with respect to the nose radius R_N^* as the reference length read

$$\mathrm{Pr}_\infty = \frac{\mu_\infty^* c_{p\infty}^*}{\kappa_\infty^*}, \quad \mathrm{Re}_\infty = \frac{\rho_\infty^* V_\infty^* R_N^*}{\mu_\infty^*}. \tag{2.5}$$

In addition to solve the full Navier–Stokes equations, for high Reynolds number flows, Eq. (2.1) can be simplified by neglecting the streamwise and spanwise viscous fluxes $\boldsymbol{E_v}$ and $\boldsymbol{F_v}$ because they are of order $1/\mathrm{Re}_\infty^{1/2}$ or smaller [71]. This simplification results in the so–called thin–layer Navier–Stokes equations.

The metric terms in Eq. (2.3) and (2.4) to apply the transformation between the Cartesian coordinate system x, y and z and the equidistant computational curvilinear coordinate system ξ, η and ζ, shown in Fig. 2.1, are calculated as follows. The derivatives of the Cartesian coordinates with respect to the curvilinear coordinates, e.g., $\frac{\partial x}{\partial \xi} = x_\xi$, are calculated by finite–differences of second order as

$$x_\xi = \frac{-x_{(i-1,j,l)} + x_{(i+1,j,l)}}{2\Delta\xi} = \frac{-x_{(i-1,j,l)} + x_{(i+1,j,l)}}{2} \tag{2.6}$$

identical to the order of the spatial discretization scheme in Sec. 2.3.1 with $\Delta\xi = 1$. To apply Eq. (2.6) at the boundaries, ghost points outlined in Sec. 2.3.3 are used in the solver. The inverse transformation is given by the matrix inversion of the before

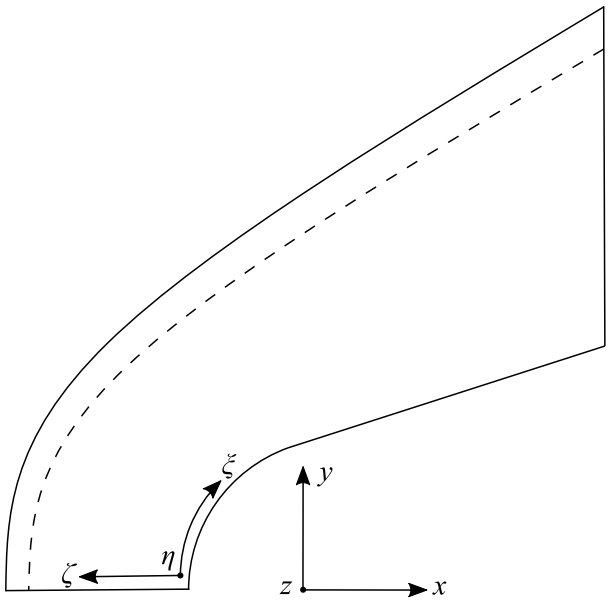

Figure 2.1: Sketch of the Cartesian and the general curvilinear coordinate system around a blunted cone including the bow shock (dashed line).

calculated metric terms as

$$\begin{aligned}
\xi_x &= J(y_\zeta z_\eta - y_\eta z_\zeta),\ \eta_x = J(y_\xi z_\zeta - y_\zeta z_\xi),\ \zeta_x = J(y_\eta z_\xi - y_\xi z_\eta),\\
\xi_y &= J(z_\zeta x_\eta - z_\eta x_\zeta),\ \eta_y = J(z_\xi x_\zeta - z_\zeta x_\xi),\ \zeta_y = J(z_\eta x_\xi - z_\xi x_\eta),\\
\xi_z &= J(x_\zeta y_\eta - x_\eta y_\zeta),\ \eta_z = J(x_\xi y_\zeta - x_\zeta y_\xi),\ \zeta_z = J(x_\eta y_\xi - x_\xi y_\eta),\\
J^{-1} &= (y_\zeta z_\eta - y_\eta z_\zeta)x_\xi + (z_\zeta x_\eta - z_\eta x_\zeta)y_\xi + (x_\zeta y_\eta - x_\eta y_\zeta)z_\xi,
\end{aligned} \tag{2.7}$$

where the same nomenclature is used for the derivatives as $\frac{\partial \xi}{\partial x} = \xi_x$ and, further, $J = 1/J^{-1}$. By applying the transformation relation, the resulting curvilinear velocity components are

$$v_k = k_x u + k_y v + k_z w \tag{2.8}$$

with $k = \xi, \eta, \zeta$ [101]. Note that in Sec. 4 and Sec. 5 the physical curvilinear velocity components are used for the figures and the results presentation which are given by, e.g.,

$$v_{t(i,j,l)} = \frac{\xi_{x(i,0,l)} u_{(i,j,l)} + \xi_{y(i,0,l)} v_{(i,j,l)} + \xi_{z(i,0,l)} w_{(i,j,l)}}{\sqrt{\xi^2_{x(i,0,l)} + \xi^2_{y(i,0,l)} + \xi^2_{z(i,0,l)}}} \tag{2.9}$$

with the metric terms at the wall $j = 0$.

2.2 Thermodynamic Models

2.2.1 Perfect Gas Model

Two types of thermodynamic models are implemented into the solver for the different gas compositions (Air, Mars atmosphere and pure CO_2) investigated in this work. The first one is the perfect gas model valid for moderate temperatures. In this case, the non–dimensional temperature is calculated by

$$T = \gamma \mathrm{M}^2_\infty \frac{p}{\rho}, \tag{2.10}$$

where the Mach number with the speed of sound as $c^*_\infty = \sqrt{\gamma R^* T^*_\infty}$ reads

$$\mathrm{M}_\infty = \frac{V^*_\infty}{c^*_\infty}. \tag{2.11}$$

Further, for perfect gases, the assumption of a constant Prandtl number is made. Thus, the non–dimensional thermal conductivity κ is equal to the non–dimensional dynamic viscosity μ which is estimated via Sutherland's law. In the dimensional form, this equation reads

$$\mu^* = \mu^*_0 \left(\frac{T^*}{T^*_0}\right)^{\frac{3}{2}} \left(\frac{T^*_0 + T^*_s}{T^* + T^*_s}\right). \tag{2.12}$$

The coefficients μ^*_0, T^*_0 and T^*_s and the gas constants for the different gas compositions can be found in Tab. 2.1 [59, 100, 105].

Table 2.1: Sutherland coefficients and gas constants for the different gas compositions [59, 100, 105].

Gas	Pr	γ	R^* [Nm kg^{-1}K^{-1}]	μ_0^* [kg m^{-1}s^{-1}]	T_0^* [K]	T_s^* [K]
Air	0.72	1.4	286.94	1.7894×10^{-5}	288	110.33
Mars	0.76165	1.291	192.161	$1.38357762 \times 10^{-5}$	273	216.6709
CO_2	0.76416	1.2885	188.924	1.370×10^{-5}	273	222

To close the system of equations in Sec. 2.1, a formulation for the total energy per unit volume is required as

$$e = \rho\epsilon + \frac{1}{2}\rho(u^2 + v^2 + w^2) = \frac{p}{\gamma - 1} + \frac{1}{2}\rho(u^2 + v^2 + w^2) \tag{2.13}$$

and for the total enthalpy as

$$H_t = h + \frac{1}{2}(u^2 + v^2 + w^2) = \frac{\gamma}{\gamma - 1}\frac{p}{\rho} + \frac{1}{2}(u^2 + v^2 + w^2). \tag{2.14}$$

With these equations, the system of equations is fully determined and the calculations in the perfect gas regime can be performed.

2.2.2 Thermo–Chemical Equilibrium Gas Model

For high temperatures, effects such as vibrational excitation and chemical reactions play a significant role. The vibrational energy becomes excited at $T^* = 300$ K in air [26], where this effect plays a significant role at temperatures above approximately $T^* = 800$ K [2]. At even higher temperatures, additionally, chemical reactions occur and have to be considered in the thermodynamic model [2]. Thus, the perfect gas assumption is not valid anymore and, further, all thermodynamic and transport properties become functions of two thermodynamic variables. Therefore, to take into account these effects, a thermo–chemical equilibrium or non–equilibrium gas model can be applied, where the former is implemented as the second thermodynamic model in CONSST3D. In the thermo–chemical equilibrium model, in contrast to the thermo–chemical non–equilibrium model, the assumptions are made that the thermal state and the chemical reactions are in equilibrium. This is the case if the reaction time of the chemical reactions and the relaxation time of the vibrational excitation is small compared to the time of the fluid element movement in the flow–field [2].

Two approaches can be applied to account for the thermo–chemical equilibrium model. The first one calculates the actual thermodynamic and transport properties at each grid point in the flow–field by minimizing the Gibbs energy in each iteration step during the calculation. The second approach, implemented in CONSST3D because it significantly reduces the computational time compared to the first approach, uses so–called state surfaces which are generated once in advance of the calculations [64].

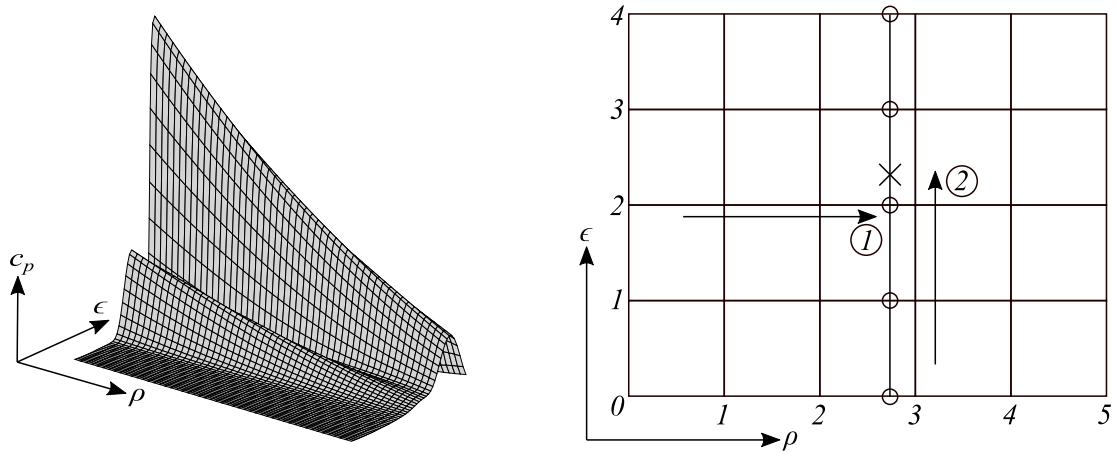

(a) Example of a state surface

(b) Interpolation process on the state surfaces

Figure 2.2: Lagrange polynomial interpolation on the state surfaces.

Table 2.2: Gas compositions of the generated state surfaces [40].

Gas model	Gas composition [vol. %]	Considered species
Air	79 (N_2), 21 (O_2)	N_2, O_2, NO, N, O
Mars	95.366 (CO_2), 4.634 (N_2)	CO_2, N_2, O_2, CO, NO, C, N, O
CO_2	100 (CO_2)	CO_2, O_2, CO, C, O

These state surfaces describe the thermodynamic and transport properties of a specific gas composition with respect to two thermodynamic variables, e.g., $c_p = f(\rho,\epsilon)$, $c_p = f(p,T)$, $\mu = f(\rho,\epsilon)$, etc., for a domain of interest (see Fig. 2.2a). In this work, the state surfaces are generated with the software CEA [21] for the different gas compositions presented in Tab. 2.2.

Because the state surfaces are described by discrete points as shown in Fig. 2.2a, an interpolation technique is necessary to calculate the thermodynamic and transport properties for the grid points in the flow–field. In this work, a Lagrange polynomial of fourth order is applied for this calculation, e.g., for $c_p = f(\rho,\epsilon)$ as

$$\begin{aligned} c_p =& c_{p,0}\frac{\rho-\rho_1}{\rho_0-\rho_1}\frac{\rho-\rho_2}{\rho_0-\rho_2}\frac{\rho-\rho_3}{\rho_0-\rho_3}\frac{\rho-\rho_4}{\rho_0-\rho_4} + c_{p,1}\frac{\rho-\rho_0}{\rho_1-\rho_0}\frac{\rho-\rho_2}{\rho_1-\rho_2}\frac{\rho-\rho_3}{\rho_1-\rho_3}\frac{\rho-\rho_4}{\rho_1-\rho_4} + \\ & c_{p,2}\frac{\rho-\rho_0}{\rho_2-\rho_0}\frac{\rho-\rho_1}{\rho_2-\rho_1}\frac{\rho-\rho_3}{\rho_2-\rho_3}\frac{\rho-\rho_4}{\rho_2-\rho_4} + c_{p,3}\frac{\rho-\rho_0}{\rho_3-\rho_0}\frac{\rho-\rho_1}{\rho_3-\rho_1}\frac{\rho-\rho_2}{\rho_3-\rho_2}\frac{\rho-\rho_4}{\rho_3-\rho_4} + \\ & c_{p,4}\frac{\rho-\rho_0}{\rho_4-\rho_0}\frac{\rho-\rho_1}{\rho_4-\rho_1}\frac{\rho-\rho_2}{\rho_4-\rho_2}\frac{\rho-\rho_3}{\rho_4-\rho_3}. \end{aligned} \tag{2.15}$$

Due to the one–dimensional nature of Eq. (2.15), the interpolation is performed in the two directions successively as shown in Fig. 2.2b. Firstly, the interpolation is performed in the ρ–direction (①) to calculate the variables at the points marked

with a ∘. Secondly, the interpolation is performed in the ϵ-direction (②) with the before calculated variables to determine the thermodynamic or transport variable at × corresponding to the density and the internal energy at the grid point in the flow–field. To further increase the efficiency of the interpolation process, Eq. (2.15) can be simplified for the first interpolation (①) to

$$c_p = c_4\rho^4 + c_3\rho^3 + c_2\rho^2 + c_1\rho + c_0, \tag{2.16}$$

where c_0–c_4 are constants from the Lagrange polynomial. Nevertheless, the second interpolation (②) still requires Eq. (2.15) due to the unknown values of c_p at the intermediate points ∘ before the first interpolation is performed.

The program CEA is capable of calculating the thermodynamic and transport properties from $T^* = 200$ K to $T^* = 20000$ K [21]. Thus, a model has to be implemented for temperatures below this lower limit to deal with low temperatures in the thermo–chemical equilibrium model. In case of CONSST3D, the perfect gas model of Sec. 2.2.1 is applied at temperatures below $T^* = 300$ K. A slightly higher temperature than the lower limit of CEA is used because at this temperature, nearly the standard temperature, the thermodynamic and transport properties can be calculated without a great discontinuity at the boundary to the thermo–chemical equilibrium model.

To solve Eq. (2.1), the process outlined in this section is performed for each thermodynamic and transport variable to close the system of equations.

2.3 Numerical Implementation

2.3.1 Spatial Discretization

The governing equations of Sec. 2.1 require adequate spatial and temporal discretization schemes and boundary conditions. To perform the spatial disretization, a flux splitting scheme is applied to the inviscid fluxes $\boldsymbol{E}$, $\boldsymbol{F}$ and $\boldsymbol{G}$ and a central finite–difference scheme to the viscous fluxes $\boldsymbol{E_v}$, $\boldsymbol{F_v}$ and $\boldsymbol{G_v}$. The flux splitting schemes implemented in CONSST3D are the AUSM+ [51], AUSM+–up [50] and the AUSMPW+ [38] flux splitting schemes, where the latter was applied in this work due to two main advantages compared to the original AUSM+ flux splitting scheme. Firstly, overshoots and oscillations of the flow variables are eliminated at shocks and, secondly, the presence of flow variable oscillations at the wall is removed [38].

In the following, the equations of the AUSMPW+ flux splitting scheme are presented in the streamwise direction with respect to Fig. 2.3 following the derivation in [38]. For simplicity and readability reasons, only the subscript i for the streamwise direction is used in the following equations of this section. In the normal and spanwise direction, similar equations can be derived by replacing the respective metric terms and by performing the calculation in the respective spatial direction. In general curvilinear coordinates, the inviscid fluxes at $i \pm 1/2$, respectively, between two grid

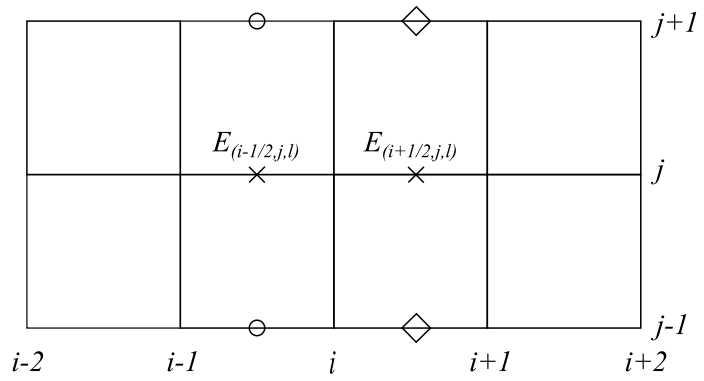

Figure 2.3: Sketch of the flux splitting scheme.

points, are calculated by

$$\begin{aligned}\boldsymbol{E}_{(i\pm1/2)} =& J^{-1}_{(i\pm1/2)}|\nabla\xi_{(i\pm1/2)}|\left(\hat{\mathrm{M}}^{+}_{L(i\pm1/2)}\boldsymbol{m}_{L(i\pm1/2)}c_{(i\pm1/2)} + \hat{\mathrm{M}}^{-}_{R(i\pm1/2)}\boldsymbol{m}_{R(i\pm1/2)}c_{(i\pm1/2)}\right)\\ &+J^{-1}_{(i\pm1/2)}\boldsymbol{\xi}_{(i\pm1/2)}\left(P^{+}_{L(i\pm1/2)}\boldsymbol{p}_{L(i\pm1/2)} + P^{-}_{R(i\pm1/2)}\boldsymbol{p}_{R(i\pm1/2)}\right)\end{aligned} \tag{2.17}$$

with $\boldsymbol{m} = [\rho, \rho u, \rho v, \rho w, \rho H_t]^T$, $\boldsymbol{p} = [0,p,p,p,0]^T$, $\boldsymbol{\xi} = [0,\xi_x,\xi_y,\xi_z,0]^T$ and $|\nabla\xi| = \sqrt{\xi_x^2+\xi_y^2+\xi_z^2}$. The metric terms J^{-1}, ξ_x, ξ_y and ξ_z at $i \pm 1/2$ are calculated by the local average of the neighboring grid points [42]. In Eq. (2.17), the Mach numbers $\hat{\mathrm{M}}^{\pm}_{L,R(i\pm1/2)}$ are defined as

$$\hat{\mathrm{M}}^{+}_{L(i\pm1/2)} = \mathrm{M}^{+}_{L(i\pm1/2)} + \mathrm{M}^{-}_{R(i\pm1/2)}[(1-\omega^{\mathrm{AUSM}}_{(i\pm1/2)})(1+f^{\mathrm{AUSM}}_{R(i\pm1/2)}) - f^{\mathrm{AUSM}}_{L(i\pm1/2)}], \tag{2.18}$$

$$\hat{\mathrm{M}}^{-}_{R(i\pm1/2)} = \mathrm{M}^{-}_{R(i\pm1/2)}\omega^{\mathrm{AUSM}}_{(i\pm1/2)}(1+f^{\mathrm{AUSM}}_{R(i\pm1/2)}), \tag{2.19}$$

for $\mathrm{M}^{+}_{L(i\pm1/2)} + \mathrm{M}^{-}_{R(i\pm1/2)} \geq 0$, and as

$$\hat{\mathrm{M}}^{+}_{L(i\pm1/2)} = \mathrm{M}^{+}_{L(i\pm1/2)}\omega^{\mathrm{AUSM}}_{(i\pm1/2)}(1+f^{\mathrm{AUSM}}_{L(i\pm1/2)}), \tag{2.20}$$

$$\hat{\mathrm{M}}^{-}_{R(i\pm1/2)} = \mathrm{M}^{-}_{R(i\pm1/2)} + \mathrm{M}^{+}_{L(i\pm1/2)}[(1-\omega^{\mathrm{AUSM}}_{(i\pm1/2)})(1+f^{\mathrm{AUSM}}_{L(i\pm1/2)}) - f^{\mathrm{AUSM}}_{R(i\pm1/2)}], \tag{2.21}$$

for $\mathrm{M}^{+}_{L(i\pm1/2)} + \mathrm{M}^{-}_{R(i\pm1/2)} < 0$, with

$$\omega^{\mathrm{AUSM}}_{(i\pm1/2)} = 1 - \min\left(\frac{p_L}{p_R},\frac{p_R}{p_L}\right)^3_{(i\pm1/2)} \tag{2.22}$$

and

$$f^{\mathrm{AUSM}}_{L,R(i\pm1/2)} = \begin{cases} \left(\dfrac{p_{L,R(i\pm1/2)}}{p_{s(i\pm1/2)}} - 1\right)\min\left(1,\dfrac{\min(p_{k,L},p_{k,R})}{\min(p_L,p_R)}\right)^2_{(i\pm1/2)} & , \text{ for } p_{s(i\pm1/2)} \neq 0 \\ 0 & , \text{ for } p_{s(i\pm1/2)} = 0 \end{cases}. \tag{2.23}$$

In Eq. (2.23), the pressure terms $p_{k,L,R}$ are reconstructed from the surrounding grid points of the discretized grid point shown in Fig. 2.3 for a two–dimensional case marked with the two circle symbols for the flux $\boldsymbol{E}_{(i-1/2)}$ and the two diamond symbols for the flux $\boldsymbol{E}_{(i+1/2)}$. Further, in Eq. (2.23) p_s is defined as $p_s = P_L^+ p_L + P_R^- p_R$. The Mach number splitting functions in the previous equations are calculated by

$$\mathrm{M}^{\pm}_{L,R(i\pm1/2)} = \begin{cases} \frac{1}{2}(\mathrm{M}_{L,R(i\pm1/2)} \pm |\mathrm{M}_{L,R(i\pm1/2)}|) & , \quad \text{if } |\mathrm{M}_{L,R(i\pm1/2)}| > 1 \\ \pm\frac{1}{4}(\mathrm{M}_{L,R(i\pm1/2)} \pm 1)^2 & , \quad \text{if } |\mathrm{M}_{L,R(i\pm1/2)}| \leq 1 \end{cases} \tag{2.24}$$

and the pressure splitting functions by

$$P^{\pm}_{L,R(i\pm1/2)} = \begin{cases} \frac{1}{2}(1 \pm \mathrm{sign}(\mathrm{M}_{L,R(i\pm1/2)})) & , \quad \text{if } |\mathrm{M}_{L,R(i\pm1/2)}| > 1 \\ \frac{1}{4}(\mathrm{M}_{L,R(i\pm1/2)} \pm 1)^2(2 \mp \mathrm{M}_{L,R(i\pm1/2)}) & \\ \pm\frac{3}{16}\mathrm{M}_{L,R(i\pm1/2)}(\mathrm{M}^2_{L,R(i\pm1/2)} - 1)^2 & , \quad \text{if } |\mathrm{M}_{L,R(i\pm1/2)}| \leq 1 \end{cases} . \tag{2.25}$$

The speed of sound that is used in Eq. (2.17) and for calculating the streamwise Mach number $\mathrm{M}^{\pm}_{L,R(i\pm1/2)} = v_{\xi,L,R(i\pm1/2)}/|\nabla\xi|/c_{(i\pm1/2)}$ is

$$\begin{cases} c_{(i\pm1/2)} = \dfrac{c^2_{s(i\pm1/2)}}{\max(|v_{\xi,L(i\pm1/2)}/|\nabla\xi||,\, c_{s(i\pm1/2)})}, & \text{for } \dfrac{1}{2}(v_{\xi,L(i\pm1/2)} + v_{\xi,R(i\pm1/2)}) > 0 \\ c_{(i\pm1/2)} = \dfrac{c^2_{s(i\pm1/2)}}{\max(|v_{\xi,R(i\pm1/2)}/|\nabla\xi||,\, c_{s(i\pm1/2)})}, & \text{for } \dfrac{1}{2}(v_{\xi,L(i\pm1/2)} + v_{\xi,R(i\pm1/2)}) \leq 0 \end{cases}, \tag{2.26}$$

where c_s for the perfect gas regime is calculated by the normal total enthalpy as

$$c_s = \sqrt{2(\gamma-1)/(\gamma+1)H_{t,n}}, \tag{2.27}$$

where the normal direction is the actual direction of discretization. This normal total enthalpy reads

$$H_{t,n} = \frac{1}{2}(H_{t,n,L} + H_{t,n,R}) \tag{2.28}$$

with

$$H_{t,n,L,R} = \frac{\gamma}{\gamma-1}\frac{p_{L,R}}{\rho_{L,R}} + \frac{1}{2}\frac{v_{\xi,L,R}}{|\nabla\xi|} = h_{L,R} + \frac{1}{2}\frac{v_{\xi,L,R}}{|\nabla\xi|}. \tag{2.29}$$

In the case of calculations in thermo–chemical equilibrium, the calculation of the speed of sound to perform the flux splitting has to be modified. In [38] a possible modification of Eq. (2.27) is given by

$$c_s = \left(2H_{t_n}\frac{(\gamma_{eq,L}-1)/\gamma_{eq,L}\rho_L - (\gamma_{eq,R}-1)/\gamma_{eq,R}\rho_R}{(\gamma_{eq,R}+1)/\gamma_{eq,R}\rho_L - (\gamma_{eq,L}+1)/\gamma_{eq,L}\rho_R}\right)^{0.5}, \tag{2.30}$$

where γ_{eq} is the specific heat capacity ratio of the actual gas composition in thermo–chemical equilibrium. This modification results in an indefinite speed of sound if the left and right states are equal which is especially the case using ghost points in combination with mirror conditions and in the free–stream, where the flow variables are constant. Thus, to avoid this issue in this work, the speed of sound for the flux splitting is calculated differently by

$$c_s = \sqrt{2\left(\frac{\gamma_{eq,L}+\gamma_{eq,R}}{2}-1\right)/\left(\frac{\gamma_{eq,L}+\gamma_{eq,R}}{2}+1\right)H_{t,n}}. \tag{2.31}$$

To apply the flux splitting scheme, the primitive flow variables $\boldsymbol{q} = [\rho,u,v,w,p]^{\mathrm{T}}$ have to be reconstructed for the left and right states at $i \pm 1/2$. Therefore, a fully upwind MUSCL–reconstruction (Monotonic Upstream-Centered Scheme for Conservation Laws) of second order is used. In the streamwise direction, the respective equations are

$$\boldsymbol{q}_{R(i+1/2)} = \boldsymbol{q}_{(i+1)} - 0.5\phi_{(i+1)}(\boldsymbol{q}_{(i+2)} - \boldsymbol{q}_{(i+1)}) \tag{2.32}$$
$$\boldsymbol{q}_{L(i+1/2)} = \boldsymbol{q}_{(i)} + 0.5\phi_{(i)}(\boldsymbol{q}_{(i+1)} - \boldsymbol{q}_{(i)}) \tag{2.33}$$
$$\boldsymbol{q}_{R(i-1/2)} = \boldsymbol{q}_{(i)} - 0.5\phi_{(i)}(\boldsymbol{q}_{(i+1)} - \boldsymbol{q}_{(i)}) \tag{2.34}$$
$$\boldsymbol{q}_{L(i-1/2)} = \boldsymbol{q}_{(i-1)} + 0.5\phi_{(i-1)}(\boldsymbol{q}_{(i)} - \boldsymbol{q}_{(i-1)}) \tag{2.35}$$

[102]. Beside the van Leer, the minmod and the superbee limiters [37, 75], the van Albada limiter

$$\phi_i = \frac{r_{(i)}^2 + r_{(i)}}{r_{(i)}^2 + 1} \quad \text{with } r_{(i)} = \frac{\boldsymbol{q}_{(i)} - \boldsymbol{q}_{(i-1)}}{\boldsymbol{q}_{(i+1)} - \boldsymbol{q}_{(i)}} \tag{2.36}$$

[37, 96] is implemented in CONSST3D and applied in this work to accomplish a TVD–character (Total Variation Diminishing). Lastly, the discretization of the inviscid fluxes is performed by

$$\left(\frac{\partial \boldsymbol{E}}{\partial \xi}\right)_{(i)} = -\boldsymbol{E}_{(i-1/2)} + \boldsymbol{E}_{(i+1/2)}. \tag{2.37}$$

As mentioned earlier in this section, the discretization of the viscous fluxes is performed by a central finite–difference scheme, in this case of second order to retain the same spatial accuracy as for the inviscid fluxes. Thus, the discretization in the streamwise direction is performed by

$$\left(\frac{\partial \boldsymbol{E}_{\boldsymbol{v}}}{\partial \xi}\right)_{(i)} = \frac{-\boldsymbol{E}_{\boldsymbol{v}(i-1)} + \boldsymbol{E}_{\boldsymbol{v}(i+1)}}{2}. \tag{2.38}$$

Analogous to the inviscid fluxes, the viscous fluxes in the normal and spanwise directions are discretized in a similar way.

2.3.2 Temporal Discretization

Two types of temporal discretization schemes are implemented in CONSST3D. The first one is an explicit four-stage low-storage Runge–Kutta method to solve Eq. (2.1) as

$$\Delta \boldsymbol{Q} = -\frac{\Delta t}{J^{-1}}\left(\frac{\partial \boldsymbol{E}}{\partial \xi}+\frac{\partial \boldsymbol{F}}{\partial \eta}+\frac{\partial \boldsymbol{G}}{\partial \zeta}-\frac{1}{\mathrm{Re}_\infty}\left(\frac{\partial \boldsymbol{E_v}}{\partial \xi}+\frac{\partial \boldsymbol{F_v}}{\partial \eta}+\frac{\partial \boldsymbol{G_v}}{\partial \zeta}\right)\right) = -\frac{\Delta t}{J^{-1}}\mathbf{Res} \tag{2.39}$$

by

$$\boldsymbol{Q}^k = \boldsymbol{Q}^0 - c^k_{\mathrm{RK}}\frac{\Delta t}{J^{-1}}\mathbf{Res}^{k-1} \tag{2.40}$$

with k representing the current stage and c^k_{RK} are the stage coefficients which can be found in [6]. This method, implemented in combination with a second–order spatial upwind scheme, is theoretically stable up to a CFL number of CFL=0.92 [6]. Thus, to further increase the possible CFL number, respectively, decreasing the computational time necessary to achieve the convergence to steady state, the second scheme, an implicit backward Euler method applying the LU-SGS (Lower–Upper Symmetric–Gauß–Seidel) method, originally developed by Yoon & Jameson [103], is used in this work. This method has the advantage to be theoretically unconditionally stable (CFL $= \infty$) [103], significantly increasing the efficiency of the calculation. In this scheme, Eq. (2.39) is written in the form

$$\Delta \boldsymbol{Q} = \boldsymbol{Q}^{k+1} - \boldsymbol{Q}^k = -\frac{\Delta t}{J^{-1}}\mathbf{Res}^{k+1}. \tag{2.41}$$

Because $\mathbf{Res}^{k+1}$ is unknown at the current time step k, a linearization is performed around the current time step by applying a first–order Taylor–series expansion as

$$\mathbf{Res}^{k+1} = \mathbf{Res}^k + \frac{\partial \mathbf{Res}^k}{\partial \boldsymbol{Q}}\Delta \boldsymbol{Q}^k. \tag{2.42}$$

Inserting Eq. (2.42) into (2.41), the equation to be solved becomes

$$\begin{aligned}
&\left(\frac{J^{-1}}{\Delta t}\boldsymbol{I}+\frac{\partial}{\partial \xi}\left(\frac{\partial \boldsymbol{E}}{\partial \boldsymbol{Q}}\right)+\frac{\partial}{\partial \eta}\left(\frac{\partial \boldsymbol{F}}{\partial \boldsymbol{Q}}\right)+\frac{\partial}{\partial \zeta}\left(\frac{\partial \boldsymbol{G}}{\partial \boldsymbol{Q}}\right)\right.\\
&\left.-\frac{1}{\mathrm{Re}_\infty}\left(\frac{\partial}{\partial \xi}\left(\frac{\partial \boldsymbol{E_v}}{\partial \boldsymbol{Q}}\right)+\frac{\partial}{\partial \eta}\left(\frac{\partial \boldsymbol{F_v}}{\partial \boldsymbol{Q}}\right)+\frac{\partial}{\partial \zeta}\left(\frac{\partial \boldsymbol{G_v}}{\partial \boldsymbol{Q}}\right)\right)\right)\Delta \boldsymbol{Q}\\
&=\left(\frac{J^{-1}}{\Delta t}\boldsymbol{I}+\frac{\partial \boldsymbol{A}}{\partial \xi}+\frac{\partial \boldsymbol{B}}{\partial \eta}+\frac{\partial \boldsymbol{C}}{\partial \zeta}-\frac{1}{\mathrm{Re}_\infty}\left(\frac{\partial \boldsymbol{A_v}}{\partial \xi}+\frac{\partial \boldsymbol{B_v}}{\partial \eta}+\frac{\partial \boldsymbol{C_v}}{\partial \zeta}\right)\right)\Delta \boldsymbol{Q} = -\mathbf{Res}^k,
\end{aligned} \tag{2.43}$$

where $\boldsymbol{I}$ is the identity matrix and $\boldsymbol{A}$, $\boldsymbol{B}$ and $\boldsymbol{C}$ are the inviscid flux Jacobians in the respective spatial direction, which can be found in appendix A.1 for a perfect gas [42]. Further, the terms $\boldsymbol{A_v}$, $\boldsymbol{B_v}$ and $\boldsymbol{C_v}$ are the viscous flux Jacobians in the respective

spatial direction given by a scalar representation [65]. Applying a flux splitting and a lower upper decomposition the system of equations becomes

$$\begin{aligned}
\boldsymbol{D} &= \frac{J^{-1}}{\Delta t}\boldsymbol{I} \\
&+ \left(\boldsymbol{A}^{+}_{(i+1/2,j,l)} - \boldsymbol{A}^{-}_{(i-1/2,j,l)} + \boldsymbol{B}^{+}_{(i,j+1/2,l)} - \boldsymbol{B}^{-}_{(i,j-1/2,l)} + \boldsymbol{C}^{+}_{(i,j,l+1/2)} - \boldsymbol{C}^{-}_{(i,j,l-1/2)}\right) \\
&+ \frac{1}{2}\left(\lambda(\boldsymbol{A}_{\boldsymbol{v}})_{(i+1,j,l)} - \lambda(\boldsymbol{A}_{\boldsymbol{v}})_{(i-1,j,l)} + \lambda(\boldsymbol{B}_{\boldsymbol{v}})_{(i,j+1,l)} - \lambda(\boldsymbol{B}_{\boldsymbol{v}})_{(i,j-1,l)}\right. \\
&\left.+\lambda(\boldsymbol{C}_{\boldsymbol{v}})_{(i,j,l+1)} - \lambda(\boldsymbol{C}_{\boldsymbol{v}})_{(i,j,l-1)}\right)\boldsymbol{I} \\
&= \frac{J^{-1}}{\Delta t}\boldsymbol{I} + \left(\lambda(\boldsymbol{A}) + \lambda(\boldsymbol{B}) + \lambda(\boldsymbol{C})\right)_{(i,j,l)}\boldsymbol{I} + \frac{1}{2}\left(\lambda(\boldsymbol{A}_{\boldsymbol{v}})_{(i+1,j,l)} - \lambda(\boldsymbol{A}_{\boldsymbol{v}})_{(i-1,j,l)}\right. \\
&\left.+\lambda(\boldsymbol{B}_{\boldsymbol{v}})_{(i,j+1,l)} - \lambda(\boldsymbol{B}_{\boldsymbol{v}})_{(i,j-1,l)} + \lambda(\boldsymbol{C}_{\boldsymbol{v}})_{(i,j,l+1)} - \lambda(\boldsymbol{C}_{\boldsymbol{v}})_{(i,j,l-1)}\right)\boldsymbol{I}, \qquad (2.44)\\
\boldsymbol{L} &= \left(-\boldsymbol{A}^{+}_{(i-1/2,j,l)} - \boldsymbol{B}^{+}_{(i,j-1/2,l)} - \boldsymbol{C}^{+}_{(i,j,l-1/2)}\right) \\
&+ \frac{1}{2}\left(\lambda(\boldsymbol{A}_{\boldsymbol{v}})_{(i-1,j,l)} + \lambda(\boldsymbol{B}_{\boldsymbol{v}})_{(i,j-1,l)} + \lambda(\boldsymbol{C}_{\boldsymbol{v}})_{(i,j,l-1)}\right)\boldsymbol{I}, \qquad (2.45)\\
\boldsymbol{U} &= \left(\boldsymbol{A}^{-}_{(i+1/2,j,l)} + \boldsymbol{B}^{-}_{(i,j+1/2,l)} + \boldsymbol{C}^{-}_{(i,j,l+1/2)}\right) \\
&- \frac{1}{2}\left(\lambda(\boldsymbol{A}_{\boldsymbol{v}})_{(i+1,j,l)} + \lambda(\boldsymbol{B}_{\boldsymbol{v}})_{(i,j+1,l)} + \lambda(\boldsymbol{C}_{\boldsymbol{v}})_{(i,j,l+1)}\right)\boldsymbol{I} \qquad (2.46)
\end{aligned}$$

with the inviscid implicit terms which are split by the maximum eigenvalue of the inviscid Jacobian matrices as

$$\begin{aligned}
\boldsymbol{A}^{\pm}_{(i\mp1/2,j,l)} &= \frac{1}{2}\left(\boldsymbol{A}_{(i\mp1,j,l)} \pm \lambda(\boldsymbol{A})_{(i\mp1,j,l)}\boldsymbol{I}\right), \\
\boldsymbol{B}^{\pm}_{(i,j\mp1/2,l)} &= \frac{1}{2}\left(\boldsymbol{B}_{(i,j\mp1,l)} \pm \lambda(\boldsymbol{B})_{(i,j\mp1,l)}\boldsymbol{I}\right), \qquad (2.47)\\
\boldsymbol{C}^{\pm}_{(i,j,l\mp1/2)} &= \frac{1}{2}\left(\boldsymbol{C}_{(i,j,l\mp1)} \pm \lambda(\boldsymbol{C})_{(i,j,l\mp1)}\boldsymbol{I}\right),
\end{aligned}$$

where the maximum eigenvalues are

$$\begin{aligned}
\lambda(\boldsymbol{A})_{(i\mp1,j,l)} &= J^{-1}_{(i\mp1/2,j,l)}(|v_{\xi(i\mp1,j,l)}| + |\nabla\xi_{(i\mp1/2,j,l)}|c_{(i\mp1,j,l)}), \\
\lambda(\boldsymbol{B})_{(i,j\mp1,l)} &= J^{-1}_{(i,j\mp1/2,l)}(|v_{\zeta(i,j\mp1,l)}| + |\nabla\zeta_{(i,j\mp1/2,l)}|c_{(i,j\mp1,l)}), \qquad (2.48)\\
\lambda(\boldsymbol{C})_{(i,j,l\mp1)} &= J^{-1}_{(i,j,l\mp1/2)}(|v_{\eta(i,j,l\mp1)}| + |\nabla\eta_{(i,j,l\mp1/2)}|c_{(i,j,l\mp1)})
\end{aligned}$$

[103]. Further, the scalar representations for the viscous implicit terms are given by

$$\begin{aligned}
\lambda(\boldsymbol{A}_{\boldsymbol{v}})_{(i\mp1,j,l)} &= \mp J^{-1}_{(i\mp1,j,l)}|\nabla\xi_{(i\mp1,j,l)}|^2\frac{\mu_{(i\mp1,j,l)}}{\rho_{(i\mp1,j,l)}\mathrm{Re}_\infty}, \\
\lambda(\boldsymbol{B}_{\boldsymbol{v}})_{(i,j\mp1,l)} &= \mp J^{-1}_{(i,j\mp1,l)}|\nabla\zeta_{(i,j\mp1,l)}|^2\frac{\mu_{(i,j\mp1,l)}}{\rho_{(i,j\mp1,l)}\mathrm{Re}_\infty}, \qquad (2.49)\\
\lambda(\boldsymbol{C}_{\boldsymbol{v}})_{(i,j,l\mp1)} &= \mp J^{-1}_{(i,j,l\mp1)}|\nabla\eta_{(i,j,l\mp1)}|^2\frac{\mu_{(i,j,l\mp1)}}{\rho_{(i,j,l\mp1)}\mathrm{Re}_\infty}
\end{aligned}$$

[65]. This resulting system of equations can be solved by a Gauß–Seidel algorithm, firstly, applying a forward sweep as

$$(\boldsymbol{D} + \boldsymbol{L})\Delta\boldsymbol{Q}^{\boldsymbol{F}} = -\mathbf{Res} \tag{2.50}$$

and, secondly, applying a backward sweep as [52]

$$(\boldsymbol{D} + \boldsymbol{U})\Delta\boldsymbol{Q} = \boldsymbol{D}\Delta\boldsymbol{Q}^{\boldsymbol{F}}. \tag{2.51}$$

To apply the LU-SGS scheme to the calculations considering the thermo–chemical equilibrium gas model, the inviscid flux Jacobians of the implicit terms are modified similar to [60], which is presented in appendix A.2. Further, the viscous terms remain the same as for the perfect gas assumption but by applying the state surfaces of Sec. 2.2.2 to calculate the thermodynamic and transport properties.

In both time discretization schemes, a local time stepping is applied to further improve the computational efficiency. The local time step is calculated at each streamwise location along the geometry, respectively, constant along a wall normal and in the spanwise direction, for an equidistant grid with $\Delta\xi = \Delta\eta = \Delta\zeta = 1$ by

$$\Delta t = \frac{\mathrm{CFL}}{\max(|\lambda_\xi|,\, |\lambda_\zeta|,\, |\lambda_\eta|)}, \tag{2.52}$$

where $|\lambda_\xi|$, $|\lambda_\zeta|$ and $|\lambda_\eta|$ are the absolute values of the maximum eigenvalues of the inviscid Jacobian matrices in the respective direction, e.g., $|\lambda_\xi| = |v_\xi| + |\nabla\xi|c$ [7].

2.3.3 Boundary Conditions

Appropriate boundary conditions are required to solve the Navier–Stokes or the thin–layer Navier–Stokes equations in this work. At the wall, the no–slip condition is applied. This boundary condition is accomplished by setting a zero velocity at the wall, $v_\xi = 0$, $v_\eta = 0$ and $v_\zeta = 0$, respectively. Additionally, a boundary condition for the pressure at the wall grid points is necessary. Several methods are available to prescribe these boundary conditions. In this work, the Navier–Stokes characteristic boundary conditions (NSCBC), based on the fundamentals of Thompson [93] and derived by Poinsot & Lele [72], are implemented. Following the curvilinear primitive variable representation described by Landmann et al. [44], firstly, a characteristic decomposition is performed for the Navier-Stokes equations in the primitive form. The resulting system of equations is

$$\begin{aligned}&\frac{\partial \boldsymbol{q}}{\partial t} + \boldsymbol{d}_{\boldsymbol{\zeta}} + J\boldsymbol{M}^{-1}\left(\boldsymbol{k}_{\boldsymbol{\zeta}} + \frac{\partial \boldsymbol{E}}{\partial \xi} + \frac{\partial \boldsymbol{F}}{\partial \eta} - \frac{1}{\mathrm{Re}_\infty}\left(\frac{\partial \boldsymbol{E}_{\boldsymbol{v}}}{\partial \xi} + \frac{\partial \boldsymbol{F}_{\boldsymbol{v}}}{\partial \eta} + \frac{\partial \boldsymbol{G}_{\boldsymbol{v}}}{\partial \zeta}\right)\right)\\ =&\frac{\partial \boldsymbol{q}}{\partial t} + \boldsymbol{d}_{\boldsymbol{\zeta}} + \boldsymbol{b}_{\boldsymbol{\zeta}} = 0,\end{aligned} \tag{2.53}$$

where $\boldsymbol{k}_{\boldsymbol{\zeta}}$ considers the partial derivatives of the metric terms with respect to the ζ–direction by

$$\boldsymbol{k}_{\boldsymbol{\zeta}} = \boldsymbol{E}_{\mathrm{cart}}\frac{\partial}{\partial\zeta}\left(\frac{\zeta_x}{J}\right) + \boldsymbol{F}_{\mathrm{cart}}\frac{\partial}{\partial\zeta}\left(\frac{\zeta_z}{J}\right) + \boldsymbol{G}_{\mathrm{cart}}\frac{\partial}{\partial\zeta}\left(\frac{\zeta_y}{J}\right) \tag{2.54}$$

with the fluxes in Cartesian coordinates denoted by the subscript "cart" and $\boldsymbol{M}^{-1}$ is the transformation matrix that describes the transformation of the conservative variables to the primitive variables. This transformation matrix can be found in appendix B. The boundary conditions are specified in $\boldsymbol{d}_{\boldsymbol{\zeta}}$ which is

$$\boldsymbol{d}_{\boldsymbol{\zeta}} = \begin{bmatrix} \frac{\rho}{\sqrt{2}c}(\boldsymbol{L}_{\boldsymbol{\zeta},4} + \boldsymbol{L}_{\boldsymbol{\zeta},5}) \\ \frac{\zeta_x/|\nabla\zeta|}{\sqrt{2}}(\boldsymbol{L}_{\boldsymbol{\zeta},4} - \boldsymbol{L}_{\boldsymbol{\zeta},5}) \\ \frac{\zeta_y/|\nabla\zeta|}{\sqrt{2}}(\boldsymbol{L}_{\boldsymbol{\zeta},4} - \boldsymbol{L}_{\boldsymbol{\zeta},5}) \\ \frac{\zeta_z/|\nabla\zeta|}{\sqrt{2}}(\boldsymbol{L}_{\boldsymbol{\zeta},4} - \boldsymbol{L}_{\boldsymbol{\zeta},5}) \\ \frac{c\rho}{\sqrt{2}}(\boldsymbol{L}_{\boldsymbol{\zeta},4} + \boldsymbol{L}_{\boldsymbol{\zeta},5}) \end{bmatrix} \tag{2.55}$$

at the wall, where

$$\boldsymbol{L}_{\boldsymbol{\zeta}} = \begin{bmatrix} 0 \\ 0 \\ 0 \\ \boldsymbol{L}_{\boldsymbol{\zeta},5} - \frac{\sqrt{2}(\zeta_x/|\nabla\zeta|\boldsymbol{b}_{\boldsymbol{\zeta},2} + \zeta_y/|\nabla\zeta|\boldsymbol{b}_{\boldsymbol{\zeta},3} + \zeta_z/|\nabla\zeta|\boldsymbol{b}_{\boldsymbol{\zeta},4})}{|\nabla\zeta|} \\ \frac{\boldsymbol{\lambda}_{\boldsymbol{\zeta},5}}{\sqrt{2}}(\frac{\partial p/\partial\zeta}{c\rho} - \zeta_x/|\nabla\zeta|\partial u/\partial\zeta - \zeta_y/|\nabla\zeta|\partial v/\partial\zeta - \zeta_z/|\nabla\zeta|\partial w/\partial\zeta) \end{bmatrix} \tag{2.56}$$

with the eigenvalue $\boldsymbol{\lambda}_{\boldsymbol{\zeta},5} = v_\zeta - c|\nabla\zeta|$ and $|\nabla\zeta| = \sqrt{\zeta_x^2 + \zeta_y^2 + \zeta_z^2}$. Thus, the time rate change of the pressure is calculated by

$$\frac{\partial p}{\partial t} + \frac{c\rho}{\sqrt{2}}(\boldsymbol{L}_{\boldsymbol{\zeta},4} + \boldsymbol{L}_{\boldsymbol{\zeta},5}) + \boldsymbol{b}_{\boldsymbol{\zeta},5} = 0 \tag{2.57}$$

and, additionally, for the no–slip boundary condition, the velocities at the wall are set to zero.

Further, an additional boundary condition for the thermal state of the wall is necessary. Either an isothermal, by setting a specific wall temperature $T_\mathrm{w} = \mathrm{const}$, or an adiabatic wall boundary condition can be chosen in the solver. The latter condition in curvilinear coordinates reads

$$\begin{aligned} 0 = \frac{\partial T}{\partial n} = \frac{1}{\sqrt{\zeta_x^2 + \zeta_y^2 + \zeta_z^2}}\Big[&(\xi_x\zeta_x + \xi_y\zeta_y + \xi_z\zeta_z)\frac{\partial T}{\partial \xi} \\ &+(\eta_x\zeta_x + \eta_y\zeta_y + \eta_z\zeta_z)\frac{\partial T}{\partial \eta} \\ &+(\zeta_x\zeta_x + \zeta_y\zeta_y + \zeta_z\zeta_z)\frac{\partial T}{\partial \zeta}\Big]. \end{aligned} \tag{2.58}$$

In addition to these two thermal states at the wall, also a radiation–adiabatic wall boundary condition can be prescribed. This boundary condition reads

$$Q_\mathrm{w} = 0 = -\frac{\kappa}{\mathrm{Re}_\infty \mathrm{Pr}_\infty \mathrm{Ec}_\infty}\frac{\partial T}{\partial n} + \frac{\epsilon_\mathrm{rad}\sigma^*_\mathrm{SB}T^{*4}_\infty}{\rho^*_\infty V^{*3}_\infty}T^4 \tag{2.59}$$

with $\partial T/\partial n$ defined by Eq. (2.58) without setting the gradient to zero and

$$\mathrm{Ec}_\infty = (\gamma - 1)\mathrm{M}_\infty^2, \quad \mathrm{Ec}_\infty = \frac{V_\infty^{*2}}{c_{p\infty}^* T_\infty^*} \tag{2.60}$$

for the perfect gas model or the thermo–chemical equilibrium gas model, respectively. The equation is solved by a Newton iteration as

$$T_{\mathrm{new}} = T_{\mathrm{old}} - \frac{Q_{\mathrm{w}}}{(\partial Q_{\mathrm{w}}/\partial T)_{\mathrm{old}}} \tag{2.61}$$

with the derivative of the heat flux with respect to the temperature T_{old} as

$$\left(\frac{\partial Q_{\mathrm{w}}}{\partial T}\right)_{\mathrm{old}} = \frac{\kappa}{\mathrm{Re}_\infty \mathrm{Pr}_\infty \mathrm{Ec}_\infty} \frac{3}{2} \sqrt{\zeta_x^2 + \zeta_y^2 + \zeta_z^2} + \frac{4\epsilon_{\mathrm{rad}} \sigma_{\mathrm{SB}}^* T_\infty^{*4}}{\rho_\infty^* V_\infty^{*3}} T_{\mathrm{old}}^3 \tag{2.62}$$

if a one–sided finite–difference of second order is applied in the ζ–direction in Eq. (2.58). The thermal conductivity κ is recalculated in each iteration step and the Newton iteration is performed until $|T_{\mathrm{new}} - T_{\mathrm{old}}| < \Delta$, where Δ is a small number. [74]

Additional boundary conditions are required for the free–stream, the outflow, in the spanwise direction and at the symmetry line. To set these boundary conditions, ghost points are placed in these regions. Additionally, ghost points are also placed inside the wall to sustain the spatial second–order accuracy of the calculation at the grid point aside of the wall ($j = 1$). The flow variables at the ghost points around the computational domain are set as follows. In the free–stream, the free–stream flow conditions are specified. Inside the wall, the primitive flow variables $\boldsymbol{q}$ at the ghost points are calculated by a second–order extrapolation from inside of the flow–field. In the outflow, either the same second–order extrapolation is applied requiring $\partial^2 \boldsymbol{q}/\partial \xi^2 = 0$ or the variables are prescribed requiring $\partial \boldsymbol{q}/\partial \xi = 0$ [42] depending on the numerical stability of the boundary condition for the actual test case, where the

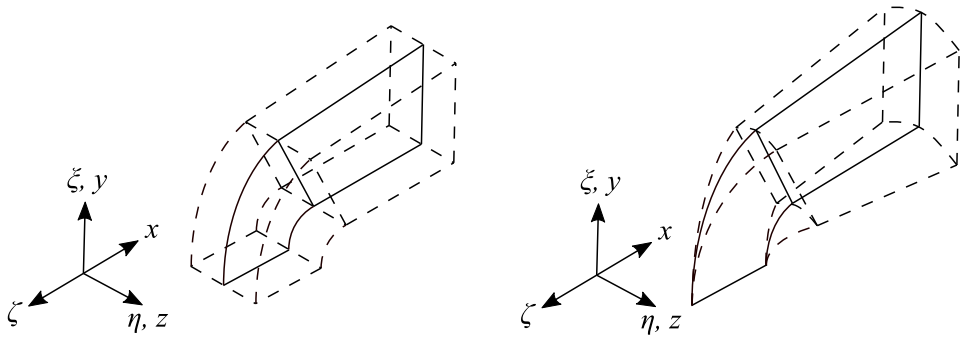

(a) 2D–planar (b) 2D-axisymmetric

Figure 2.4: Ghost point placement for the boundary conditions in the spanwise direction.

first boundary condition is preferred due to the more physical representation of the outflow. In the spanwise direction, the boundary conditions are applied depending on the test case dimension (2D, 2D–axisymmetric or 3D), where in all cases the 3D governing equations Eq. (2.1) are solved without simplifications. In the 2D case and the 2D–axisymmetric case, the pressure, density and curvilinear velocity components remain the same at the ghost points in the spanwise direction (dashed lines in Fig. 2.4) as on the calculation plane (solid lines in Fig. 2.4). The difference between these two flow cases is achieved by the different generation of the ghost points in the spanwise direction. For 2D cases, the ghost points are placed by a translation of the grid points in the z–direction (see Fig. 2.4a). For the 2D–axisymmetric case, the ghost points are set by a rotation of the grid points around the x–axis (see Fig. 2.4b). In the 3D case, where in case of CONSST3D half of the geometry is calculated, the flow variables are mirrored around the x/y–plane. At the symmetry line, the distinction between the cases is also made. In the 2D/2D–axisymmetric case, all flow variables are mirrored around the symmetry line except $v_{-1,j,l} = -v_{1,j,l}$. For 3D calculations, the flow variables are exchanged between the upper and the lower part of the computed geometry. [90]

2.3.4 Mesh Adaption

In super– and hypersonic flows, investigated in this work, a bow shock arises in front of the geometries (see Fig. 2.1). Bow shocks are a discontinuity in the flow–field and require a special treatment to accurately calculate the flow variables behind the shock. Mainly, two approaches are available in the literature to adequately treat this discontinuity. The first approach is the shock–fitting method. In this method, the shock is the outer boundary of the computational domain and the unsteady Rankine-Hugoniot relations are solved at this location [61, 68]. The advantages of the shock–fitting method are the reduced computational domain because the free–stream can be excluded from the calculation and, additionally, no clustering of the grid points at the shock is necessary [61]. Nevertheless, issues arise in computing long slender geometries with regard to the stability of the calculation due to the moving mesh [42]. To overcome these stability issues, another approach is applied in this work. This second approach is the shock–capturing method in which the shock lies inside the computational domain and is treated by the same governing equations Eq. (2.1) as the interior points. Typically, the bow shock is resolved by three grid points [42] and, thus, to adequately capture the shock in this approach, the mesh needs to be aligned with and refined at the shock.

To place the grid points at the shock, the shock location has to be determined and the mesh has to be aligned with the shock. Therefore, a mesh adaption is implemented in the solver as follows. The shock condition

$$\begin{cases} \mathrm{M}_n \geq 1 & \text{upstream of the shock} \\ \mathrm{M}_n < 1 & \text{downstream of the shock} \end{cases} \tag{2.63}$$

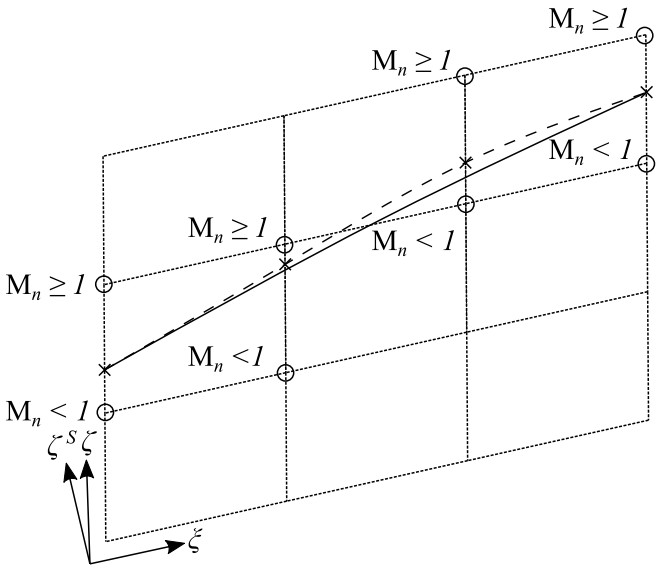

Figure 2.5: Schematic sketch of the mesh adaption.

with the shock normal Mach number

$$\mathrm{M}_n = \frac{(u\zeta_x^{\mathrm{S}} + v\zeta_y^{\mathrm{S}} + w\zeta_z^{\mathrm{S}})/\sqrt{\zeta_x^{\mathrm{S}^2} + \zeta_y^{\mathrm{S}^2} + \zeta_z^{\mathrm{S}^2}}}{c} \tag{2.64}$$

is used to detect the grid points next to the shock ($\circ$ in Fig. 2.5). The required shock metric terms ζ_x^{S}, ζ_y^{S} and ζ_z^{S} of Eq. (2.64) can be calculated by transforming the streamwise metric derivatives as described in [73]. In a next step, a linear interpolation in the ζ–direction is performed to determine the exact shock location by requiring $\mathrm{M}_n = 1$ ($\times$ in Fig. 2.5). This process results in the shock shape represented by the dashed line. Next, the smoothing procedure found in [42] is applied to the determined shock distance from the wall in the streamwise direction as

$$n_{s(i,j,l)} = \frac{1}{4}(n_{s(i-1,j,l)} + 2n_{s(i,j,l)} + n_{s(i+1,j,l)}) \tag{2.65}$$

to remove numerical inaccuracies/oscillations from the shock shape to get the shock shape for the further calculations represented by the solid line. Note that this smoothing procedure is additionally performed in the spanwise direction for 3D calculations. In a last step, the new mesh is aligned with the previous estimated shock shape and the flow variables are interpolated onto the new mesh by a linear interpolation. [90]

2.3.5 Treatment of the Singular Line

Due to the discretization with finite–differences in general curvilinear coordinates, a metric singularity arises at the symmetry line of blunt bodies [66] (red line in Fig. 2.6). This singularity is caused by the transformation of the Cartesian coordinates to the general curvilinear coordinates and, thus, is of a non–physical nature. Because

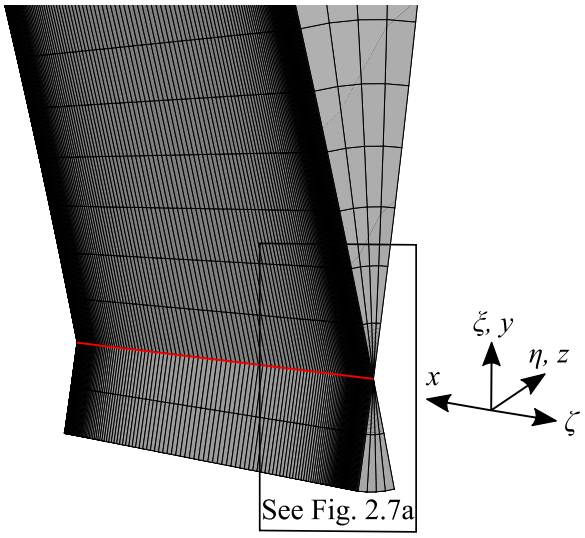

Figure 2.6: "Metric singularity (red line) at the nose of a blunt body configuration on the body-orientated mesh" adapted from [90] is licensed under CC BY 4.0 `http://creativecommons.org/licenses/by/4.0/`.

the spatial derivatives of the Cartesian coordinates x, y and z with respect to the spanwise curvilinear coordinate η vanish due to the collapse of all grid lines at the symmetry line shown in Fig. 2.6, the determinant of the metric Jacobian J^{-1} becomes zero (see Eq. (2.7)). In consequence, the discretization of Eq. (2.1) is impossible at

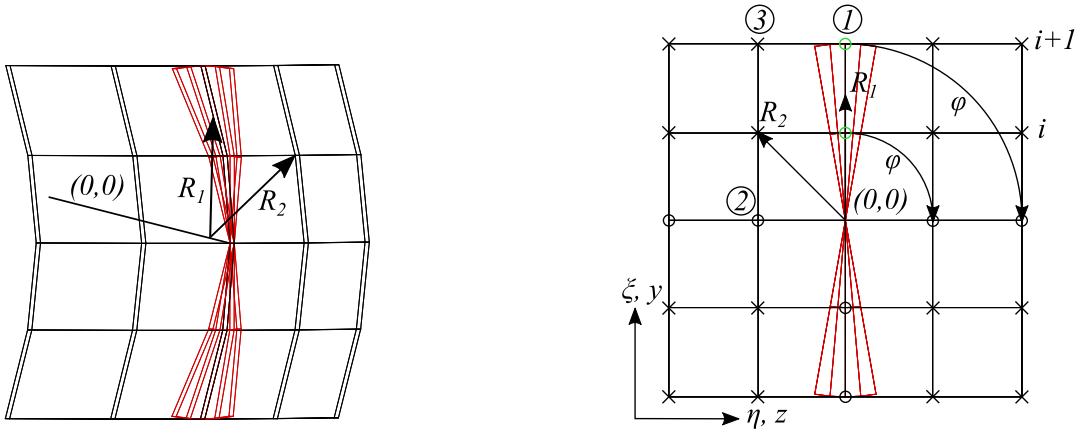

(a) Detailed view of Fig. 2.6

(b) Illustration of the overset mesh generation

Figure 2.7: "Overset mesh at the symmetry line for 2D-axisymmetric calculations: Body-orientated mesh (red lines), Overset mesh (black lines)" adapted from [90] is licensed under CC BY 4.0 `http://creativecommons.org/licenses/by/4.0/`.

the symmetry line in this coordinate system because the curvilinear state vector $J^{-1}\boldsymbol{Q}$ becomes zero which is non–physical. To overcome this issue, the fully conservative overset mesh method of Teschner & Mundt [90] is implemented in CONSST3D and will be outlined in the following. The overset mesh is generated by avoiding the collapse of the grid lines. Therefore, a hexahedral structure is used which is presented for two grid surfaces in the ζ–direction in black color in Fig. 2.7a. Further, a coincidence is required between the grid points of the body–orientated mesh (red lines in Fig. 2.7b) and the grid points of the overset mesh (black lines in Fig. 2.7b). This requirement enables the conservation of the flow variables because the flow variables can be interchanged between the meshes without applying interpolation techniques. To ensure this coincidence, the grid points are placed as follows. The coordinates of the calculation points (green $\circ$) on the overset mesh are equal to the respective coordinates of the grid points on the body–orientated mesh. Further, the grid points to apply the boundary conditions (black $\circ$) are calculated by rotating the calculation points around the symmetry line ((0,0)) by $\varphi = 90^\circ$, 180° and 270°. Lastly, the metric points (black $\times$), that are required to calculate the metric terms at the calculation and boundary condition points, are placed as follows. As an example, due to the placement of the overset mesh, the y–coordinate of point ③ equals the y–coordinate of point ① and the z–coordinate of point ③ equals the z–coordinate of point ②. With these coordinates, the respective x–coordinates of the metric points are calculated by

$$x = \frac{R_1 - y_{(i)}}{y_{(i+1)} - y_{(i)}}(x_{(i+1)} - x_{(i)}) + x_{(i)}, \tag{2.66}$$

where

$$R_1 = R_2, \quad \text{with} \quad R_2 = \sqrt{y^2 + z^2} \tag{2.67}$$

which is valid for 2D-axisymmetric flows, where the shock distance remains constant in the spanwise direction. The exchange of the flow variables between the two meshes is performed in the following way. The flow variables at the calculation points are equal on both meshes and, thus, the overset mesh can receive the variables directly from the body–orientated mesh. The flow variables at the boundary condition points on the overset mesh are calculated by the boundary condition in the spanwise direction for 2D–axisymmetric calculations in Sec. 2.3.3. Lastly, the flow variables at the symmetry line on the body–orientated mesh can be received directly from the overset mesh because the mesh points coincide.

Additionally, due to the indefinite metric at the singular line and the local averaging of the metric terms for the flux reconstruction (see Sec. 2.3.1), the metric calculation on the body–orientated mesh has to be modified for the discretization of the first point downstream of the symmetry line ($i = 1$). Therefore, firstly, the metric terms describing the derivative of the Cartesian coordinates with respect to the curvilinear coordinates, e.g., x_ξ, are averaged between $i = 0$ and $i = 1$ to get the values at $i = 1/2$. Secondly, due to the resulting definite metric, the inversion to calculate the inverse transformation, e.g., ξ_x, is performed at $i = 1/2$ to enable the flux reconstruction at $i = 1$.

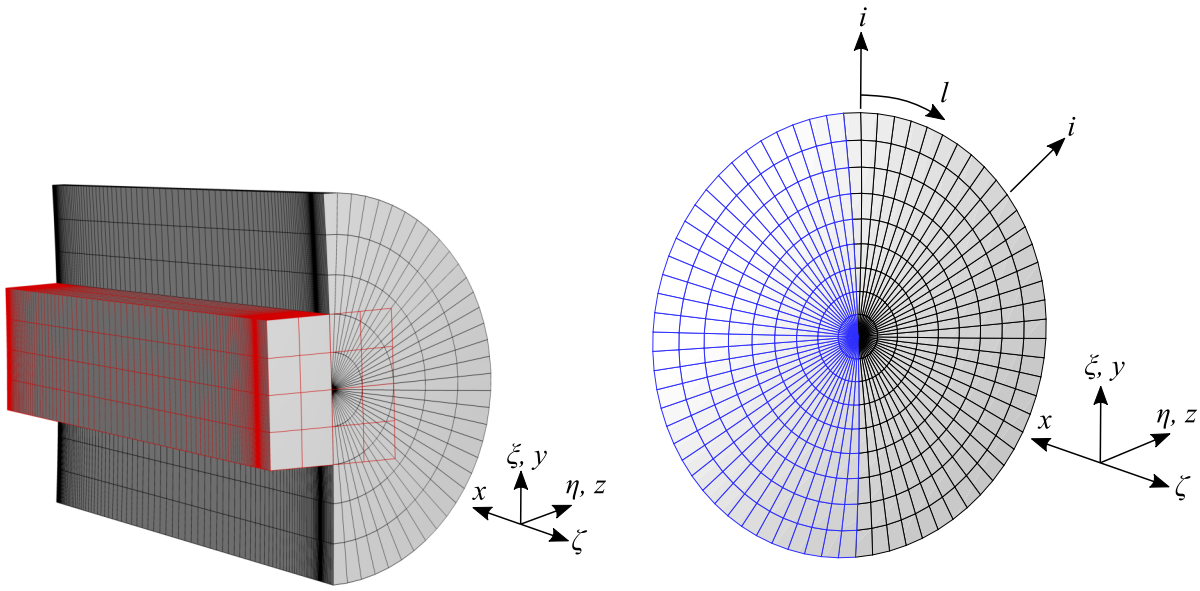

(a) "Overset Mesh for the discretization of the governing equations" adapted from [90] is licensed under CC BY 4.0 http://creativecommons.org/licenses/by/4.0/

(b) "Surface fitting method for one grid surface in the ζ–direction" adapted from [90] is licensed under CC BY 4.0 http://creativecommons.org/licenses/by/4.0/

Figure 2.8: Overset mesh generation for 3D calculations.

In case of 3D calculations, where the assumption of a constant shock distance in the spanwise direction is not valid anymore, the overset mesh presented in red color in Fig. 2.8a is generated as follows. To calculate the coordinates, each grid plane in the ζ–direction, by choosing 10 grid points on each spanwise grid line l (see Fig. 2.8b), is treated separately. Firstly, the grid points of the body–orientated mesh of half of the geometry are mirrored around the x/y–plane (blue lines in Fig. 2.8b). Thereafter, the coefficients a_0, a_1, a_2 and $a_{l,i}$ for the surface fitting method developed by Harder and Desmarais [23] as

$$x = a_0 + a_1 y + a_2 z + \sum_{l=0}^{l_{\max}-1} \sum_{i=0}^{i_{\max}-1} a_{(l,i)} r^2_{(l,i)} \ln r^2_{(l,i)} \tag{2.68}$$

with $r^2_{(l,i)} = (y - y_{(l,i)})^2 + (z - z_{(l,i)})^2$ are calculated on each of these grid planes. Knowing the coefficients, the x–coordinates of the calculation points, boundary condition points and metric points can be calculated by Eq. (2.68), where the y– and z–coordinates can be determined as explained for the 2D–axisymmetric case. The interchange of the flow variables is performed as follows. The flow variables on the overset mesh at the calculation points and the boundary condition points can be received directly from the body–orientated mesh at $\varphi = 0°$, $90°$ and $180°$ and at $\varphi = 270°$ by mirroring the flow variables around the x/y–axis as explained in Sec. 2.3.3. Similar to the 2D–axisymmetric case, the flow variables at the symmetry line

on the body–orientated mesh are received directly from the overset mesh. Further, the metric terms for the discretization of the first point downstream of the singularity are calculated analogous to the 2D–axisymmetric case but for each grid line in the spanwise direction. Note, that in both cases, 2D–axisymmetric and 3D, the same governing equations Eq. (2.1) are solved on the two meshes with the respective metric terms.

2.3.6 Computational Grid Generation and Flow–Field Initialization

The generation of the computational grid is performed in different ways depending on whether flat plates or blunted geometries, e.g., blunted cones or cylinder wedges, are calculated. In the streamwise direction, for both cases, a stretching function as

$$\Psi_i = 1 + \beta_s \frac{1 - \left(\frac{\beta_s+1}{\beta_s-1}\right)^{1-h_i}}{1 + \left(\frac{\beta_s+1}{\beta_s-1}\right)^{1-h_i}} \tag{2.69}$$

with the stretching factor β_s and

$$h_i = \frac{i-1}{i_{\max}-1}, \quad \text{with } i = 2, ..., i_{\max} - 1 \tag{2.70}$$

is applied to enable a clustering at the front tip of flat plates or the nose part of blunted geometries [42]. This stretching function is applied in different ways to the calculation of the grid points at the wall. For the flat plate case, it is directly applied to calculate the x–coordinates of the grid points, where the y–coordinate is held constant ($y^* = 0$). For blunted geometries, the stretching function is applied to the arclength s to thereafter calculate the x–coordinates by

$$x^* = \begin{cases} (-\cos(s))R_N^* & \text{for } s \leq \frac{1}{2}\pi - \Theta \\ ((s - \frac{1}{2}\pi + \Theta)\cos\Theta - \sin\Theta)R_N^* & \text{for } s > \frac{1}{2}\pi - \Theta \end{cases} \tag{2.71}$$

[105]. Subsequently, the y–coordinates along the wall can be calculated by the geometrical relations of a circle or a line for the nose part and the straight part, respectively.

The main difference between the two cases arise at the outer boundary of the computational domain and the grid distribution in the wall normal direction. For blunted geometries, the outer boundary of the computational domain is initialized by the intersection points of the wall normal grid lines with Billig's correlation given by

$$x^* = R_N^* + \Delta_s^* - R_c^* \text{cotan}^2\Theta \left[\left(1 + \frac{y^{*2}\tan^2\Theta}{R_c^{*2}} \right)^{1/2} - 1 \right], \tag{2.72}$$

with

$$\Delta_s^* = 0.143\exp\left(3.24/\mathrm{M}_\infty^2\right) R_N^*, \tag{2.73}$$

$$R_c^* = 1.143\exp\left(0.54/(\mathrm{M}_\infty - 1)^{1.2}\right) R_N^* \tag{2.74}$$

for blunted cones and

$$\Delta_s^* = 0.386\exp\left(4.67/\mathrm{M}_\infty^2\right) R_N^*, \tag{2.75}$$

$$R_c^* = 1.386\exp\left(1.8/(\mathrm{M}_\infty - 1)^{0.75}\right) R_N^* \tag{2.76}$$

for cylinder wedges [5]. Thereafter, the grid point distribution in the wall normal direction between the wall and the shock is generated by the one–dimensional stretching function of Vinokur [98]. By applying this stretching function, a clustering of the grid points at the wall and at the shock can be achieved without discontinuities in the distribution. Further, in this work 20 of the wall normal grid points are mirrored at the shock for the free–stream, comparable to Kufner et al. [43]. For flat plates, a constant distance from the wall $y^* = \text{const}$ is used as the outer boundary, where care must be taken that the shock is inside the computational domain. Additionally, the grid points are only clustered at the wall using the same stretching function as for the blunted geometries but without a clustering at the outer boundary. This is the case because no alignment of the grid with the shock is possible in this case due to the resulting collapse of all grid lines at the front tip of the flat plate. Note that in case of 3D calculations of blunted cones, respectively, considering an angle of attack, the initial grid distribution is rotated around the x–axis to generate the mesh for half of the geometry (0° - 180°). Further, the outer boundary of the computational domain, calculated by Billig's correlation, can be multiplied by a prescribed factor to take into account the 3D effects on the shock location, respectively, guaranteeing that the shock lies inside the computational domain before the first mesh adaption is applied.

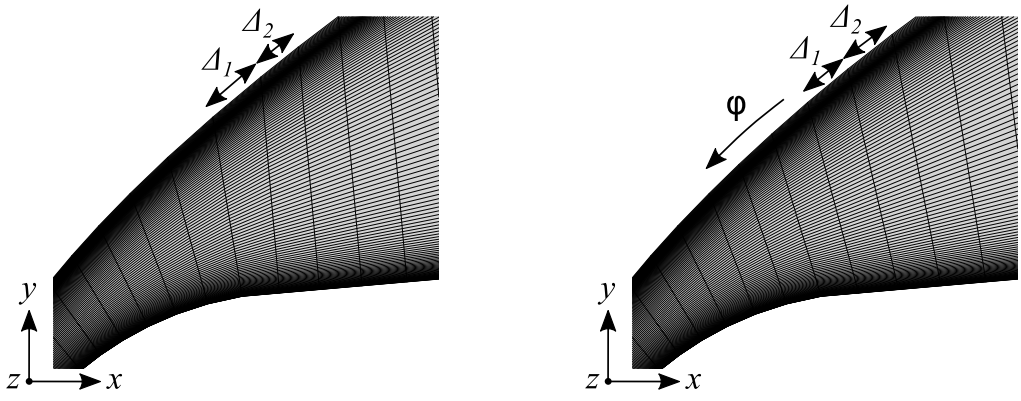

(a) Mesh with discontinuity (b) Adjusted mesh without discontinuity

Figure 2.9: Mesh discontinuity for blunted geometries.

In case of blunted geometries, a mesh discontinuity (see Fig. 2.9a), which results in inaccuracies in the flow–field, arises at the junction between the nose and the straight part by using wall normal grid lines. These flow–field inaccuracies arise because the increment between the mesh distances Δ_1 and Δ_2 exceed 10 % [42]. Thus, to improve the grid quality at this location, the wall normal grid lines are manually adjusted by a small angle φ, see Fig. 2.9b, to enable a smooth transition of the grid lines from the nose to the straight part. This adjustment angle is restricted to be below 10° to maintain the thin–layer Navier–Stokes approximation [42].

Two approaches are available to initialize the flow variables. In the first approach, the flow–field is initialized by prescribing the free–stream flow variables in the whole computational domain, whereas, in the second approach, the Rankine–Hugoniot shock relations are applied. For the latter, the shock metrics, see Sec. 2.3.4, and the free–stream values are used to calculate the flow variables downstream of the shock inside the shock–layer. These calculated values are prescribed constant along each wall normal grid line. Upstream of the shock, the free–stream values are set. The advantage of this approach is a decrease of the computational time to steady state as the initial flow–field inside the shock–layer resembles the steady state flow–field more likely.

Chapter 3

Boundary-Layer Stability Solver

3.1 Governing Equations

The second solver, developed in this work, is a boundary–layer stability solver, named COSTAS (COmpressible STAbility Solver) [92]. The governing equations of this solver are derived from the compressible Navier–Stokes equations in the primitive form as

$$0 = \frac{\partial \rho}{\partial t} + \left(\rho v^k\right)_{,k} \quad (k = 1,2,3), \tag{3.1}$$

$$\begin{aligned} 0 =& \rho \frac{\partial v^k}{\partial t} + \rho v^m v^k_{,m} + p_{,m} g^{km} - \frac{1}{\mathrm{Re}_\infty} \left(g^{km} \frac{\partial}{\partial x^m} \left(\lambda_s \frac{1}{\sqrt{g}} \frac{\partial}{\partial x^o} \left(v^o \sqrt{g} \right) \right) \right. \\ &+ \left. \frac{1}{\sqrt{g}} \frac{\partial}{\partial x^m} \left(\mu \sqrt{g} \left(g^{kp} v^m_{,p} + g^{mr} v^k_{,r} \right) \right) + \Gamma^k_{mo} \mu \left(g^{mp} v^o_{,p} + g^{or} v^m_{,r} \right) \right) \\ & (k = 1 \vee 2 \vee 3), \quad (m,o,p,r = 1,2,3), \end{aligned} \tag{3.2}$$

$$\begin{aligned} 0 =& \rho \frac{\partial h}{\partial t} + \rho v^k h_{,k} - \mathrm{Ec}_\infty \left(\frac{\partial p}{\partial t} + v^k p_{,k} \right) - \frac{1}{\mathrm{Re}_\infty \mathrm{Pr}_\infty} \left(\frac{1}{\sqrt{g}} \frac{\partial}{\partial x^k} \left(\sqrt{g} \kappa g^{km} T_{,m} \right) \right) \\ &- \frac{\mathrm{Ec}_\infty}{\mathrm{Re}_\infty} g_{ko} \left(\lambda_s v^p_{,p} g^{om} + \mu \left(g^{op} v^m_{,p} + g^{mr} v^o_{,r} \right) \right) v^k_{,m} \quad (k,m,o,p,r = 1,2,3) \end{aligned} \tag{3.3}$$

[45, 67, 70]. These equations are written in the non–dimensional form in general curvilinear coordinates in tensor notation, where the Einstein summation convention is used. The energy equation Eq. (3.3) will be applied unchanged in the case of calculations in thermo–chemical equilibrium. In case of considering a perfect gas, the enthalpy $h = c_p T$ is replaced by T because of the constant heat capacity, respectively, $c_p = 1$. Note that the curvilinear coordinates and velocity components in this section correspond to the respective counterparts in Fig. 2.1, respectively, $x^1 = \xi$, $x^2 = \zeta$, $x^3 = \eta$, $v^1 = v_\xi$, $v^2 = v_\zeta$ and $v^3 = v_\eta$.

For the calculation of the metric tensors g_{km} and g^{km} and the Christoffel symbols of the second kind Γ^k_{mo}, the derivatives of the Cartesian coordinates with respect to

the curvilinear coordinates, e.g., $\partial x/\partial x^2$, can be calculated by finite–differences of fourth–order or a Chebyshev spectral collocation method depending on the applied spatial discretization scheme in the respective direction explained in Sec. 3.3.1. With these derivatives, the covariant metric tensors are calculated by

$$g_{km} = \frac{\partial x}{\partial x^k}\frac{\partial x}{\partial x^m} + \frac{\partial y}{\partial x^k}\frac{\partial y}{\partial x^m} + \frac{\partial z}{\partial x^k}\frac{\partial z}{\partial x^m}. \tag{3.4}$$

With the orthogonality relation $g_{km}g^{kl} = \boldsymbol{\delta}^l_m$ with the Kronecker tensor $\boldsymbol{\delta}^l_m$, the contravariant metric tensor is

$$g^{kl} = \frac{1}{g}(g_{mp}g_{or} - g_{mr}g_{op}) \tag{3.5}$$

with g being the determinant of the metric tensor and the indices (k, m, o) and (l, p, r) are cyclic. Lastly, the Christoffel symbols of the second kind are defined by

$$\Gamma^o_{km} = \frac{1}{2}g^{lo}\left(\frac{\partial g_{ml}}{\partial x^k} + \frac{\partial g_{kl}}{\partial x^m} - \frac{\partial g_{km}}{\partial x^l}\right) \tag{3.6}$$

[4, 27, 45]. Note that in Sec. 4 and Sec. 5 the physical velocity components are presented which are given by, e.g., $v_t = v^1\sqrt{g_{11}}$.

The non–dimensionalization is performed in the same way as for CONSST3D, explained in Sec. 2.1, but with the Blasius length scale as the reference length. This length and the other non–dimensional parameters are

$$L^*_\infty = \sqrt{\frac{\mu^*_\infty s^*}{\rho^*_\infty V^*_\infty}}, \quad \mathrm{M}_\infty = \frac{V^*_\infty}{c^*_\infty}, \quad \mathrm{Re}_\infty = \frac{\rho^*_\infty V^*_\infty L^*_\infty}{\mu^*_\infty}, \quad \mathrm{Pr}_\infty = \frac{\mu^*_\infty c^*_{p\infty}}{\kappa^*_\infty} \tag{3.7}$$

with a distinction of the Eckert number between the perfect gas case (PG) and the thermo–chemical equilibrium gas case (TCE) as

$$\mathrm{Ec}_\infty = (\gamma - 1)\mathrm{M}^2_\infty \text{ (PG)}, \quad \mathrm{Ec}_\infty = \frac{V^{*2}_\infty}{c^*_{p_\infty} T^*_\infty} \text{ (TCE)} \tag{3.8}$$

[56, 104]. Note that in the LST, the non–dimensionalization is performed with the reference length at the respective surface location, whereas in case of the LPSE the reference length at the initial location is used [104]. Thus, in case of LST calculations along the surface of the geometry, the non–dimensional coordinates, the metric terms, the curvilinear velocities and the non–dimensional spatial derivatives of the flow variables have to be recomputed for the calculation at each streamwise location.

To derive the stability equations, firstly, a disturbance part, which is assumed to be small with respect to the base–flow variables, is added to the velocity components, the thermodynamic variables as well as to the transport variables. Thus, the flow variables are replaced by

$$\boldsymbol{q}(x^1,x^2,x^3,t) = \bar{\boldsymbol{q}}(x^1,x^2,x^3) + \boldsymbol{q}'(x^1,x^2,x^3,t) \tag{3.9}$$

with the laminar base–flow variables $\bar{\mathbf{q}}$ from CONSST3D and the disturbance flow variables $\boldsymbol{q}'$. These variables are inserted into Eq. (3.1) – (3.3), the laminar base–flow is subtracted from the equations and the resulting equations are linearized to get the linearized disturbance equations as

$$\begin{aligned}&\bar{\boldsymbol{T}}_{\boldsymbol{t}}\frac{\partial \boldsymbol{q}'}{\partial t}+\bar{\boldsymbol{A}}_{\boldsymbol{x^1}}\frac{\partial \boldsymbol{q}'}{\partial x^1}+\bar{\boldsymbol{B}}_{\boldsymbol{x^2}}\frac{\partial \boldsymbol{q}'}{\partial x^2}+\bar{\boldsymbol{C}}_{\boldsymbol{x^3}}\frac{\partial \boldsymbol{q}'}{\partial x^3}+\bar{\boldsymbol{D}}_{\boldsymbol{0}}\boldsymbol{q}'\\ =&\bar{\boldsymbol{V}}_{\boldsymbol{x^1x^1}}\frac{\partial^2 \boldsymbol{q}'}{\partial x^1 x^1}+\bar{\boldsymbol{V}}_{\boldsymbol{x^2x^2}}\frac{\partial^2 \boldsymbol{q}'}{\partial x^2 x^2}+\bar{\boldsymbol{V}}_{\boldsymbol{x^3x^3}}\frac{\partial^2 \boldsymbol{q}'}{\partial x^3 x^3}\\ +&\bar{\boldsymbol{V}}_{\boldsymbol{x^1x^2}}\frac{\partial^2 \boldsymbol{q}'}{\partial x^1 x^2}+\bar{\boldsymbol{V}}_{\boldsymbol{x^1x^3}}\frac{\partial^2 \boldsymbol{q}'}{\partial x^1 x^3}+\bar{\boldsymbol{V}}_{\boldsymbol{x^2x^3}}\frac{\partial^2 \boldsymbol{q}'}{\partial x^2 x^3}.\end{aligned} \tag{3.10}$$

A wave–like ansatz as

$$\boldsymbol{q}'(x^1,x^2,x^3,t)=\tilde{\boldsymbol{q}}(x^1,x^2)e^{i(\Phi(x^1,x^3,t))}+c.c. \tag{3.11}$$

with

$$\frac{\partial \Phi}{\partial t}=-\omega,\quad \frac{\partial \Phi}{\partial x^1}=\frac{\alpha}{\sqrt{g_{11}}},\quad \frac{\partial \Phi}{\partial x^3}=\frac{\beta}{\sqrt{g_{33}}} \tag{3.12}$$

is applied to Eq. (3.10), where the non–dimensional angular disturbance frequency and streamwise and spanwise wave–numbers are

$$\omega=\frac{f^*2\pi L^*_\infty}{V^*_\infty},\quad \alpha=\alpha^* L^*_\infty,\quad \beta=\beta^* L^*_\infty. \tag{3.13}$$

Note that the metric tensors in Eq. (3.12) appear due to the physical representation of the wave–numbers in COSTAS. Further, in this work, the spatial theory is applied, where the angular frequency ω and the spanwise wave–number β are real numbers, whereas the streamwise wave–number α is a complex number. Additionally, only two–dimensional disturbances on the centerline of the geometries will be investigated in this work, respectively, $\beta=0$. The resulting system of equations is

$$\boldsymbol{A}_{\boldsymbol{x^1}}\frac{\partial \tilde{\boldsymbol{q}}}{\partial x^1}+\boldsymbol{B}_{\boldsymbol{x^2}}\frac{\partial \tilde{\boldsymbol{q}}}{\partial x^2}+\boldsymbol{D}_{\boldsymbol{0}}\tilde{\boldsymbol{q}}=\boldsymbol{V}_{\boldsymbol{x^2x^2}}\frac{\partial^2 \tilde{\boldsymbol{q}}}{\partial x^2 x^2} \tag{3.14}$$

with

$$\boldsymbol{A}_{\boldsymbol{x^1}}=\bar{\boldsymbol{A}}_{\boldsymbol{x^1}}-2i\frac{\alpha}{\sqrt{g_{11}}}\bar{\boldsymbol{V}}_{\boldsymbol{x^1x^1}}-i\frac{\beta}{\sqrt{g_{33}}}\bar{\boldsymbol{V}}_{\boldsymbol{x^1x^3}} \tag{3.15}$$

$$\boldsymbol{B}_{\boldsymbol{x^2}}=\bar{\boldsymbol{B}}_{\boldsymbol{x^2}}-i\frac{\alpha}{\sqrt{g_{11}}}\bar{\boldsymbol{V}}_{\boldsymbol{x^1x^2}}-i\frac{\beta}{\sqrt{g_{33}}}\bar{\boldsymbol{V}}_{\boldsymbol{x^2x^3}} \tag{3.16}$$

$$\begin{aligned}\boldsymbol{D}_{\boldsymbol{0}}=&-i\omega\bar{\boldsymbol{T}}_{\boldsymbol{t}}+i\frac{\alpha}{\sqrt{g_{11}}}\bar{\boldsymbol{A}}_{\boldsymbol{x^1}}+i\frac{\beta}{\sqrt{g_{33}}}\bar{\boldsymbol{C}}_{\boldsymbol{x^3}}+\bar{\boldsymbol{D}}_{\boldsymbol{0}}+\frac{\alpha^2}{g_{11}}\bar{\boldsymbol{V}}_{\boldsymbol{x^1x^1}}+\frac{\alpha}{\sqrt{g_{11}}}\frac{\beta}{\sqrt{g_{33}}}\bar{\boldsymbol{V}}_{\boldsymbol{x^1x^3}}\\ &+\frac{\beta^2}{g_{33}}\bar{\boldsymbol{V}}_{\boldsymbol{x^3x^3}}-i\frac{1}{\sqrt{g_{11}}}\frac{\partial \alpha}{\partial x^1}\bar{\boldsymbol{V}}_{\boldsymbol{x^1x^1}}\end{aligned} \tag{3.17}$$

$$\boldsymbol{V}_{\boldsymbol{x^2x^2}}=\bar{\boldsymbol{V}}_{\boldsymbol{x^2x^2}} \tag{3.18}$$

which represents the linear parabolized stability equations (LPSE). By assuming a locally parallel flow, respectively, $\bar{v}^2 = 0$, $\partial\bar{\boldsymbol{q}}/\partial x^1 = 0$ and $\partial\tilde{\boldsymbol{q}}/\partial x^1 = 0$, the system of equations reduces to the linear stability theory (LST), which excludes the downstream evolution of the disturbances. [20, 42, 55]

3.2 Thermodynamic Models

3.2.1 Perfect Gas Model

The assumptions made for the perfect gas model in the Navier-Stokes solver, see Sec. 2.2.1, are also applied to COSTAS. Further, to reduce the set of equations in the stability calculations, the perfect gas equation is rewritten in the disturbance form as

$$\tilde{p} = \frac{\bar{\rho}\tilde{T} + \tilde{\rho}\bar{T}}{\gamma \mathrm{M}_\infty^2} \tag{3.19}$$

to replace the pressure in Eq. (3.1)–(3.3) [80]. Additionally, the transport properties are replaced by a Taylor–series expansion which reads for the viscosity, the thermal conductivity and the second coefficient of the viscosity as

$$\tilde{\mu} = \frac{\partial\bar{\mu}}{\partial\bar{T}}\tilde{T}, \quad \tilde{\kappa} = \frac{\partial\bar{\kappa}}{\partial\bar{T}}\tilde{T}, \quad \tilde{\lambda_s} = \frac{\partial\bar{\lambda_s}}{\partial\bar{T}}\tilde{T} \tag{3.20}$$

[55]. Thus, the resulting solution vector becomes $\tilde{\boldsymbol{q}} = [\tilde{\rho},\tilde{v}^1,\tilde{v}^2,\tilde{v}^3,\tilde{T}]^T$.

3.2.2 Thermo–Chemical Equilibrium Gas Model

Similar to the perfect gas case, the thermo–chemical equilibrium gas model of the Navier–Stokes solver, see Sec. 2.2.2, is implemented in COSTAS. Besides including the state surfaces, the representations of the disturbance variables of the thermodynamic and transport variables has to be modified. The transport variables are again estimated by a Taylor–series expansion but in this case with respect to two variables [56, 70]. In case of COSTAS, the temperature and the density are used resulting in

$$\tilde{\mu} = \frac{\partial\bar{\mu}}{\partial\bar{T}}\tilde{T} + \frac{\partial\bar{\mu}}{\partial\bar{\rho}}\tilde{\rho}, \quad \tilde{\kappa} = \frac{\partial\bar{\kappa}}{\partial\bar{T}}\tilde{T} + \frac{\partial\bar{\kappa}}{\partial\bar{\rho}}\tilde{\rho}, \quad \tilde{\lambda_s} = \frac{\partial\bar{\lambda_s}}{\partial\bar{T}}\tilde{T} + \frac{\partial\bar{\lambda_s}}{\partial\bar{\rho}}\tilde{\rho}. \tag{3.21}$$

Further, because Eq. (3.19) is not valid anymore, the pressure and in addition, to solve for the same solution vector $\tilde{\boldsymbol{q}}$ as for the perfect gas case, the enthalpy are also approximated by a Taylor–series expansion as

$$\tilde{p} = \frac{\partial\bar{p}}{\partial\bar{T}}\tilde{T} + \frac{\partial\bar{p}}{\partial\bar{\rho}}\tilde{\rho}, \quad \tilde{h} = \frac{\partial\bar{h}}{\partial\bar{T}}\tilde{T} + \frac{\partial\bar{h}}{\partial\bar{\rho}}\tilde{\rho} \tag{3.22}$$

[92].

3.3 Numerical Implementation

3.3.1 Spatial Discretization

The spatial discretization of the governing equations Eq. (3.14) is performed in different ways dependent on the spatial direction. Firstly, the wall normal direction will be treated in this section. Two types of discretization schemes are available in this direction, a fourth-order finite–difference scheme and a Chebyshev spectral collocation method. In the fourth–order finite–difference scheme, the discretization of the first derivatives at the interior points is performed with a central scheme for an equidistant computational grid as

$$\frac{\partial \tilde{\boldsymbol{q}}_{(i,j,l)}}{\partial x^2} = \frac{\tilde{\boldsymbol{q}}_{(i,j-2,l)} - 8\tilde{\boldsymbol{q}}_{(i,j-1,l)} + 8\tilde{\boldsymbol{q}}_{(i,j+1,l)} - \tilde{\boldsymbol{q}}_{(i,j+2,l)}}{12\Delta x^2}. \tag{3.23}$$

To account for the boundaries, the scheme is modified to

$$\frac{\partial \tilde{\boldsymbol{q}}_{(i,j,l)}}{\partial x^2} = \frac{-3\tilde{\boldsymbol{q}}_{(i,j-1,l)} - 10\tilde{\boldsymbol{q}}_{(i,j,l)} + 18\tilde{\boldsymbol{q}}_{(i,j+1,l)} - 6\tilde{\boldsymbol{q}}_{(i,j+2,l)} + 1\tilde{\boldsymbol{q}}_{(i,j+3,l)}}{12\Delta x^2}, \tag{3.24}$$

$$\frac{\partial \tilde{\boldsymbol{q}}_{(i,j,l)}}{\partial x^2} = \frac{-1\tilde{\boldsymbol{q}}_{(i,j-3,l)} + 6\tilde{\boldsymbol{q}}_{(i,j-2,l)} - 18\tilde{\boldsymbol{q}}_{(i,j-1,l)} + 10\tilde{\boldsymbol{q}}_{(i,j,l)} + 3\tilde{\boldsymbol{q}}_{(i,j+1,l)}}{12\Delta x^2} \tag{3.25}$$

for the point aside of the wall and the point aside of the outer boundary, respectively, and to

$$\frac{\partial \tilde{\boldsymbol{q}}_{(i,j,l)}}{\partial x^2} = \frac{-25\tilde{\boldsymbol{q}}_{(i,j,l)} + 48\tilde{\boldsymbol{q}}_{(i,j+1,l)} - 36\tilde{\boldsymbol{q}}_{(i,j+2,l)} + 16\tilde{\boldsymbol{q}}_{(i,j+3,l)} - 3\tilde{\boldsymbol{q}}_{(i,j+4,l)}}{12\Delta x^2}, \tag{3.26}$$

$$\frac{\partial \tilde{\boldsymbol{q}}_{(i,j,l)}}{\partial x^2} = \frac{3\tilde{\boldsymbol{q}}_{(i,j-4,l)} - 16\tilde{\boldsymbol{q}}_{(i,j-3,l)} + 36\tilde{\boldsymbol{q}}_{(i,j-2,l)} - 48\tilde{\boldsymbol{q}}_{(i,j-1,l)} + 25\tilde{\boldsymbol{q}}_{(i,j,l)}}{12\Delta x^2} \tag{3.27}$$

directly at the wall and at the outer boundary. For the discretization of the second derivatives, the scheme is reduced to a third–order finite-difference defined as

$$\frac{\partial^2 \tilde{\boldsymbol{q}}_{(i,j,l)}}{\partial x^{2^2}} = \frac{-\tilde{\boldsymbol{q}}_{(i,j-2,l)} + 16\tilde{\boldsymbol{q}}_{(i,j-1,l)} - 30\tilde{\boldsymbol{q}}_{(i,j,l)} + 16\tilde{\boldsymbol{q}}_{(i,j+1,l)} - \tilde{\boldsymbol{q}}_{(i,j+2,l)}}{12\Delta x^{2^2}} \tag{3.28}$$

for the interior points. Analogous to the first derivatives, the scheme is modified at the point next to the wall and next to the outer boundary to

$$\frac{\partial^2 \tilde{\boldsymbol{q}}_{(i,j,l)}}{\partial x^{2^2}} = \frac{11\tilde{\boldsymbol{q}}_{(i,j-1,l)} - 20\tilde{\boldsymbol{q}}_{(i,j,l)} + 6\tilde{\boldsymbol{q}}_{(i,j+1,l)} + 4\tilde{\boldsymbol{q}}_{(i,j+2,l)} - 1\tilde{\boldsymbol{q}}_{(i,j+3,l)}}{12\Delta x^{2^2}}, \tag{3.29}$$

$$\frac{\partial^2 \tilde{\boldsymbol{q}}_{(i,j,l)}}{\partial x^{2^2}} = \frac{-1\tilde{\boldsymbol{q}}_{(i,j-3,l)} + 4\tilde{\boldsymbol{q}}_{(i,j-2,l)} + 6\tilde{\boldsymbol{q}}_{(i,j-1,l)} - 20\tilde{\boldsymbol{q}}_{(i,j,l)} + 11\tilde{\boldsymbol{q}}_{(i,j+1,l)}}{12\Delta x^{2^2}} \tag{3.30}$$

and directly at the wall and at the outer boundary to

$$\frac{\partial^2 \tilde{\boldsymbol{q}}_{(i,j,l)}}{\partial x^{2^2}} = \frac{35\tilde{\boldsymbol{q}}_{(i,j,l)} - 104\tilde{\boldsymbol{q}}_{(i,j+1,l)} + 114\tilde{\boldsymbol{q}}_{(i,j+2,l)} - 56\tilde{\boldsymbol{q}}_{(i,j+3,l)} + 11\tilde{\boldsymbol{q}}_{(i,j+4,l)}}{12\Delta x^{2^2}}, \tag{3.31}$$

$$\frac{\partial^2 \tilde{\boldsymbol{q}}_{(i,j,l)}}{\partial x^{2^2}} = \frac{11\tilde{\boldsymbol{q}}_{(i,j-4,l)} - 56\tilde{\boldsymbol{q}}_{(i,j-3,l)} + 114\tilde{\boldsymbol{q}}_{(i,j-2,l)} - 104\tilde{\boldsymbol{q}}_{(i,j-1,l)} + 35\tilde{\boldsymbol{q}}_{(i,j,l)}}{12\Delta x^{2^2}}. \tag{3.32}$$

Note that in this work the equidistant grid is generated with $\Delta x^2 = 1$.

A second, more accurate, approach found in the literature is the Chebyshev spectral collocation method. Following Malik [55], the method is applied in COSTAS as follows. To perform the discretization, firstly, the collocation points in the wall normal direction are determined by

$$x^2_{(i,j,l)} = \cos\frac{\pi j}{j_{\max}}, \quad \text{with } j = 0, ..., j_{\max}. \tag{3.33}$$

With these collocation points, secondly, the discretization stencils of the first derivatives are calculated by

$$\begin{aligned} \boldsymbol{E}_{\mathbf{Cheb}(jk)} &= \frac{c_j}{c_k}\frac{(-1)^{k+j}}{x^2_{(i,j,l)} - x^2_{(i,k,l)}}, \quad \text{for} j \neq k, \\ \boldsymbol{E}_{\mathbf{Cheb}(jj)} &= -\frac{x^2_{(i,j,l)}}{2(1 - x^{2^2}_{(i,j,l)})}, \\ \boldsymbol{E}_{\mathbf{Cheb}(00)} &= -\boldsymbol{E}_{\mathbf{Cheb}(j_{\max}j_{\max})} = \frac{2j^2_{\max} + 1}{6} \end{aligned} \tag{3.34}$$

with $c_j = 1$, $c_k = 1$ and $c_0 = c_{j_{\max}} = 2$. Further, by applying the relation

$$\boldsymbol{G}_{\mathbf{Cheb}(jk)} = \boldsymbol{E}_{\mathbf{Cheb}(jm)}\boldsymbol{E}_{\mathbf{Cheb}(mk)}, \tag{3.35}$$

the discretization stencils of the second derivatives can be determined. [55] As both schemes, the fourth–order finite–difference scheme and the Chebyshev spectral collocation method, are written in matrix form in COSTAS, only the calculation of the discretization stencils has to be modified to change the scheme.

To perform the discretization in the streamwise direction for the LPSE, a first–order backward finite–difference scheme as

$$\frac{\partial \tilde{\boldsymbol{q}}_{(i,j,l)}}{\partial x^1} = \frac{-\tilde{\boldsymbol{q}}_{(i-1,j,l)} + \tilde{\boldsymbol{q}}_{(i,j,l)}}{\Delta x^1} \tag{3.36}$$

is applied for the first point downstream of the initial location of the calculation. For the points further downstream, the scheme is modified to a second–order backward finite–difference scheme which reads

$$\frac{\partial \tilde{\boldsymbol{q}}_{(i,j,l)}}{\partial x^1} = \frac{\tilde{\boldsymbol{q}}_{(i-2,j,l)} - 4\tilde{\boldsymbol{q}}_{(i-1,j,l)} + 3\tilde{\boldsymbol{q}}_{(i,j,l)}}{2\Delta x^1}, \tag{3.37}$$

where also in the streamwise direction the equidistant grid is generated with $\Delta x^1 = 1$ in this work. [92]

3.3.2 Solution Methods for the LST and LPSE

Different schemes are applied to solve the LST or the LPSE. In the LST, two approaches are available in COSTAS to solve Eq. (3.14) with the locally parallel flow

assumption. The first approach is to solve a quadratic eigenvalue problem that is generated by rearranging Eq. (3.14) to

$$(\alpha^2 \frac{1}{g_{11}} \boldsymbol{H_{\alpha\alpha}} + \alpha \frac{1}{\sqrt{g_{11}}} \boldsymbol{H_{\alpha}} + \boldsymbol{H}) \tilde{\boldsymbol{q}} = 0, \tag{3.38}$$

where $\boldsymbol{H_{\alpha\alpha}}$ contains all terms with α^2, $\boldsymbol{H_{\alpha}}$ all terms with α and $\boldsymbol{H}$ the remaining terms [20]. To solve the system of equations Eq. (3.38), the quadratic eigenvalue problem is linearized which results in

$$\begin{bmatrix} \boldsymbol{H} + \boldsymbol{H_{x^2}} \frac{\partial}{\partial x^2} + \boldsymbol{H_{x^2x^2}} \frac{\partial^2}{\partial {x^2}^2} & 0 \\ 0 & \frac{1}{\sqrt{g_{11}}} \boldsymbol{I} \end{bmatrix} \begin{bmatrix} \tilde{\boldsymbol{q}} \\ \alpha \tilde{\boldsymbol{q}} \end{bmatrix} \tag{3.39}$$

$$= \alpha \frac{1}{\sqrt{g_{11}}} \begin{bmatrix} -\boldsymbol{H_{\alpha}} - \boldsymbol{H_{\alpha x^2}} \frac{\partial}{\partial x^2} & -\frac{1}{\sqrt{g_{11}}} \boldsymbol{H_{\alpha\alpha}} \\ \boldsymbol{I} & 0 \end{bmatrix} \begin{bmatrix} \tilde{\boldsymbol{q}} \\ \alpha \tilde{\boldsymbol{q}} \end{bmatrix} \tag{3.40}$$

with $\boldsymbol{I}$ being the identity matrix and the matrices with the subscript x^2 contain the terms with the first derivatives in the wall normal direction and with x^2x^2 the second derivatives [94]. This generalized complex eigenvalue problem is solved by the QZ–algorithm of LAPACK [1].

In the second approach, a Newton iteration is applied to solve the governing equations. To perform this calculation, firstly, an initial guess is required for the streamwise wave–number α. Therefore, the most amplified eigenvalue in the eigenvalue spectrum of the previously outlined generalized complex eigenvalue problem is chosen. With this initial guess, the higher–order Newton iteration of [55] with

$$\alpha_{\text{new}} = \alpha_{\text{old}} - \tilde{v}^1_{(i,0,l)} \Big/ \left(\frac{\partial \tilde{v}^1_{(i,0,l)}}{\partial \alpha} \right) - \tilde{v}^{1^2}_{(i,0,l)} \left(\frac{\partial^2 \tilde{v}^1_{(i,0,l)}}{\partial \alpha^2} \right) / 2 \left(\frac{\partial \tilde{v}^1_{(i,0,l)}}{\partial \alpha} \right)^3 \tag{3.41}$$

is performed until the solution converges, where the convergence criterion is given in Sec. 3.3.3.

In the computation of the LPSE, Eq. (3.14) is solved without simplifications. An initial solution is required due to the discretization in the x^1–direction which is determined by the LST by applying the Newton iteration at an initial location upstream of the neutral point ($\sigma = 0$) of the investigated disturbance. Thereafter, the LPSE are solved moving downstream along the surface. Due to the x^1–dependency of the governing equations, an additional condition to close the system of equations is required. Several approaches can be found in the literature, where in this work the normalization condition based on the disturbance kinetic energy E is applied as

$$\alpha_{\text{new}} = \alpha_{\text{old}} - i \frac{1}{E} \int_{x^2=0}^{x^2_{\max}} \frac{\bar{\rho}}{\sqrt{g_{11}}} \left(\tilde{v}^{1^\dagger} \frac{\partial \tilde{v}^1}{\partial x^1} + \tilde{v}^{2^\dagger} \frac{\partial \tilde{v}^2}{\partial x^1} + \tilde{v}^{3^\dagger} \frac{\partial \tilde{v}^3}{\partial x^1} \right) dx^2, \tag{3.42}$$

with $E = \int_{x^2=0}^{x^2_{\max}} \bar{\rho}(|\tilde{v}^1|^2 + |\tilde{v}^2|^2 + |\tilde{v}^3|^2) dx^2$ [35].

3.3.3 Boundary Conditions

The system of equations Eq. (3.14), requires adequate boundary conditions at the wall ($x^2 = 0$) and at the outer boundary ($x^2_{\max}$). At the wall, the no–slip boundary condition and a condition for the disturbance temperature are applied. Due to the several times larger disturbance frequencies compared to the thermal response time of the wall, the disturbance wall temperature remains zero [42]. Thus, the boundary conditions at the wall read

$$\tilde{v}^1 = \tilde{v}^2 = \tilde{v}^3 = \tilde{T} = 0, \quad \text{at } x^2 = 0. \tag{3.43}$$

If applying the Newton–iteration of Sec. 3.3.2 in the LST, the boundary conditions have to be modified. To avoid the trivial solution of a zero disturbance eigenfunction, the wall boundary condition for the streamwise velocity component is replaced by $\tilde{\rho} = 1$. Thus, the system of equations is solved until $\tilde{v}^1 < \Delta$ with $\Delta = 1 \times 10^{-8}$ as the convergence criterion mentioned in Sec. 3.3.2.

At the outer boundary of the computational domain ($x^2_{\max}$) inside the shock layer, respectively, on the high pressure side of the bow shock, three types of boundary

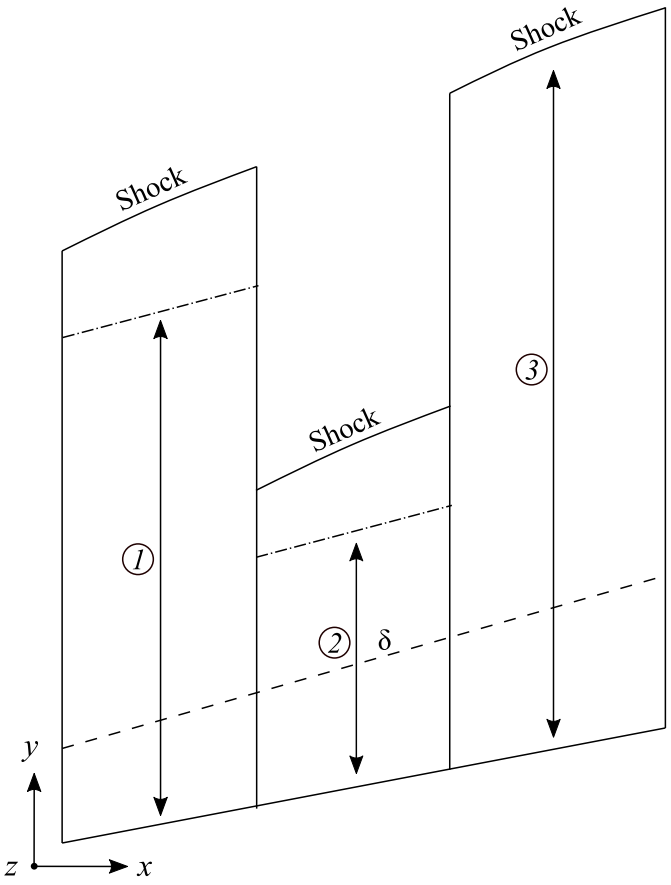

Figure 3.1: Computational domains in the boundary–layer stability solver to prescribe the boundary conditions at the outer boundary.

conditions can be prescribed. The first one requires the disturbances to vanish completely. This requirement can be found sufficiently far away from the wall (① in Fig. 3.1), usually several times the boundary–layer thickness δ. Thus, at this location all disturbance quantities are set to zero as [12]

$$\tilde{\rho} = \tilde{v}^1 = \tilde{v}^2 = \tilde{v}^3 = \tilde{T} = 0, \quad \text{at } x^2_{\max}. \tag{3.44}$$

If, due to a small bow shock distance, the outer boundary lies closer to the wall, a non–reflecting boundary condition has to be applied because the disturbances do not vanish completely and oscillations would occur in the disturbance eigenfunctions [79] (② in Fig. 3.1). By applying a characteristic decomposition to the governing equations and using the outgoing characteristics, this second boundary condition, found in [8, 41], results in a system of equations at the outer boundary as

$$\bar{\boldsymbol{T}}_{\boldsymbol{t}} \frac{\partial \boldsymbol{q'}}{\partial t} + \bar{\boldsymbol{A}}_{\boldsymbol{x^1}} \frac{\partial \boldsymbol{q'}}{\partial x^1} + \bar{\boldsymbol{B}}^{+}_{\boldsymbol{x^2}} \frac{\partial \boldsymbol{q'}}{\partial x^2} + \bar{\boldsymbol{C}}_{\boldsymbol{x^3}} \frac{\partial \boldsymbol{q'}}{\partial x^3} + \bar{\boldsymbol{D}}_{\boldsymbol{0}} \boldsymbol{q'} = 0, \tag{3.45}$$

where the matrix $\bar{\boldsymbol{B}}^{+}_{\boldsymbol{x^2}}$ is calculated by the maximum positive eigenvalue $\boldsymbol{\Lambda}^{+} = \mathrm{diag}(\max(0,\lambda_k))$ of $\bar{\boldsymbol{T}}_{\boldsymbol{0}}^{-1} \bar{\boldsymbol{B}}_{\boldsymbol{x^2}}$ and the left eigenvetor $\boldsymbol{L}_{\boldsymbol{\Lambda}}$ as

$$\bar{\boldsymbol{B}}^{+}_{\boldsymbol{x^2}} = \bar{\boldsymbol{T}}_{\boldsymbol{0}} (\boldsymbol{L}_{\boldsymbol{\Lambda}} \boldsymbol{\Lambda}^{+} \boldsymbol{L}^{-1}_{\boldsymbol{\Lambda}}). \tag{3.46}$$

For the determination of this boundary condition, the inviscid disturbance equations are used because at the outer boundary, outside the boundary–layer, the viscous effects can be neglected. [8, 41]

The third boundary condition, implemented in COSTAS, considers the bow shock as the outer boundary (③ in Fig. 3.1). In this case, the unsteady Rankine–Hugoniot shock relations are solved at the first grid point next to the shock on the high pressure side. Following the derivation in [11, 69], the unsteady Rankine–Hugoniot relations in the disturbance form read

$$(i\alpha(\bar{\boldsymbol{E}}_{\infty} - \bar{\boldsymbol{E}}) + i\beta(\bar{\boldsymbol{F}}_{\infty} - \bar{\boldsymbol{F}}) - i\omega(\bar{\boldsymbol{Q}}_{\infty} - \bar{\boldsymbol{Q}}))\tilde{n}_S + \frac{\partial \bar{n}_S}{\partial x^1} \tilde{\boldsymbol{E}} - \tilde{\boldsymbol{G}}, \tag{3.47}$$

where $\boldsymbol{E}$, $\boldsymbol{F}$, $\boldsymbol{G}$ are the inviscid fluxes in general curvilinear coordinates in tensor notation to account for the coordinate system in the current work and n_S is the normal shock distance. Further, the vectors with the subscript "∞" are the fluxes and the state vector in the free–stream, whereas the vectors without a subscript denote the fluxes and the state vector at the first grid point next to the shock on the high pressure side. [11, 69] The additional variable to be solved for is the shock distance $\tilde{n}_S$ that arises due to the disturbance formulation $n_S = \bar{n}_S + \tilde{n}_S$. Due to this additional unknown variable, an additional boundary condition is required to solve Eq. 3.47. Therefore, because currently only 2D–axisymmetric disturbances are considered in COSTAS, the spanwise disturbance velocity is set to zero at the shock, respectively, $\tilde{v}^3 = 0$.

3.3.4 Step Size Restriction

As the parabolized stability equations are only nearly parabolic in space because only the second derivatives in the streamwise direction are neglected, an upstream propagation of the information is still present [24]. Thus, similar to the parabolized Navier–Stokes equations, a limitation of the step size in the streamwise direction exists to achieve a convergence of the solution [3]. Applying the parabolized stability equations, this step size limitation in the streamwise direction was found to be

$$\Delta s > \frac{1}{|\mathrm{Real}(\alpha)|} \tag{3.48}$$

by Li & Malik [47, 48]. Therefore, to overcome this limitation, respectively, to enable a smaller step size, the disturbance pressure gradient term is manipulated. This manipulation is performed in the streamwise derivative of the disturbance pressure as

$$\frac{\partial p'}{\partial x^1} = \left(i\alpha\tilde{p} + f_p \frac{\partial \tilde{p}}{\partial x^1} \right) e^{i(\Phi(x^1, x^3, t))} \tag{3.49}$$

with

$$f_p = \frac{\gamma \mathrm{M}^2_{x^1}}{1 + (\gamma - 1)\mathrm{M}^2_{x^1}}, \qquad \text{for } M_{x^1} < 1, \tag{3.50}$$

$$f_p = 1, \qquad \text{for } M_{x^1} \geq 1, \tag{3.51}$$

where M_{x^1} is the streamwise Mach number [10, 24].

In case of calculations in thermo-chemical equilibrium, γ in Eq. (3.50) is replaced by the specific heat capacity ratio of the actual gas composition in thermo–chemical equilibrium γ_{eq}. Further, due to the representation of the governing equations in terms of the density, Eq. (3.49) has to be rewritten with Eq. (3.19) or Eq. (3.22) depending on the thermodynamic model to apply the manipulation in Eq. (3.49) to the density and the temperature.

3.3.5 Computational Grid and Interpolation

To perform the boundary–layer stability calculations, a grid aligned with the boundary–layer edge $x_{n,\delta}$ is required, where, at this location, the disturbance amplitudes exponentially decay [42, 55]. To generate this grid, firstly, the boundary–layer thickness has to be determined. Therefore, the value of the total enthalpy is used in COSTAS as the criterion. Two approaches are applied depending on whether an adiabatic or an isothermal wall was set in the laminar base–flow calculation. For an adiabatic wall, the grid point with the maximum total enthaply along each surface normal grid line characterizes the outer edge of the boundary–layer [32], whereas in case of an isothermal wall, the grid point with 99% of the free–stream total enthaply corresponds to the boundary–layer edge. As a distinct grid point is found with this procedure but the real boundary–layer edge location can be located between two grid

points, thereafter, the interpolation and smoothing procedure of the mesh adaption in Sec. 2.3.4 is performed to determine this location. In a last step, to prescribe the boundary conditions, explained in Sec. 3.3.3, the outer boundary of the calculation domain $x_{n,\max}$ is placed at several times the determined boundary–layer thickness but with the restriction to not exceed the shock layer thickness. Besides the alignment of the grid with the boundary–layer edge, for the shock boundary condition in Sec. 3.3.3, the shock location determined in Sec. 2.3.4 is used as the outer boundary of the computational domain.

For the generation of the new grid point distribution in the wall normal direction, two approaches presented by Malik [55] can be used. For the discretization with finite–differences of fourth order, the wall clustered grid given by

$$x_n = \frac{ax^2/x_{\max}^2}{b - x^2/x_{\max}^2} \tag{3.52}$$

is used, where $a = (x_{n,\max}x_{n,\delta})/(x_{n,\max} - 2x_{n,\delta})$ and $b = 1 + a/x_{n,\max}$. For the discretization with the Chebyshev spectral collocation method

$$x_n = a\frac{1 + x^2}{b - x^2} \tag{3.53}$$

is applied with $a = (x_{n,\max}x_{n,\delta})/(x_{n,\max} - 2x_{n,\delta})$ and $b = 1 + 2a/x_{n,\max}$ and with the collocation points calculated by Eq. (3.33). In both cases x^2 runs from zero to the maximum grid point number.

The new mesh requires an accurate interpolation of the flow variables from the base–flow solution mesh onto the stability grid. Two approaches were tested in this work to perform this interpolation. One approach is the interpolation of the flow variables onto the new mesh and the calculation of the spatial derivatives on the stability grid. The other approach is the simultaneous interpolation of the flow variables and their spatial derivatives onto the new mesh similar to Johnson & Candler [34]. By applying the first approach, it was found that the first and second derivatives in the wall normal direction show oscillations if a very fine stability grid was used. In contrast, by applying the second approach, the spatial derivatives remain smooth even on very fine grids. To apply the second approach, firstly, the derivatives of the flow variables in the Cartesian reference frame with respect to the physical normal direction, e.g.,

$$\frac{\partial u}{\partial x_n}, \quad \frac{\partial^2 u}{\partial x_n^2}, \quad \frac{\partial T}{\partial x_n} \tag{3.54}$$

are calculated by a fourth–order finite–difference scheme irrespective of the applied discretization scheme. This is the case because the calculation is performed in the physical coordinate system, respectively, no calculation on the Chebyshev collocation points is possible. Further, the calculation is performed with respect to the Cartesian coordinates and velocities due to the different metric terms for the transformation into the curvilinear coordinate system before and after the interpolation. Thus, the interpolation can not be performed with the curvilinear velocities due to incompatible

transformations. In a second step, the flow variables and their spatial derivatives need to be interpolated adequately onto the new mesh of Eq. (3.52) or Eq. (3.53) for which a Lagrange polynomial of fourth order is used. In a last step, the new flow variables and the spatial derivatives are transformed into the general curvilinear coordinate system. Therefore, the transformations of the first and second derivatives with respect to x_n into the derivatives with respect to the computational curvilinear normal coordinate are performed by, e.g.,

$$\frac{\partial u}{\partial x^2} = \frac{\partial u}{\partial x_n}\frac{\partial x_n}{\partial x^2}, \quad \frac{\partial^2 u}{\partial x^{2^2}} = \frac{\partial^2 u}{\partial x_n^2}\left(\frac{\partial x_n}{\partial x^2}\right)^2 + \frac{\partial u}{\partial x_n}\frac{\partial^2 x_n}{\partial x^{2^2}}. \tag{3.55}$$

Further, the transformations of the Cartesian velocities and their derivatives into the curvilinear velocities are defined by, e.g.,

$$v^1 = u\frac{\partial x^1}{\partial x} + v\frac{\partial x^1}{\partial y} + w\frac{\partial x^1}{\partial z}, \tag{3.56}$$

$$\begin{aligned}\frac{\partial v^1}{\partial x^2} = {} & \frac{\partial u}{\partial x^2}\frac{\partial x^1}{\partial x} + u\frac{\partial(\partial x^1/\partial x)}{\partial x^2} + \frac{\partial v}{\partial x^2}\frac{\partial x^1}{\partial y} + v\frac{\partial(\partial x^1/\partial y)}{\partial x^2} \\ & + \frac{\partial w}{\partial x^2}\frac{\partial x^1}{\partial z} + w\frac{\partial(\partial x^1/\partial z)}{\partial x^2},\end{aligned} \tag{3.57}$$

$$\begin{aligned}\frac{\partial^2 v^1}{\partial x^{2^2}} = {} & \frac{\partial^2 u}{\partial x^{2^2}}\frac{\partial x^1}{\partial x} + 2\frac{\partial u}{\partial x^2}\frac{(\partial x^1/\partial x)}{\partial x^2} + u\frac{\partial^2(\partial x^1/\partial x)}{\partial x^{2^2}} \\ & + \frac{\partial^2 v}{\partial x^{2^2}}\frac{\partial x^1}{\partial y} + 2\frac{\partial v}{\partial x^2}\frac{(\partial x^1/\partial y)}{\partial x^2} + v\frac{\partial^2(\partial x^1/\partial y)}{\partial x^{2^2}} \\ & + \frac{\partial^2 w}{\partial x^{2^2}}\frac{\partial x^1}{\partial z} + 2\frac{\partial w}{\partial x^2}\frac{(\partial x^1/\partial z)}{\partial x^2} + w\frac{\partial^2(\partial x^1/\partial z)}{\partial x^{2^2}}.\end{aligned} \tag{3.58}$$

Similar transformation relations are applied to the other velocity components. For the calculation of the base–flow derivatives in the streamwise and the spanwise direction as well as for the mixed derivatives, the fourth–order finite–difference scheme is applied in the curvilinear reference frame because a finite–difference scheme is used in this direction for the discretization. Further, no interpolation of the flow variables is performed because the grid remains the same in these directions between the two solvers.

3.4 Growth Rate and N-Factor

The criterion for the laminar–turbulent transition in the LST and LPSE is the N–factor. To calculate this quantity, the growth rate is required which is calculated in different ways for the LST and the LPSE. In the LST, the growth rate is the negative imaginary part of the wave–number $\sigma = -\mathrm{Imag}(\alpha)$ [105]. In contrast, the growth rate for the LPSE is calculated by

$$\sigma = -\mathrm{Imag}(\alpha) + \frac{1}{2E}\frac{\partial E}{\partial x^1} \tag{3.59}$$

with the disturbance kinetic energy defined in Sec. 3.3.2 [35]. By integrating the growth rate along the surface of the geometry as

$$N(x^1) = \ln\frac{A}{A_0} = \int_{x^1=0}^{x^1_{\max}} \sqrt{g_{11}}\sigma dx^1 \tag{3.60}$$

the N–factor distribution is determined [35], where $x^1 = 0$ is the surface location of the neutral point $\sigma = 0$ and $x^1_{\max}$ the end of the geometry.

Chapter 4

Validation of the Solvers

4.1 Stetson Mach 8 Cone

4.1.1 Laminar Base–Flow Results

To validate the Navier–Stokes solver (CONSST3D) and the boundary–layer stability solver (COSTAS) for the perfect gas regime, the Stetson Mach 8 cone [85] was chosen because of the several results by other researchers that can be found in the literature. The results which were published in [92] will be presented in the following containing additional results which were not presented in [92]. Firstly, the laminar base–flow calculations were performed with the following test case parameters. The geometry consists of a blunted cone with a nose radius of $R_N^* = 3.81$ mm, a cone half angle of $\Theta = 7^\circ$ and an overall length of $L^* = 1.016$ m [85]. The free–stream parameters, including the Reynolds number with respect to the nose radius R_N^*, can be found in Tab. 4.1 [105]. Due to the moderate stagnation point temperature of $\bar{T}^* = 750$ K [105], the perfect gas model of Sec. 2.2.1 with the respective constants for air was applied. Further, due to the high Reynolds number, the thin–layer Navier–Stokes equations were solved and an adiabatic wall temperature condition was set similar to [105]. A 2D–axisymmetric calculation was performed with a grid distribution of 300 points in the streamwise direction. In the wall normal direction 300/350/400 grid points were prescribed to perform a mesh independence study with a clustering of the grid points at the wall and at the shock as explained in Sec. 2.3.6.

Firstly, the contour plots of the Mach number and the temperature at the nose part of the investigated geometry are shown in Fig. 4.1. The contour plot of the Mach number illustrates the mesh adaption of Sec. 2.3.4. Firstly, an alignment of the grid with the bow shock can be recognized and secondly the free–stream ($\bar{\mathrm{M}} = 7.99$)

Table 4.1: Free-stream parameters for the Stetson Mach 8 cone [105].

M_∞	Re_∞	p_∞^* [Pa]	T_∞^* [K]
7.99	33630	413.685	54.348

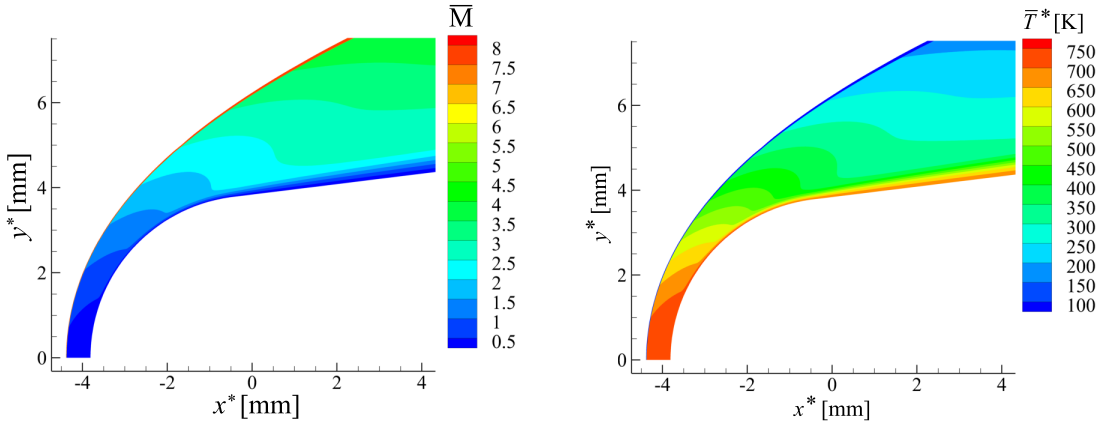

(a) Mach number (b) Temperature

Figure 4.1: Contour plots at the nose part of the Stetson Mach 8 cone.

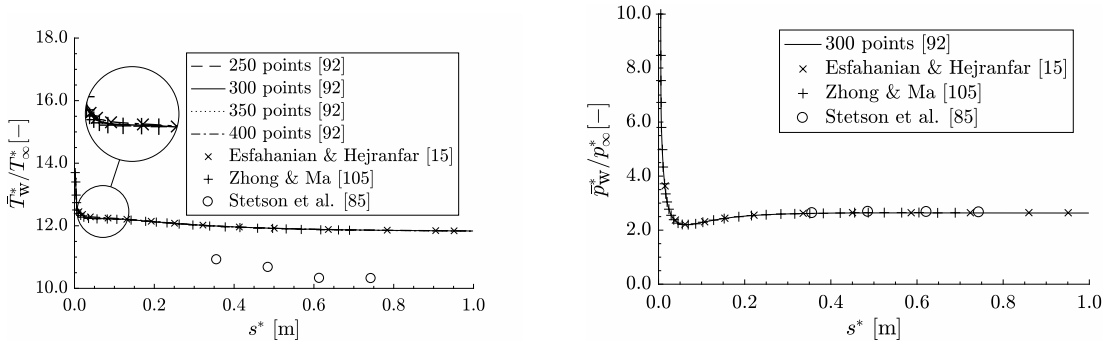

(a) Wall temperature (b) Wall pressure

Figure 4.2: Wall distributions along the arclength of the Stetson Mach 8 cone [92].

containing 20 grid points explained in Sec. 2.3.6 can be observed. The contour plot of the temperature shows that the maximum temperatures, that appear at the stagnation point, are below the perfect gas limit of $\bar{T}^* = 800$ K given in Sec. 2.2.2 and, thus, justifies the application of the perfect gas model for this test case.

In Fig. 4.2, the non–dimensional wall temperature and wall pressure are presented along the cone arclength. Besides a validation against the numerical results of Esfahanian & Hejranfar [15], the results of Zhong & Ma [105] and the experimental data of Stetson et al. [85], a mesh independence study was performed with regard to the temperature. Firstly, the current temperature distributions of the different grid point distributions in Fig. 4.2a show only slight differences at the junction between the nose and the cone part which can be seen in the zoomed portion in the figure. Downstream of this location, the temperature shows similar distributions independent of the number of grid points. Due to these similar distributions, the result containing 300 grid points in the wall normal direction was chosen as the base–flow solution for the boundary–layer stability calculations and for the further validation

in this section. Comparing the current temperature distributions with the other numerical results a good agreement can be observed along the entire cone. The experimental results of Stetson et al. in contrast show lower values at the measurement locations. As the same observations were made by the other researchers applying an adiabatic wall boundary condition, Zhong & Ma suggested that the adiabatic

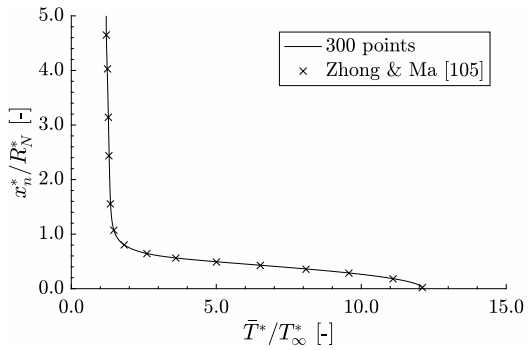

(a) Wall normal temperature distribution

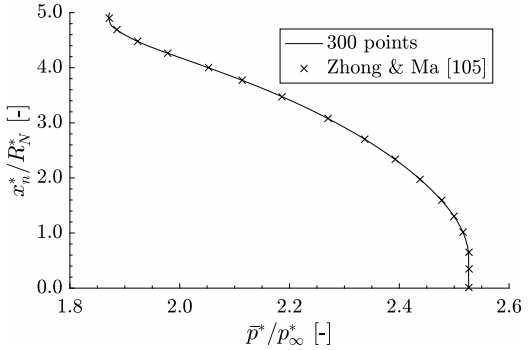

(b) Wall normal pressure distribution

Figure 4.3: Wall normal distributions at $s = 54$ of the Stetson Mach 8 cone.

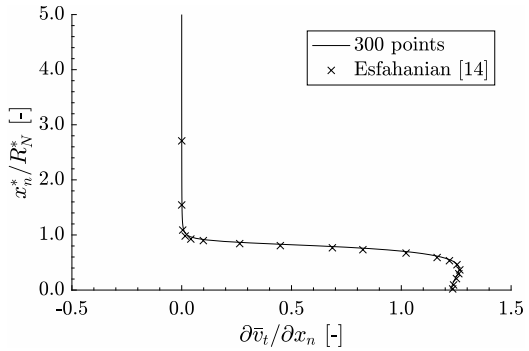

(a) Wall normal derivative of the physical streamwise velocity

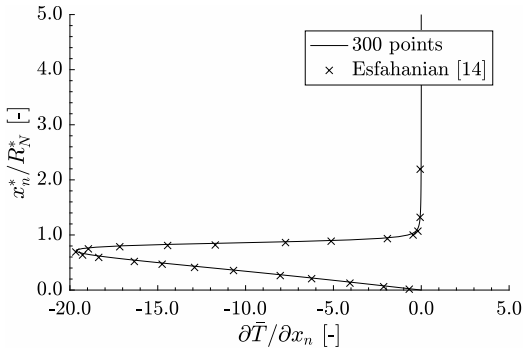

(b) Wall normal derivative of the temperature

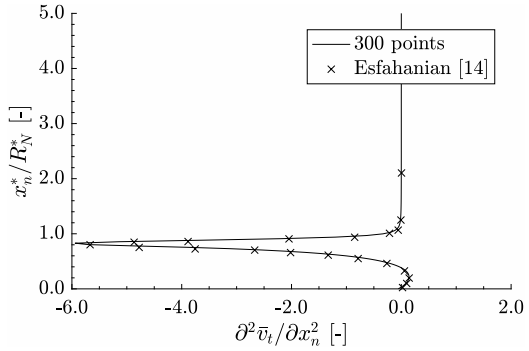

(c) Wall normal second derivative of the physical streamwise velocity

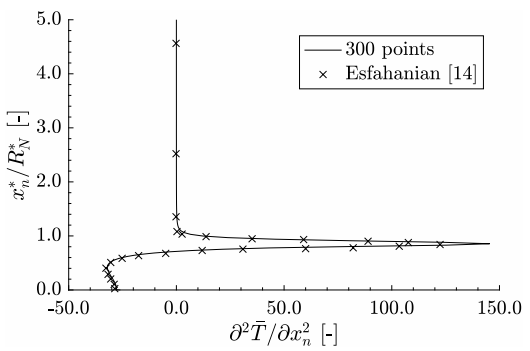

(d) Wall normal second derivative of the temperature

Figure 4.4: Wall normal distributions at $s = 175$ of the Stetson Mach 8 cone.

boundary condition does not reflect the real experimental conditions [105]. Lastly, the pressure distributions are compared with each other in Fig. 4.2b. In this case, the current results agree well with the referenced numerical results as well as with the experimental results.

In the calculation of the boundary layer stability, an adequate base–flow solution is required. Therefore, to examine accuracy of the current base–flow solution, selected wall normal profiles of the flow variables and their spatial derivatives will be presented in the following. In Fig. 4.3, the non–dimensional wall normal temperature and pressure distributions at $s = 54$ are presented and compared to the distributions of Zhong & Ma [105] along the non-dimensional wall normal distance. In both cases, a good agreement can be observed between the distributions along the whole wall normal distance, respectively, inside the boundary–layer and in the inviscid region. The first and second spatial derivatives of the non–dimensional physical streamwise velocity component and the temperature with respect to the non–dimensional wall normal distance are compared to the profiles of Esfahanian [14] in Fig. 4.4 at a surface location of $s = 175$. Similar to the other base–flow validation results, a good agreement between the current results and the results of Esfahanian [14] can be observed.

4.1.2 Boundary–Layer Stability Results

The base–flow results, presented in Sec. 4.1.1, were used for the validation with regard to the boundary–layer stability, where the linear stability theory and the linear parabolized stability equations were applied for the calculations. In both cases, the Chebyshev spectral collocation method in combination with the non–reflecting boundary condition at the outer boundary was applied. Firstly, the linear stability theory was validated against the other numerical and experimental results from the previous section at the surface location of $s = 175$. For this purpose, the growth rate and the phase speed for multiple disturbance frequencies from the LST are presented, where the growth rate is shown for different number of grid points to perform the

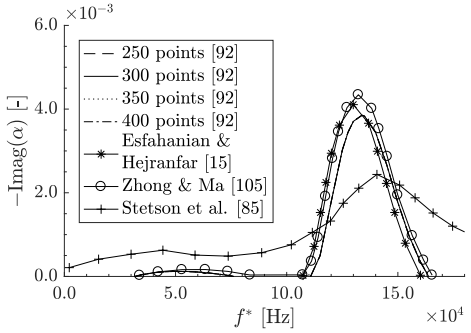

(a) Growth rate versus disturbance frequency [92]

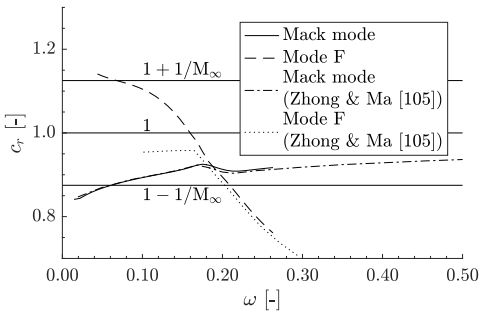

(b) Phase speed versus angular disturbance frequency

Figure 4.5: LST results at $s = 175$ of the Stetson Mach 8 cone.

mesh independence study for the stability calculations as well. For this purpose, 250/300/350/400 grid points were prescribed in the wall normal direction.

The current growth rate distributions versus the frequency show equal results in Fig. 4.5a for the different number of grid points. Thus a number of 300 grid points was chosen for the further investigations. Comparable to the other numerical

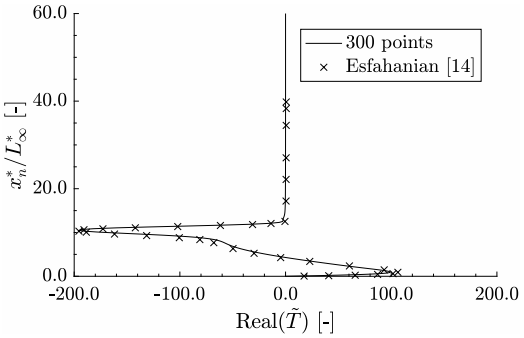

(a) Real part of disturbance temperature eigenfunction

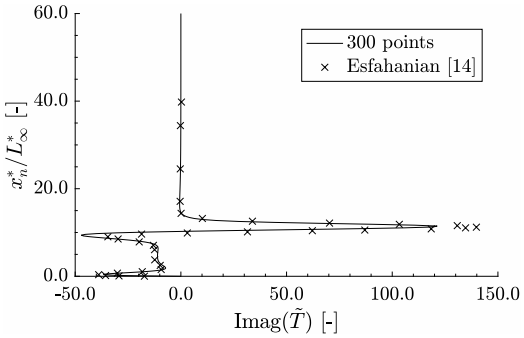

(b) Imaginary part of disturbance temperature eigenfunction

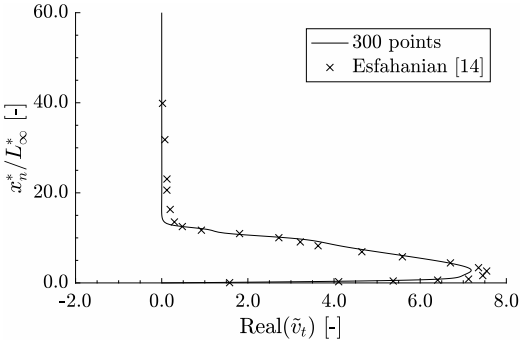

(c) Real part of physical streamwise contravariant disturbance velocity eigenfunction

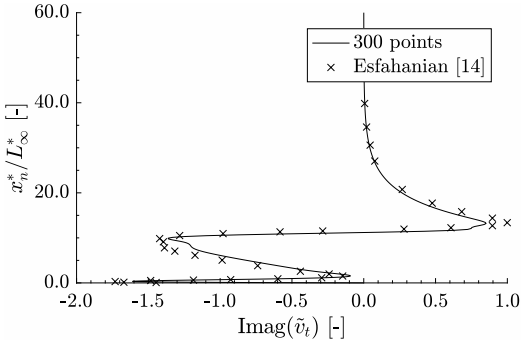

(d) Imaginary part of physical streamwise contravariant disturbance velocity eigenfunction

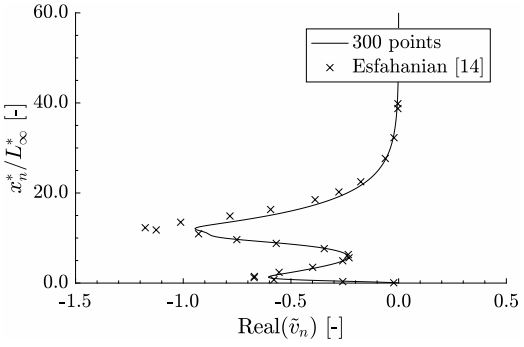

(e) Real part of physical normal contravariant disturbance velocity eigenfunction

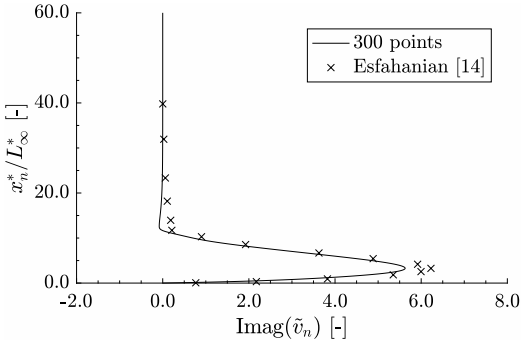

(f) Imaginary part of physical normal contravariant disturbance velocity eigenfunction

Figure 4.6: Disturbance eigenfunctions at $s = 175$ of the Stetson Mach 8 cone.

results, a first and a second Mack mode can be recognized in the current growth rate distributions. The unstable first mode shows only small growth rates at low frequencies from $f^* = 35$ kHz to $f^* = 75$ kHz comparable to the results of Zhong & Ma [105]. Further, the second Mack mode becomes unstable at frequencies from $f^* = 115$ kHz to $f^* = 160$ kHz, where comparable values can be found in [15] and [105]. In contrast to the other results, the maximum of the current growth rate shows a slightly lower value of $-\text{Imag}(\alpha) = 3.8515 \times 10^{-3}$ at a slightly higher disturbance frequency of $f^* = 133.87$ kHz. With respect to the experimental results of Stetson et al. [85], the current growth rate is over–predicted and the maximum occurs at a lower disturbance frequency. This trend can also be observed in the other numerical results.

In Fig. 4.5b, the current phase speed is compared to the one of Zhong & Ma [105]. The Mack mode shows a similar distribution along the angular disturbance frequency and the intersection point of the Mack mode and the Mode F, where the first mode converts to a second mode, can be found at $\omega = 0.1879$, respectively, slightly higher compared to $\omega = 0.1825$ in [105].

Additionally, a comparison of the disturbance eigenfunctions corresponding to a disturbance frequency of $f^* = 127.562$ kHz with the results of Esfahanian [14] is performed. Therefore, the real and imaginary parts of the temperature eigenfunction and the physical streamwise and normal contravariant velocity eigenfunctions are presented along the non-dimensional wall normal distance in Fig. 4.6. Note that the eigenfunctions are scaled with respect to the maximum of the real part of the temperature eigenfunction of [14]. Comparing the resulting eigenfunctions, overall a good agreement can be observed for all variables, respectively, the distribution along the wall normal distance and the location of the maxima, with only small differences especially in the physical normal contravariant disturbance velocity eigenfunction. The slight differences between the eigenfunctions can be caused by the smaller number of grid points of 100 and 200 points in the wall normal direction and the Rankine-Hugoniot shock boundary condition applied for the computation in [14] compared to

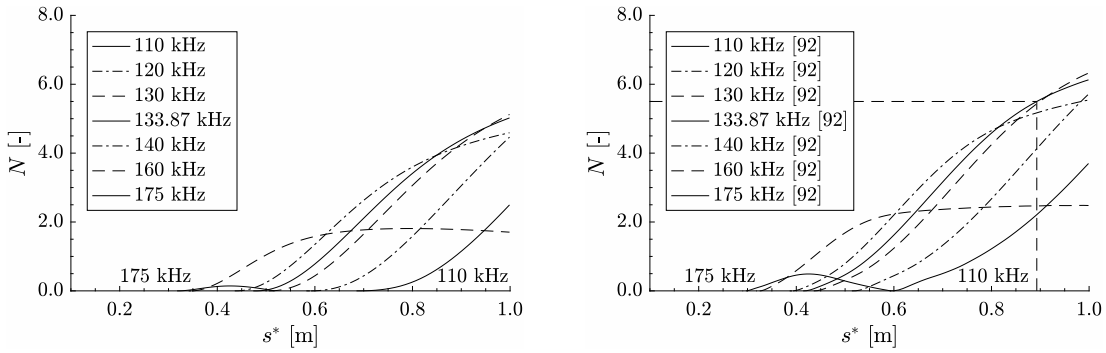

(a) N–factor distributions of the LST along the arclength

(b) N–factor distributions of the LPSE along the arclength [92]

Figure 4.7: N–factor distributions of the Stetson Mach 8 cone.

300 grid points and a non–reflecting boundary condition for the current computation. Additionally, the numerical schemes which are implemented in COSTAS could have a higher numerical dissipation compared to the schemes in [14].

Lastly, the N–factor distributions of the LST and LPSE along the cone arclength are presented in Fig. 4.7 for multiple disturbance frequencies. Comparing the N–factor distributions of the LST in Fig. 4.7a with the current N–factor distributions of the LPSE in Fig. 4.7b, the results of the LST show smaller N–factors along the cone and the neutral points $\sigma = -\text{Imag}(\alpha) = 0$ appear slightly further downstream. The current results of the LPSE are compared to the results of Esfahanian & Hejranfar [15] and Malik et al. [57] by applying the same N–factor of $N = 5.5$ as the criterion for the transition onset location. Thus, the transition onset location was found for a disturbance frequency of $f^* = 133.87$ kHz at $s^*_{\text{trans}} = 0.8928$ m. This surface location corresponds to a transition Reynolds number of $\text{Re}_{\text{trans},\infty,s} = \sqrt{(\text{Re}_{\infty,R_N} s^*_{\text{trans}})/R^*_N} = 2807$. Compared to the values of $\text{Re}_{\text{trans},\infty,s} = 2865/2825$ found by Esfahanian & Hejranfar [15] and $\text{Re}_{\text{trans},\infty,s} = 2800$ by Malik et al. [57], a good agreement was found in the current results. Additionally, a good agreement can be observed in the transition arclength compared to $s^*_{\text{trans}} = 0.9$ m found by Rosenboom et al. [76]. With respect to the presented base–flow results and the results of the LST and the LPSE, the base–flow solver and the boundary layer–stability solver are successfully validated for the perfect gas regime.

4.2 Mach 10 Flat Plate

4.2.1 Laminar Base–Flow Results

A second test case was chosen to validate the capability of the solvers to accurately calculate the base–flow and the boundary–layer stability in the thermo–chemical equilibrium gas regime, where the results, published in [92], will be presented in the following, which contain additional results which were not presented in [92]. To perform the validation, a Mach 10 flat plate was chosen, where the free–stream values can be found in Tab. 4.2 [56, 58]. For this test case, the Reynolds number Re_∞ is given with respect to the overall length $L^* = 1$ m chosen in the current calculations. Similar to the Stetson Mach 8 cone, the thin–layer Navier–Stokes equations were solved with an adiabatic wall boundary condition. Further, the thermo–chemical equilibrium gas model of Sec. 2.2.2 for air was applied. The mesh consisted of 300 grid points in the streamwise direction and 300/350/400/450 grid points in the wall normal direction to perform the mesh independence study with a clustering of the

Table 4.2: Free-stream parameters for the Mach 10 flat plate [56, 58].

M_∞	Re_∞	p^*_∞ [Pa]	T^*_∞ [K]
10	6.3922×10^6	3596	350

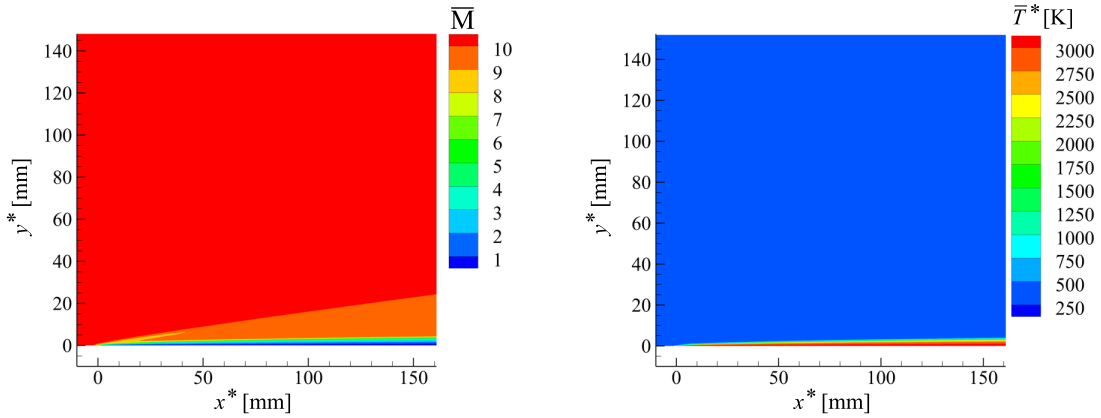

(a) Mach number (b) Temperature

Figure 4.8: Contour plots at the front part of the Mach 10 flat plate.

grid points at the wall.

In Fig. 4.8, contour plots of the Mach number and the temperature are presented. Fig. 4.8a illustrates the issue in the clustering of the grid points around the shock in a structured grid approach for flat plates mentioned in Sec. 2.3.6. As the shock arises at the tip of the flat plate ($x^* = 0$ mm), all grid lines would collapse at this position if aligning the mesh with the shock shape and a calculation of the governing equations would become impossible. Thus, because the grid alignment cannot be performed, a clustering of the grid points around the shock on a structured grid cannot be achieved. In Fig. 4.8b, the observed high temperature of $\bar{T}^* = 3200$ K justifies the application of the thermo–chemical equilibrium gas model because the temperatures exceed the temperature limit of $\bar{T}^* = 800$ K for the application of the perfect gas model.

To perform the mesh independence study and to validate the base–flow solution in the thermo–chemical equilibrium gas regime, the results along the wall and along the wall normal distance at a surface location of $\mathrm{Re}_x = \sqrt{\mathrm{Re}_\infty x} = 2000$ are shown in Fig. 4.9. The non–dimensional temperature distributions along the wall in Fig. 4.9a show oscillatory behaviors at the tip of the flat plate ($\mathrm{Re}_x = 0$). By increasing the number of grid points in the wall normal direction, the oscillations damp but small oscillations remain in the temperature distributions. These oscillations arise due to the attached shock at the tip of the flat plate and, thus, due to the former explained issue in aligning the mesh with the shock. Thus, an adequate grid point distribution at this location is difficult to achieve. Nevertheless, further downstream, the temperature distributions are in good agreement for 350 to 450 points in the wall normal direction.

As the validation of the boundary–layer stability solver is performed at a surface location of $\mathrm{Re}_x = 2000$, the current non–dimensional wall normal temperature and physical streamwise velocity distributions are presented in Fig. 4.9b along the wall normal distance. Firstly, the trend observed along the wall can be recognized in

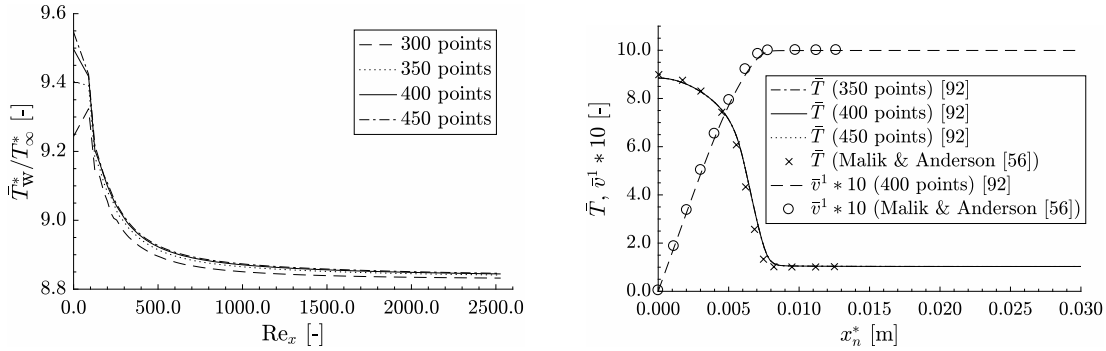

(a) Wall temperature distribution versus the Reynolds number along the flat plate

(b) Temperature and physical streamwise velocity distribution along the wall normal distance at $Re_x = 2000$ [92]

Figure 4.9: Base–flow results of the Mach 10 flat plate.

the wall normal temperature distributions as well, namely, the comparable results for the number of grid points from 350 to 450 points. Thus, the result from the grid containing 400 points in the wall normal direction was used for the further investigations. Comparing the current temperature as well as the physical streamwise velocity profiles with Malik & Anderson [56], similar results can be observed, where only slight differences in the temperature distributions can be found. These small differences are likely due to differences in the thermo–chemical equilibrium gas models and because Malik & Anderson calculated the flow–field using the boundary-layer theory. Nevertheless, due to the overall good agreement between the two results, the validation of the boundary–layer stability solver is performed in the next section with the current result.

4.2.2 Boundary–Layer Stability Results

The validation of the boundary–layer stability solver by applying the thermo–chemical equilibrium gas model was performed by LST calculations at a surface location of $Re_x = 2000$ with a grid containing 300/400/500 wall normal grid points. Also in this case, the Chebyshev spectral collocation method in combination with the non–reflecting boundary condition at the outer boundary was applied.

The growth rate and the phase speed are shown in Fig. 4.10 versus the angular disturbance frequency, where the growth rate is presented for the different number of grid points along the wall normal direction in the LST calculations. The current growth rates in Fig. 4.10a show equal distributions for all numbers of grid points. Thus, the grid with 300 points in the wall normal direction was chosen for the upcoming discussions. Similar to the results of Malik & Anderson [56], a second and a third Mack mode can be observed in the current results with their maxima at the same angular disturbance frequencies. In addition, in the current results, a first mode is detected for the small frequencies which was not observed in the result of Malik & Anderson. The maximum growth rate of the second mode can be found

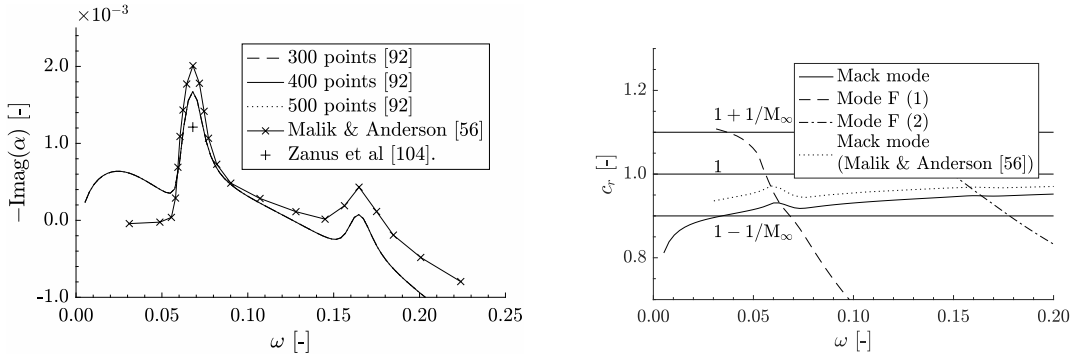

(a) Growth rate versus angular frequency [92]

(b) Phase speed versus angular frequency

Figure 4.10: LST results at $\mathrm{Re}_x = 2000$ of the Mach 10 flat plate.

at $\omega = 6.795 \times 10^{-2}$ with $-\mathrm{Imag}(\alpha) = 1.673 \times 10^{-3}$ and for the third mode at $\omega = 1.646 \times 10^{-1}$ with $-\mathrm{Imag}(\alpha) = 7.569 \times 10^{-5}$ in the current results. Comparing the value of the second mode maximum growth rate with $-\mathrm{Imag}(\alpha) = 2.009 \times 10^{-3}$ of Malik & Anderson, the current solver under–predicts the growth rate but, with respect to $-\mathrm{Imag}(\alpha) = 1.211 \times 10^{-3}$ of Zanus et al. [104], the current solver over–predicts the growth rate. Additionally, the detected third mode in the current results shows a smaller maximum growth rate compared to $-\mathrm{Imag}(\alpha) = 4.307 \times 10^{-4}$ in [56]. Nevertheless, the current growth rate shows a similar distribution and the maximum growth rate of the second mode can be found between the two referenced values.

Lastly, the phase speed along the angular disturbance frequency is compared to the results of Malik & Anderson [56] in Fig. 4.10b. The current values show a qualitatively similar distribution along the whole presented angular frequency range but the values are slightly under–predicted. Additionally, the intersection points of the Mack mode with the fast modes (Mode F) are shown in this figure. The conversion from the first mode to the second mode arises at $\omega = 6.320 \times 10^{-2}$ and the conversion from the second to the third mode arises at $\omega = 1.640 \times 10^{-1}$. The slight differences in the growth rate as well as in the phase speed can be caused by differences in the thermo–chemical equilibrium gas model and in the different methods to calculate the base–flow solution mentioned in Sec. 4.2.1. Overall, the validation shows that the solvers are also capable of accurately calculating the base–flow solution and the boundary–layer stability solution in the thermo–chemical equilibrium gas regime.

Chapter 5

Results

5.1 Shot 2 in CO_2 Atmosphere

5.1.1 Laminar Base–Flow Results

The first test case, to investigate the influence of the atmospheres on the boundary–layer stability in this work, where parts of the results were published in [91], is the blunted cone of Hollis et al. [28] with a nose radius of $R_N^* = 2.5$ mm. Further, the geometry of the cone is defined by a cone half angle of $\Theta = 7^\circ$ and an overall length of $L^* = 1.12$ m. In the high–enthalpy expansion tunnel test runs of Hollis et al., several test conditions were set to examine the influence of the free-stream conditions. In this section, the Shot 2 conditions were chosen due to the measured laminar–turbulent transition with the free-stream conditions presented in Tab. 5.1 [28].

Table 5.1: Free-stream conditions for the blunted cone of Hollis et al. under the Shot 2 conditions [28].

M_∞	Re_∞	p_∞^* [Pa]	T_∞^* [K]	ρ_∞^* [kg/m^3]
9.99	6874	1589	452	0.01861

Similar to the validation test cases in the current work, different number of grid points were set in the wall normal direction to perform a mesh independence study for the base–flow computation. For this purpose, 300 points were chosen in the streamwise direction and 200/300/400 grid points were placed in the wall normal direction, where the grid points were clustered at the wall and around the shock. For the calculations, an axisymmetric laminar flow was assumed and the thin–layer Navier–Stokes equations were solved with an isothermal wall by setting $\bar{T}_w^* = 300$ K. Additionally, the thermo–chemical equilibrium gas model of Sec. 2.2.2 was applied in the calculations because of the high temperatures in the flow–field, containing pure CO_2 similar to the test gas in the experiment. In the following investigations, the axial distance from the virtual sharp nose x_a^* will be used for several figures. Therefore,

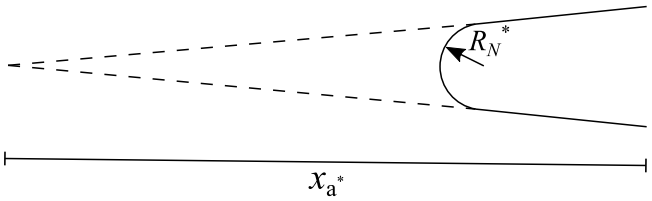

Figure 5.1: Sketch of the axial distance from the virtual sharp nose x_a^*.

note that this distance is the distance if the blunted cone would be prolonged to a sharp cone as shown in Fig. 5.1.

The current results along the before defined distance x_a^* are presented in Fig. 5.2 and are compared with the numerical and experimental results of Hollis et al. [28]. The wall pressure in Fig. 5.2a is presented for the different number of grid points, where no significant difference between the results can be observed. Comparing the wall pressure distributions with the numerical result of Hollis et al., a good agreement is observed. Additionally, comparing the current results with the experimentally measured ones, a good agreement can be found as well at the two points of measurement. In Fig. 5.2b, the wall heat flux along x_a^* is presented. Comparable to the pressure, the current results of the different number of grid points show similar distributions except at the junction between the blunt nose and the straight cone part. Thus, because the wall heat flux show similar distributions downstream of the nose–cone junction and with respect to the wall pressure, the result of the grid containing 400 grid points in the wall normal direction was selected for the further investigations and the boundary–layer stability calculations. In comparison to the experimental result of Hollis et al., the current result under–predicts the wall heat flux for several reasons. Firstly, at a location of $x_a^* = 0.5325$ m, due to the rise in the experimental measured wall heat flux, the laminar–turbulent transition onset location can be found. Thus, the wall heat flux in the experiment shows higher values downstream of this location compared to the current results because a laminar flow was assumed in the base–flow calculation. The same trend can also be observed in the numerical result of

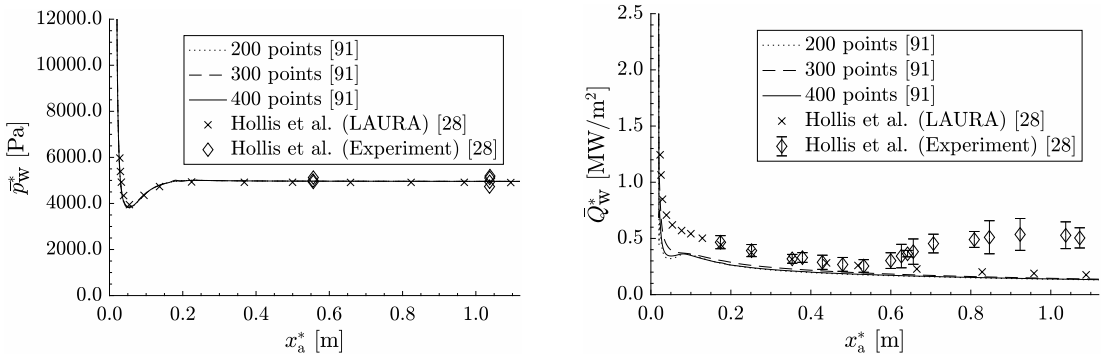

(a) Wall pressure distribution

(b) Wall heat flux distribution

Figure 5.2: Wall distributions along x_a^* of the Shot 2 blunted cone [91].

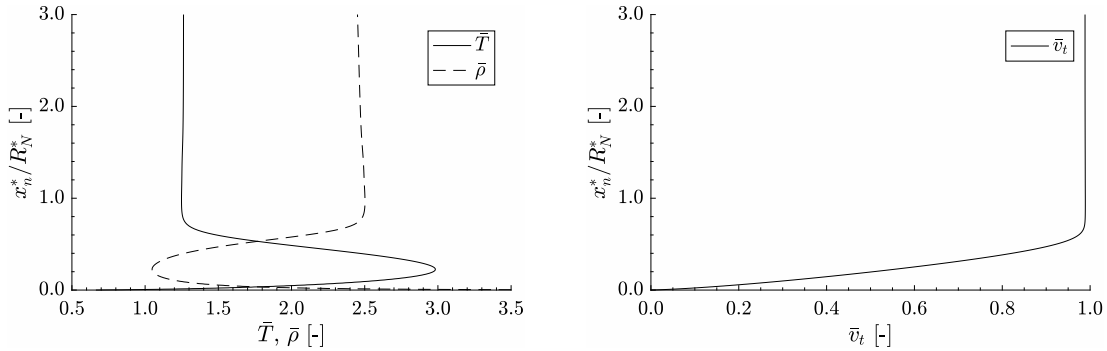

(a) Temperature and density

(b) Physical streamwise velocity component

Figure 5.3: Wall normal distributions along the wall normal distance of the Shot 2 blunted cone at $x_a^* = 0.576$ m.

Hollis et al., respectively, the under–prediction due to the laminar flow assumption, where this result shows a slightly higher wall heat flux compared to the current result. Upstream of the transition location, the under–prediction is likely caused by the thermodynamic model. As the numerical result of Hollis et al., by applying a thermo–chemical non–equilibrium gas model matches the experimental results, it appears that the equilibrium assumption does not match the real physical conditions of the experiment. Because both the chemical reactions and the vibrational excitation are assumed to be in equilibrium, the temperature in the flow–field is lower. This is the case because parts of the energy are stored in the chemical reactions and the vibrational excitation, where, in contrast to the non–equilibrium model, where ongoing chemical reactions and vibrational excitation occur, these parts of the energy are greater. Thus, because of the lower temperatures in the flow–field, the wall heat flux is under–predicted. Nevertheless, this result is used for the boundary–layer stability calculations in the next section because in both solvers, CONSST3D and COSTAS, currently no thermo–chemical non–equilibrium gas model is implemented.

As the boundary–layer stability calculations require an adequate base–flow solution, the non–dimensional wall normal distributions of the temperature and the density in Fig. 5.3a and of the physical streamwise velocity component in Fig. 5.3b are presented along the non–dimensional wall normal distance at $x_a^* = 0.576$ m, respectively, approximately at the transition onset location. It can be recognized that all distributions are smooth without any oscillations in the wall normal direction. Thus, with regard to the validation of the wall distributions and the non–oscillatory wall normal distributions, the boundary–layer stability calculations were performed with the current result as the base–flow solution.

5.1.2 Boundary–Layer Stability Results

The boundary–layer stability calculations were firstly performed approximately at the laminar–turbulent transition onset location at $x_a^* = 0.576$ m by applying the

LST to detect the first and second or higher Mack modes. The calculations were performed with different grid point distributions in the wall normal direction, respectively, 350/400/450/500 grid points. Further, the non–reflecting boundary condition was prescribed at the outer boundary and the spectral Chebyshev collocation method was used for the discretization.

In Fig. 5.4, the current results of the LST calculations are presented versus the disturbance frequency. With respect to the growth rate results of the different number of grid points, in Fig. 5.4a, equal distributions can be observed. Thus, the result containing 400 grid points was used for the further investigations. Comparing the current result with the results of the Stetson cone in the Earth atmosphere in Sec. 4.1.2, similar qualitative growth rate distributions can be observed versus the disturbance frequency but with some slight differences. Firstly, in the current result a second Mack mode can be detected with a maximum growth rate $\sigma^* = 33.29$ 1/m for a disturbance frequency of $f^* = 405$ kHz. Secondly, the growth rate decreases with lower disturbance frequencies but in contrast to the Stetson cone no unstable first mode can be detected. Additionally, for higher disturbance frequencies, the growth rate decreases but in contrast to the Stetson cone the growth rate remains unstable. This unstable behavior can be found up to high disturbance frequencies of $f^* = 1000$ kHz. To distinguish the eigenmodes, the phase speed of the Mack mode and the fast mode are shown versus the disturbance frequency in Fig. 5.4b. The first mode (Mack mode), arising from the slow acoustic spectrum, synchronizes with the fast mode (Mode F) at a disturbance frequency of $f^* = 451.5$ kHz with a phase speed of $c_r = 0.8618$ and, thus, converts to a second Mack mode. Even though the growth rate remains unstable up to very high disturbance frequencies, no conversion to a third mode can be found in the phase speed unlike for the flat plate validation case in Sec. 4.2.2 because no additional synchronization point with a fast mode was found.

For completeness of the LST computation, the absolute values of the eigenfunctions $|\tilde{q}| = (\text{Real}(\tilde{q})^2 + \text{Imag}(\tilde{q})^2)^{1/2}$ of the temperature, density and the physical streamwise and normal velocity components for a disturbance frequency of $f^* =$

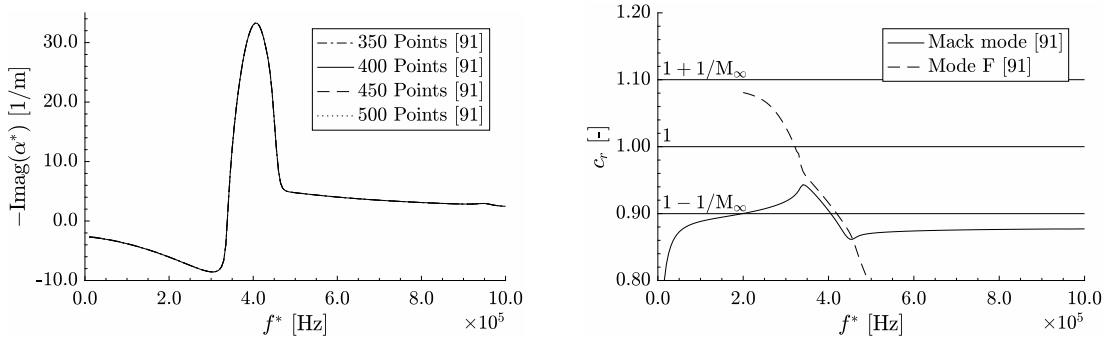

(a) Growth rate distribution versus the disturbance frequency

(b) Phase speed distribution versus the disturbance frequency

Figure 5.4: LST calculations at $x_a^* = 0.576$ m of the Shot 2 blunted cone [91].

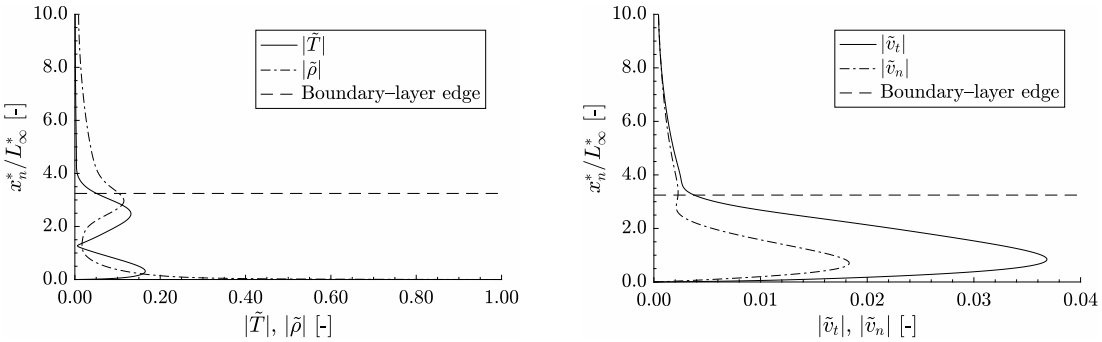

(a) Temperature and density (b) Physical streamwise and normal velocity

Figure 5.5: Absolute values of the eigenfunctions along the wall normal distance of the Shot 2 test case at $x_a^* = 0.576$ m.

405 kHz are shown along the wall normal distance in Fig. 5.5. In these figures, the oscillatory behavior of a second Mack mode inside the boundary–layer and the asymptotic decay in the inviscid region of the flow–field can be recognized.

To determine the N–factor at the laminar–turbulent transition onset location, firstly, the LST was applied along the cone geometry. The resulting growth rate distributions are shown in Fig. 5.6a along the arclength for disturbance frequencies from $f^* = 300$ kHz up to $f^* = 520$ kHz with $\Delta f^* = 20$ kHz. It can be recognized that the maximum growth rate increases with an increase in the disturbance frequency and, additionally, the neutral point moves upstream. Further, a decaying growth rate downstream of the maximum location can be observed, where the growth rate remains unstable along the entire cone. Applying Eq. (3.60) for the calculation of the N–factor, the distributions versus the arclength in Fig. 5.6b were found. The unstable behavior of the growth rate along the entire cone can also be recognized in this figure as the N–factor continues to rise up to the end of the geometry for all disturbance frequencies. Lastly, the N–factor as the criterion for the laminar–

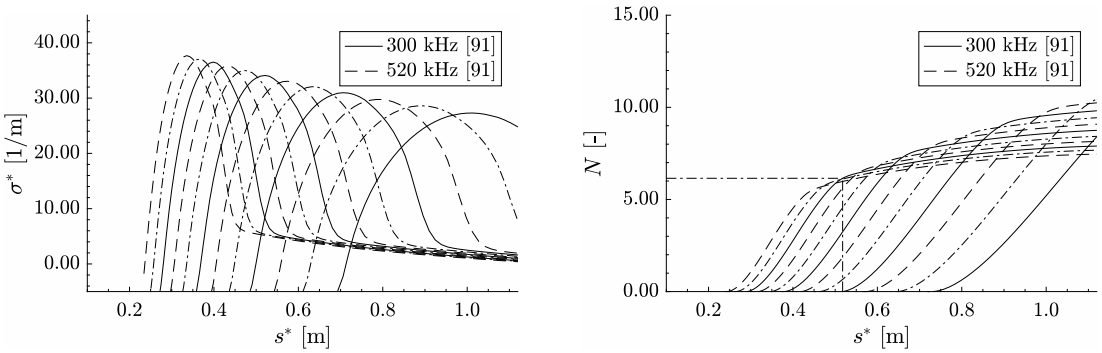

(a) Growth rate distributions (b) N–factor distributions

Figure 5.6: LST calculations along the arclength of the Shot 2 blunted cone [91].

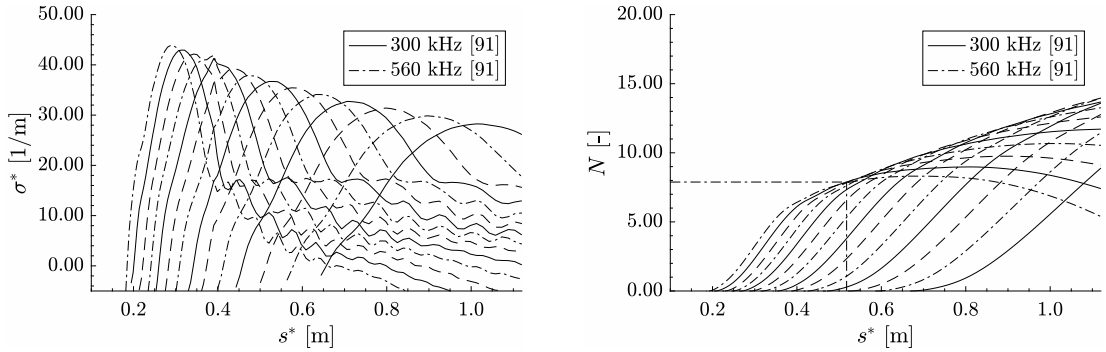

(a) Growth rate distributions

(b) N–factor distributions

Figure 5.7: LPSE calculations along the arclength of the Shot 2 blunted cone [91].

turbulent transition onset was found with $N = 6.15$ for a disturbance frequency of $f^* = 480$ kHz at the laminar–turbulent transition onset location $x_a^* = 0.5325$ m, respectively, $s^* = 0.51772$ m.

A second calculation was performed, applying the LPSE, to account for the downstream propagation of the disturbances. The growth rate distributions along the arclength are presented in Fig. 5.7a for disturbance frequencies from $f^* = 300$ kHz up to $f^* = 560$ kHz with $\Delta f^* = 20$ kHz. Similar to the LST computations, the maximum growth rate increases with an increasing disturbance frequency and the neutral point moves further upstream. Overall greater growth rates were observed and the neutral point moves further upstream compared to the LST. Downstream of the maximum, the growth rate decreases and for the higher disturbance frequencies the growth rate becomes stable in contrast to the LST computations. Further, an oscillatory behavior can be observed which likely arises due to difficulties in the tracking of the second Mack mode because of the appearance of additional unstable modes also observed by Chang et al. [12] and Zanus et al. [104]. In Fig. 5.7b, the resulting N–factor distributions, calculated with Eq. (3.60), along the arclength of the cone are shown. Firstly, the stable behavior of the growth rate for high disturbance frequencies can also be observed in these results, respectively, a decaying N–factor. Secondly, the N–factor at the laminar–turbulent transition onset location was found with $N = 7.88$ for $f^* = 540$ kHz, respectively, a higher N–factor at a higher disturbance frequency compared to the LST. Overall, in both calculations, typical values for the N–factor were found at the laminar–turbulent transition onset location.

5.2 Shot 2 in Mars Atmosphere

5.2.1 Laminar Base–Flow Results

The second test case to investigate the influence of the atmospheres on the boundary–layer stability in this work is the blunted cone of the previous section but a Mars atmosphere was assumed. Therefore, to differentiate the test cases, the test case

of the previous section in the pure CO_2 atmosphere will be labeled as Shot 2 in the following. Different to the pure CO_2 atmosphere, additionally, N_2 is considered in this atmosphere, where the gas composition and the considered species for the thermo–chemical equilibrium gas model can be found in Tab. 2.2. To enable a comparison between the current test case and the Shot 2 test case of Sec. 5.1, the same Mach number, Reynolds number and temperature were chosen similar to Kline et al. [40] who chose the same variables to perform their comparisons on a flat plate. The resulting free–stream parameters can be found in Tab. 5.2. Further, also in this case the thin–layer Navier–Stokes equations were solved with a prescribed wall temperature of $\bar{T}^*_{\mathrm{w}} = 300$ K and with an axisymmetric laminar flow assumption. Additionally, the number of grid points was kept the same, respectively, 300 grid points in the streamwise direction and 200/300/400 in the wall normal direction.

Table 5.2: Free-stream conditions for the blunted cone assuming a Mars atmosphere.

M_∞	Re_∞	p^*_∞ [Pa]	T^*_∞ [K]	ρ^*_∞ [kg/m^3]
9.99	6874	1614.5	452	0.01859

In Fig. 5.8, the current distributions of the non–dimensional wall pressure and the Stanton number along x^*_a are compared to the Shot 2 results. The non–dimensional values are chosen for these figures to exclude the effects of the different static free–stream values such as the free–stream pressure and density. Further, note that the wall pressure is made non-dimensional with the static free–stream pressure. Comparing the results of the different number of grid points overall a good agreement can be observed. Similar to the Shot 2 test case, the pressure distributions in Fig. 5.8a matches well between the different grid resolutions and the Stanton number show only small differences at the junction between the nose and the cone part. Further downstream, the Stanton numbers are comparable and, thus, the same number of grid points as for the Shot 2 test case, respectively, 400 grid points in the wall normal

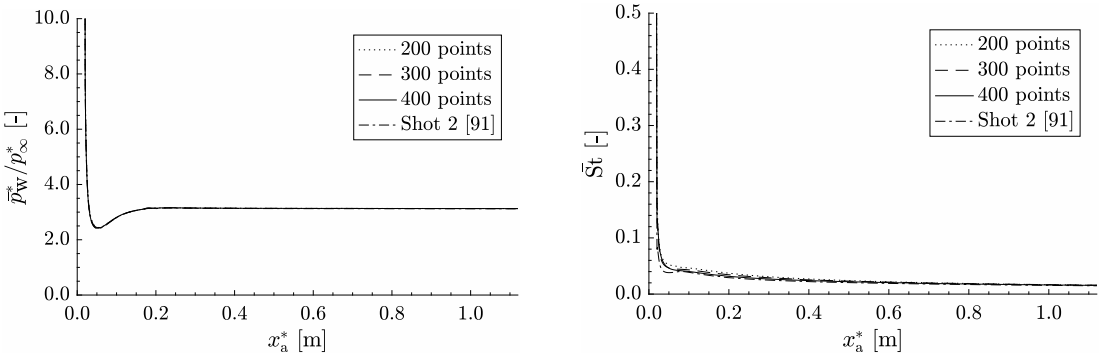

(a) Wall pressure distribution

(b) Wall heat flux distribution

Figure 5.8: Wall distributions along x^*_a of the the blunted cone assuming a Mars atmosphere.

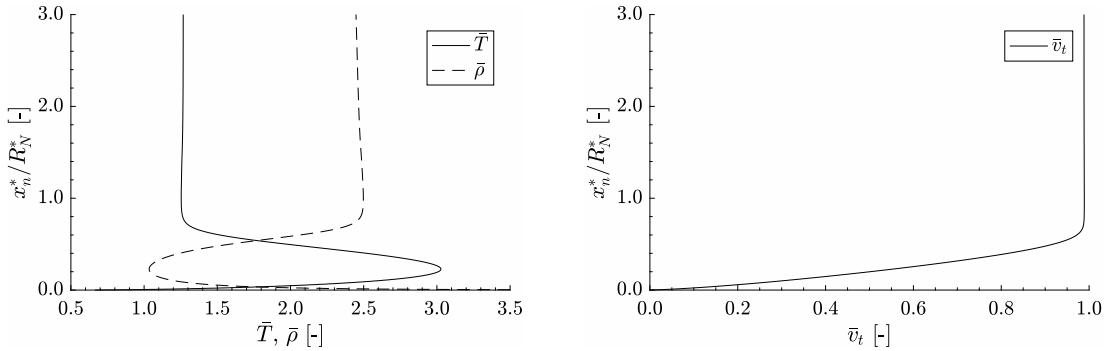

(a) Temperature and density (b) Physical streamwise velocity component

Figure 5.9: Wall normal distributions along the wall normal distance of the blunted cone assuming a Mars atmosphere at $x_a^* = 0.576$ m.

direction, was used for the further investigations and the boundary–layer stability calculations. Comparing the current pressure distribution with the pressure distribution of the Shot 2 test case in Fig. 5.8a, no significant difference can be observed between the results. Similar observations can be made for the Stanton number in Fig. 5.8b, respectively, the current values are comparable to the values of the Shot 2 test case. Thus, due to the same grid point distributions and the similarity in the free-stream parameters between the two cases, the additional consideration of N_2 in the atmosphere has no significant influence on the non–dimensional base–flow results.

In Fig. 5.9, the wall normal distributions of the flow variables are presented at $x_a^* = 0.576$ m. The distributions of the non–dimensional temperature and density in Fig. 5.9a and of the physical streamwise velocity in Fig. 5.9b along the non–dimensional wall normal distance show smooth profiles without oscillations similar to the results of the Shot 2 test case. Thus, the current base–flow solution was used to perform the boundary–layer stability calculations, where the results will be presented in the following section.

5.2.2 Boundary–Layer Stability Results

With the previously calculated base–flow result, firstly, the LST was applied at the same location of $x_a^* = 0.576$ m as for the Shot 2 test case to enable a comparison between the results. The calculation was performed for different number of grid points in the wall normal direction, respectively, 350/400/450/500 grid points. To enable a comparison with the Shot 2 boundary–layer stability calculations, also in this case the non–reflecting boundary conditions were chosen at the outer boundary and the Chebyshev spectral collocation method was applied in the wall normal direction.

In Fig. 5.10, the resulting growth rate and the phase speed distributions versus the disturbance frequency are shown, where the growth rate is presented for the different number of grid points. Similar to the Shot 2 result, also in this case no significant differences can be observed between the growth rates of the different grid

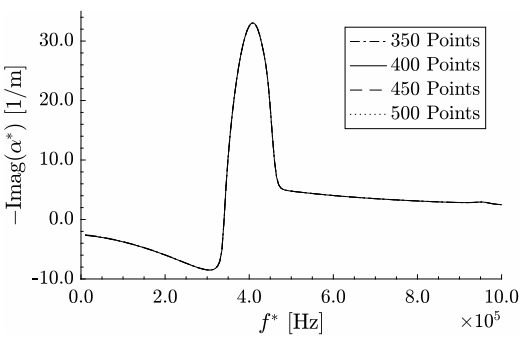

(a) Growth rate distribution versus the disturbance frequency

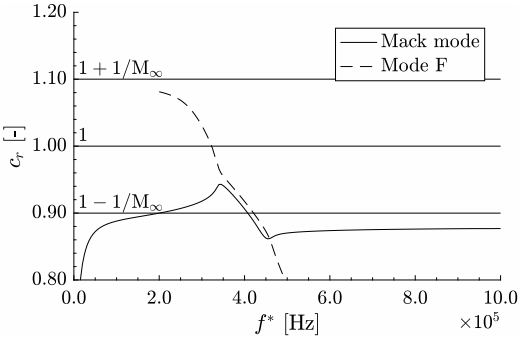

(b) Phase speed distribution versus the disturbance frequency

Figure 5.10: LST calculations at $x_a = 0.576$ m of the blunted cone assuming a Mars atmosphere.

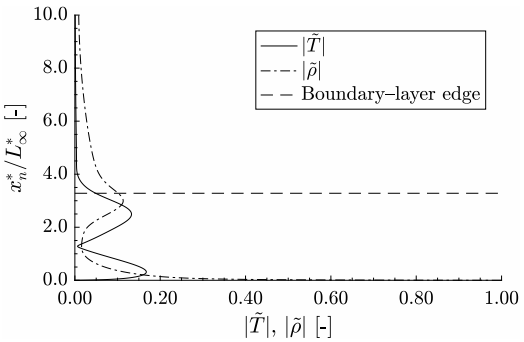

(a) Temperature and density

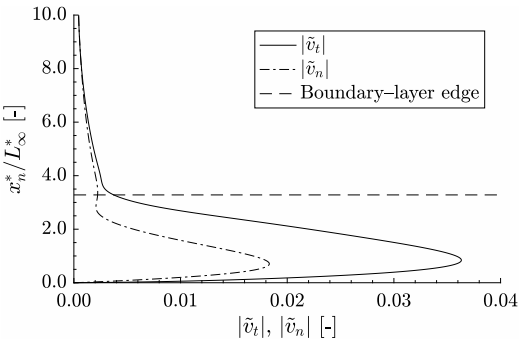

(b) Physical streamwise and normal velocity

Figure 5.11: Absolute values of the eigenfunctions along the wall normal distance of the blunted cone assuming a Mars atmosphere at $x_a^* = 0.576$ m.

distributions. Thus, to enable a comparison between the current result and the Shot 2 result, the same number of grid points as for the Shot 2 test case was chosen, respectively, 400 points in the wall normal direction. The growth rate in Fig. 5.10a shows a qualitatively similar result compared to the result of the Shot 2 test case, respectively, an unstable second Mack mode, a stable first mode and an unstable behavior up to high frequencies. The current maximum growth rate of the second Mack mode can be found at a frequency of $f^* = 410$ kHz with $\sigma^* = 33.06$ 1/m. To verify the second Mack mode appearance, the phase speed is shown in Fig. 5.10b along the disturbance frequency, where the synchronization point between the fast mode (Mode F) and the Mack mode, respectively, the conversion from the first to the second mode, was found at $f^* = 453.3$ kHz with $c_r = 0.8619$. For higher disturbance frequencies, also in this case no conversion to a third mode can be observed.

Lastly, in the LST investigations at $x_a^* = 0.576$ m, the eigenfunctions of the absolute disturbance temperature and density are shown in Fig. 5.11a and the absolute

disturbance velocity components in Fig. 5.11b. Both figures show the eigenfunctions along the non–dimensional wall normal distance for the disturbance frequency of the maximum growth rate $f^* = 410$ kHz including the location of the boundary–layer edge. Similar profiles can be observed compared to the Shot 2 eigenfunctions with an oscillatory behavior inside the boundary–layer and an asymptotic decay in the inviscid region.

In the following, the LST and LPSE results along the cone are presented. The LST results are shown in Fig. 5.12, where the growth rate distributions are presented in Fig. 5.12a and the N–factor distributions in Fig. 5.12b along the cone arclength. In both figures, the distributions are shown for disturbance frequencies from $f^* = 300$ kHz to $f^* = 520$ kHz with $\Delta f^* = 20$ kHz. Similar to the other results in this section, qualitatively comparable results to the Shot 2 test case can be observed in the growth rate distributions but the growth rates show slightly higher values and the neutral points can be found slightly upstream compared to the Shot 2 test case. Downstream of the maximum of the growth rates, the growth rates decay but an unstable behavior can be observed for all presented disturbance frequencies up to the end of the cone. In case of the LST calculations in the Mars atmosphere, an N-factor of $N = 6.22$ was found for a disturbance frequency of $f^* = 480$ kHz at the laminar–turbulent transition onset location $s^* = 0.51772$ m of the Shot 2 test case. Respectively, by assuming a Mars atmosphere and the same laminar–turbulent transition onset location of the Shot 2 test case, a slightly higher N–factor at the same disturbance frequency can be found.

To examine the influence of the different atmosphere on the LPSE, the results of these calculations are presented in Fig. 5.13 for disturbance frequencies from $f^* = 300$ kHz to $f^* = 560$ kHz with $\Delta f^* = 20$ kHz. The growth rate distributions along the cone arclength, shown in Fig. 5.13a, again show qualitatively similar distributions to the Shot 2 test case but the maximum growth rates show higher values and the neutral points can be found slightly upstream compared to the Shot 2 test case. Further, also in this case an oscillatory behavior can be recognized downstream of

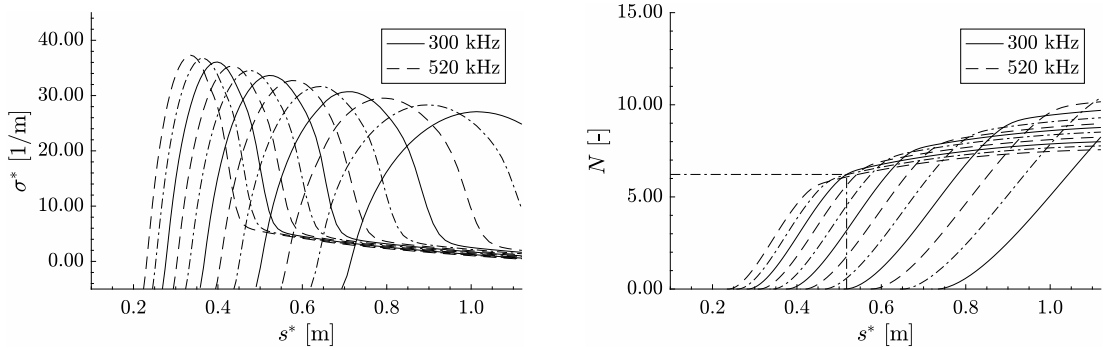

(a) Growth rate distributions

(b) N–factor distributions

Figure 5.12: LST calculations along the arclength of the blunted cone assuming a Mars atmosphere.

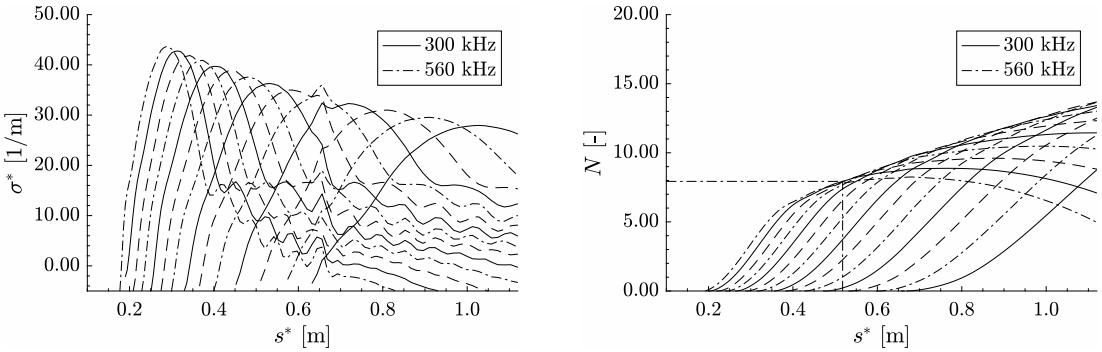

(a) Growth rate distributions

(b) N–factor distributions

Figure 5.13: LPSE calculations along the arclength of the blunted cone assuming a Mars atmosphere.

the maximum of the growth rates which also likely appears due the occurrence of additional unstable modes beside the second Mack mode. Additionally, also in this case, a stable behavior of the growth rate was found for high disturbance frequencies. In case of the current LPSE calculations, the N–factor at the Shot 2 laminar–turbulent transition onset location $s^* = 0.51772$ m was found for a disturbance frequency of $f^* = 540$ kHz with $N = 7.93$. Respectively, in case of the LPSE calculations, the N–factor is also found to be slightly higher compared to the Shot 2 result for the same disturbance frequency.

5.3 Shot 2 in Earth Atmosphere

5.3.1 Laminar Base–Flow Results

The last test case in this work to examine the influence of the atmosphere on the boundary–layer stability is the blunted cone but by assuming an Earth atmosphere, respectively, air, where the gas composition and the considered species for the thermo–chemical equilibrium gas model can be found in Tab. 2.2. The calculations were performed similar to the Mars atmosphere test case by requiring the same Mach number, Reynolds number and temperature as in the Shot 2 test case in Sec. 5.1. This requirement results in the free–stream conditions that can be found in Tab. 5.3.

Table 5.3: Free-stream conditions for the blunted cone assuming an Earth atmosphere.

M_∞	Re_∞	p^*_∞ [Pa]	T^*_∞ [K]	ρ^*_∞ [kg/m^3]
9.99	6874	2124.4	452	0.01631

Analogous to the test cases in the last sections, the calculations were performed

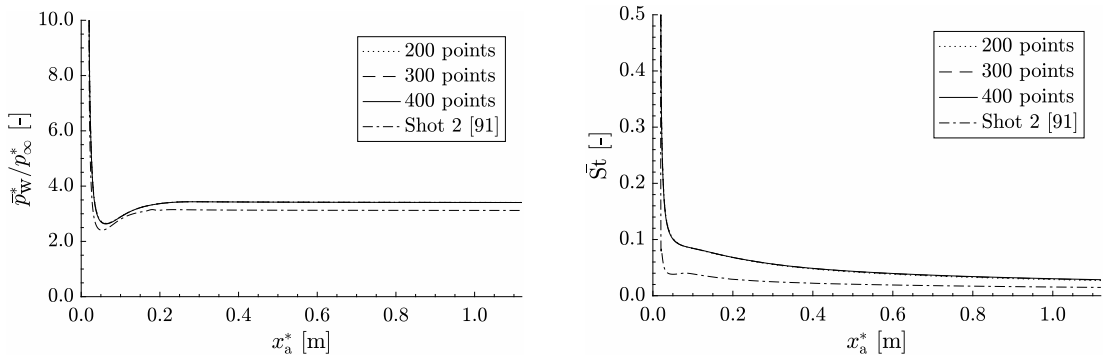

(a) Wall pressure distribution (b) Wall heat flux distribution

Figure 5.14: Wall distributions along x_a^* of the the blunted cone assuming an Earth atmosphere.

applying the thin–layer Navier–Stokes equations requiring an axisymmetric laminar flow and assuming an isothermal wall with $\bar{T}^*_w = 300$ K. Further, 300 grid points were prescribed in the streamwise direction and 200/300/400 in the wall normal direction.

The resulting base–flow solutions of the different grid distributions are presented in Fig. 5.14 and a comparison to the Shot 2 test case is made. Therefore, again the non–dimensional wall pressure and the Stanton number are presented to exclude the effects of the different static free-stream variables. Firstly, it can be recognized that the non–dimensional wall pressure for the different grid distributions along x_a^* in Fig. 5.14a show similar distributions analogous to the previous test cases. Secondly, by comparing the results with the Shot 2 test case, the wall pressure shows greater values due to the different atmosphere which will be explained later in this section. Similar to the wall pressure distributions, the Stanton number in Fig. 5.14b shows the same trend in the comparison to the Shot 2 test case. Firstly, the different number of grid points show similar results and, secondly, the Stanton number is higher compared to the Shot 2 test case which is caused by higher temperatures in the flow–field due to the different atmosphere. Therefore, with regard to the results of the different grid distributions, also in the current test case the result with 400 points in the wall normal direction was chosen for the further investigations and the boundary–layer stability calculations.

As mentioned before, the difference in the wall distributions arises due to the different atmospheres in the calculations because a similarity is required in the free–stream. The Earth atmosphere model in this work considers diatomic molecules, e.g., N_2 and O_2. In contrast, for the Shot 2 test case, CO_2 was included which is a triatomic molecule. The difference in the flow–field, thus, is caused by the isentropic coefficient which is lower in case of CO_2. In consequence, by applying the normal shock relations for a perfect gas as a first approximation, the pressure and the temperature ratios over the bow shock are higher in the Earth atmosphere case compared to the CO_2 case. Respectively, the temperature and the pressure in the entire flow–field are

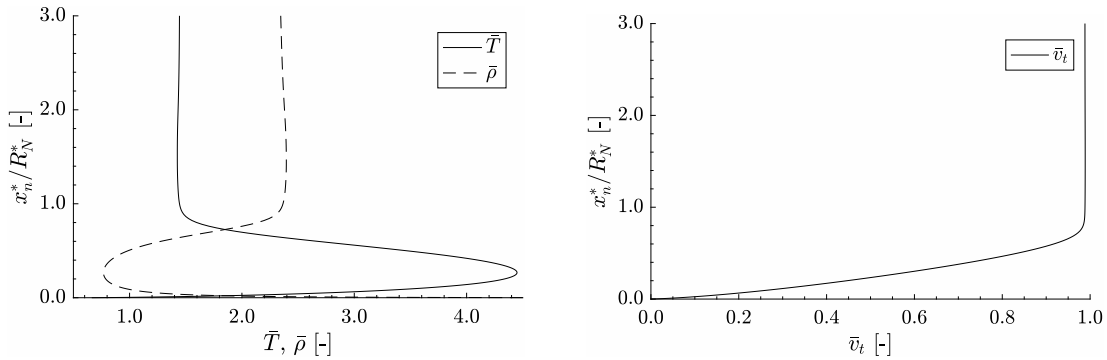

(a) Temperature and density

(b) Physical streamwise velocity component

Figure 5.15: Wall normal distributions along the wall normal distance of the blunted cone assuming an Earth atmosphere at $x_a^* = 0.576$ m.

higher by assuming air. This higher temperature can be recognized as an example in Fig. 5.15a along the non–dimensional wall normal distance at $x_a^* = 0.576$ m. Further, by considering the Earth atmosphere, different chemical reactions occur compared to the pure CO_2 atmosphere which has an additional effect on the wall distributions.

For completeness of the results, the non–dimensional density and temperature distributions are shown in Fig. 5.15a and the non–dimensional physical streamwise velocity component is presented in Fig. 5.15b. All of these profiles, similar to the previous results, show non–oscillatory distributions and, thus, the current result was used to perform the boundary–layer stability calculations.

5.3.2 Boundary–Layer Stability Results

With the previously calculated base–flow solution, firstly, the LST computations were performed at the same location $x_a^* = 0.576$ m as for the previous test cases. Additionally, the same number of grid points was prescribed in the wall normal direction, respectively, 350/400/450/500 grid points. Further, the non–reflecting boundary condition was set at the outer boundary and the Chebyshev spectral collocation method was applied for the discretization in the wall normal direction.

The results of these calculations are presented in Fig. 5.16 along the disturbance frequency. Also in this case, no significant difference can be observed between the growth rate results of the different grid distributions and, thus, the result with 400 grid points was chosen for the following investigations. Comparable to the Shot 2 test case, in the growth rate distribution in Fig. 5.16a, no unstable first mode can be recognized but, for higher disturbance frequencies, the results show different distributions. In contrast to the previous two test cases, firstly, the maximum of the growth rate of the second Mack mode shows a smaller value with $\sigma^* = 24.39$ 1/m at a higher disturbance frequency of $f^* = 535$ kHz. Secondly, the growth rate decreases for higher disturbance frequencies and the Mack mode becomes and remains stable up to high disturbance frequencies. In Fig. 5.16b, the phase speed distributions along

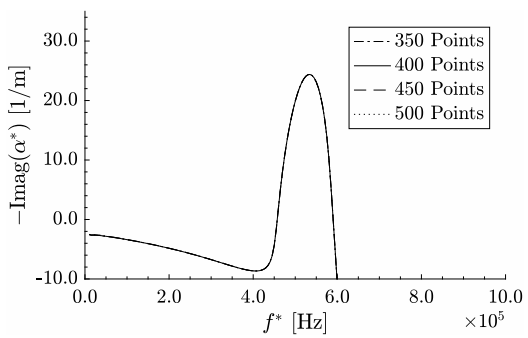

(a) Growth rate distribution versus the disturbance frequency

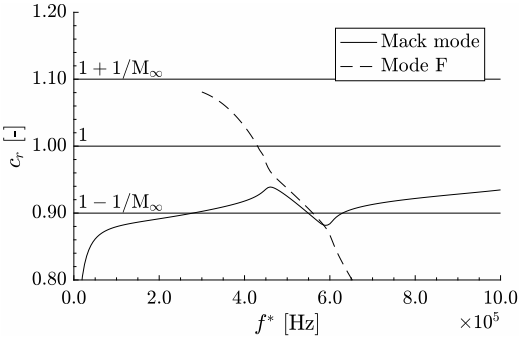

(b) Phase speed distribution versus the disturbance frequency

Figure 5.16: LST calculations at $x_a = 0.576$ m for the blunted cone assuming an Earth atmosphere.

the disturbance frequency show a qualitatively similar distribution compared to the other test cases but the synchronization point between the fast mode (Mode F) and the Mack mode, respectively, the conversion from the first to the second mode, can be found at a higher disturbance frequency of $f^* = 580.29$ kHz with $c_r = 0.8821$. Further, also in the current result no conversion to a third mode can be recognized.

Lastly, for the LST calculations approximately at the transition onset location, the eigenfunctions are presented along the non–dimensional wall normal distance in Fig. 5.17. The absolute values of the density and the temperature in Fig. 5.17a as well as the absolute values of the velocity components in Fig.5.17b show qualitatively similar distributions compared the the previous results with the oscillatory behavior inside the boundary–layer and the asymptotic decay in the inviscid region.

The LST and LPSE calculations along the cone surface are performed also for this test case and are presented in the following. Firstly, the results of the LST are shown

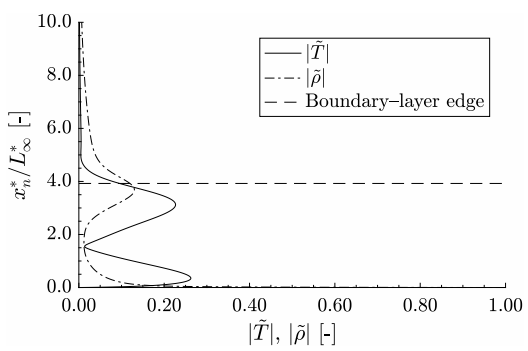

(a) Temperature and density

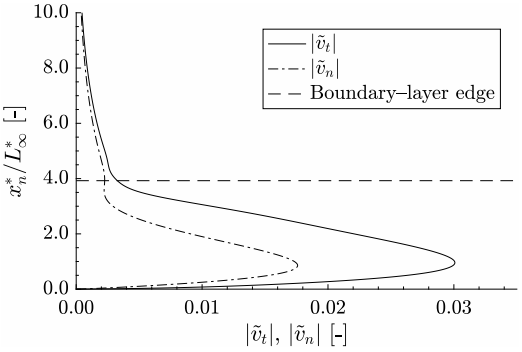

(b) Physical streamwise and normal velocity

Figure 5.17: Absolute values of the eigenfunctions along the wall normal distance of the blunted cone assuming an Earth atmosphere at $x_a^* = 0.576$ m.

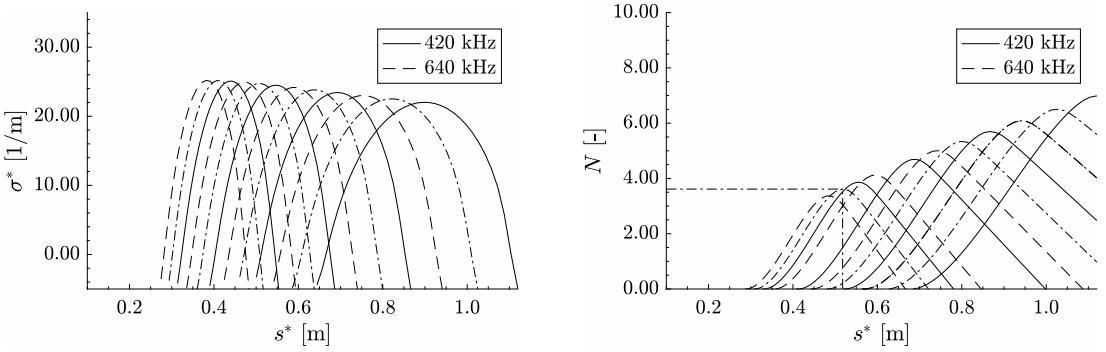

(a) Growth rate distributions (b) N–factor distributions

Figure 5.18: LST calculations along the arclength of the blunted cone assuming an Earth atmosphere.

along the cone surface arclength for disturbance frequencies from $f^* = 420$ kHz to $f^* = 640$ kHz with $\Delta f^* = 20$ kHz, where the growth rate distributions are shown in Fig. 5.18a and the N–factor distributions in Fig. 5.18b. Compared to the previous test cases, the growth rate distributions along the cone surface show smaller maximum values and, in addition, the second Mack mode becomes stable at some location downstream of the maximum of the growth rates of the different disturbance frequencies. Therefore, a decaying behavior can be observed in the N–factor distributions downstream of the maximum. Lastly, the N–factor at the transition onset location of $s^* = 0.51772$ m was found with $N = 3.61$ for $f^* = 620$ kHz. Therefore, compared to the Mars and pure CO_2 atmospheres, a smaller N–factor at a higher disturbance frequency can be observed.

In the LPSE calculations, presented in Fig. 5.19, similar observations as for the LST can be made. With regard to the growth rate distributions for disturbance frequencies from $f^* = 420$ kHz to $f^* = 640$ kHz with $\Delta f^* = 20$ kHz along the cone

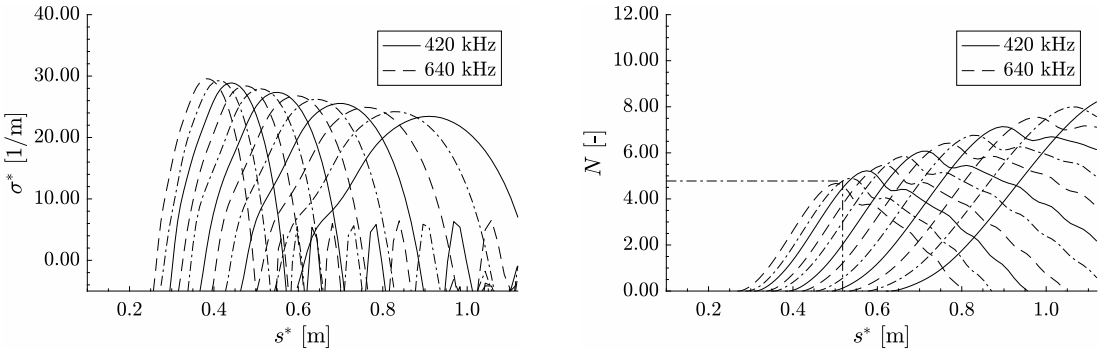

(a) Growth rate distributions (b) N–factor distributions

Figure 5.19: LPSE calculations along the arclength of the blunted cone assuming an Earth atmosphere.

surface, firstly, higher values compared to the current LST calculations are found and the neutral points move slightly upstream. Secondly, in contrast to the other atmospheres, smaller growth rates are found which show a decreasing behavior for all disturbance frequencies downstream of the maximum. Similar to the previous test cases, also in the current results an oscillatory behavior can be observed downstream of the maximum growth rate. In the N–factor distributions in Fig. 5.19b, the stable behavior of the instabilities can also be recognized downstream of the maximum. Further, in the current test case an N–factor of $N = 4.78$ can be found for a disturbance frequency of $f^* = 620$ at the Shot 2 laminar–turbulent transition onset location. Respectively, a greater N–factor compared to the current LST results is observed but a smaller one compared to the test cases considering the other atmospheres.

5.4 Influence of the Atmosphere on the Boundary–Layer Stability

To investigate the influence of the different atmospheres on the boundary–layer stability, in this section, the previously presented results will be compared with each other and a discussion on the differences will be made. Firstly, a side by side comparison of the growth rates from the different LST calculations at $x_a^* = 0.576$ m is shown in Fig. 5.20. In Fig. 5.20a, the dimensional growth rate distributions versus the dimensional disturbance frequency are presented for the three different atmospheres, whereas, in Fig. 5.20b, the same values are shown but in the non–dimensional form. In the former, it can be seen that the CO_2 and the Mars atmosphere show similar distributions over the whole disturbance frequency range. Thus, as mentioned before, the consideration of the small amount of 4.634 vol % N_2 in the atmosphere has no significant influence on the LST calculations. In consequence, with respect to the current LST results, the experimental test runs of Hollis et al. [28], considering pure

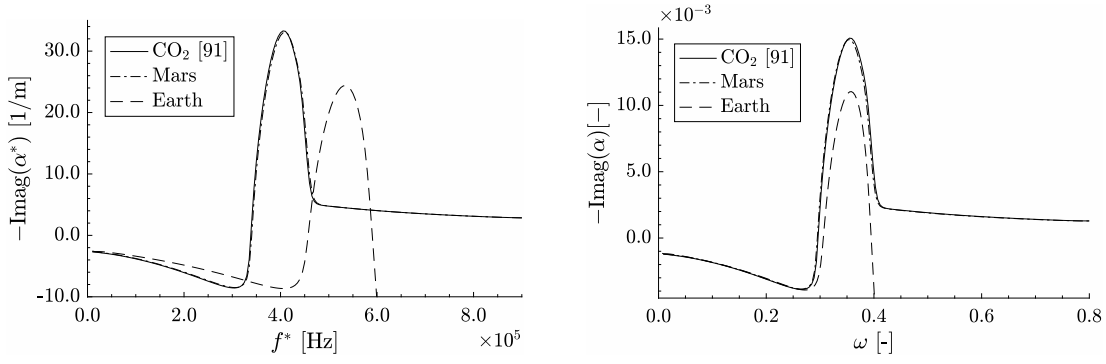

(a) Growth rate distribution versus the disturbance frequency

(b) Non–dimensional growth rate distribution versus the non–dimensional angular disturbance frequency

Figure 5.20: Comparison of the LST growth rates of the different atmospheres.

CO_2, are a good approximation of the Mars atmosphere conditions. Comparing the growth rate considering the CO_2 atmosphere with the result considering the Earth atmosphere, significant differences can be observed. Firstly, the Earth atmosphere shows a stabilizing effect on the second Mack mode, respectively, a significantly lower growth rate. This observation is contrary to the thermo–chemical non–equilibrium stabilizing effects of the injection of CO_2 into air outlined in Sec. 1.3 and observed by Kline et al. [40] applying a thermo–chemical non–equilibrium gas model but agree with the observations made by Kline et al. [40] applying a finite rate chemistry model. Secondly, the maximum in the growth rate can be found at a higher disturbance frequency in the Earth atmosphere compared to the other atmospheres in this work. Additionally, in contrast to the other atmospheres, a stable Mack mode can be recognized in the Earth atmosphere at high disturbance frequencies. In Fig. 5.20b, the non–dimensional values are presented to exclude the influence of the free–stream variables in the LST and to enable the comparison with regard to the atmosphere only. In this case, the growth rates of the CO_2 and the Mars atmosphere also show similar distributions along the complete disturbance frequency range. Comparing the growth rate of the Earth atmosphere with the other atmospheres, again the stabilizing effect of air can be seen. In contrast to the dimensional representation in Fig. 5.20a, the non–dimensional angular frequency at the maximum growth rate of the Earth atmosphere shows only a small shift to higher values with $\omega = 0.3581$ compared to $\omega = 0.3545$ in the CO_2 and $\omega = 0.3553$ in the Mars atmosphere. Thus, in the non–dimensional form, the maximum of the second Mack mode growth rate appears at nearly the same non–dimensional angular disturbance frequencies.

Further comparisons are made with regard to the phase speed and the eigenfunctions in the following, where, firstly, the phase speeds along the non–dimensional angular frequency are shown in Fig. 5.21a. Similar to the growth rates, the phase speed shows comparable distributions between the CO_2 and the Mars atmosphere. Comparing these distributions with the phase speed of the Earth atmosphere test case, qualitatively similar distributions can be observed for the lower disturbance frequencies but at high frequencies differences occur between the results. Until the maximum of the phase speeds, qualitatively similar distributions can be observed between the test cases. Thereafter, the phase speeds of the CO_2 and the Mars atmosphere decrease and remain below the slow acoustic branch $1 - 1/M_\infty$, whereas the phase speed of the Earth atmosphere decreases and, thereafter, rises again and the phase speed crosses the slow acoustic branch again.

Lastly, the absolute values of the eigenfunctions are compared with each other. Therefore, all eigenfunctions are scaled so that the maximum values of the temperature eigenfunctions match with the maximum of the CO_2 atmosphere temperature eigenfunction. The resulting eigenfunctions for the temperature, physical streamwise velocity and normal velocity are presented in Fig. 5.21b – 5.21d. Overall, qualitatively similar distributions can be observed between the different cases for all presented eigenfunctions. By comparing the CO_2 and the Mars atmosphere with each other, the eigenfunctions also show a quantitatively good agreement. This behavior corresponds to the previous observations, respectively, that the small amount of N_2

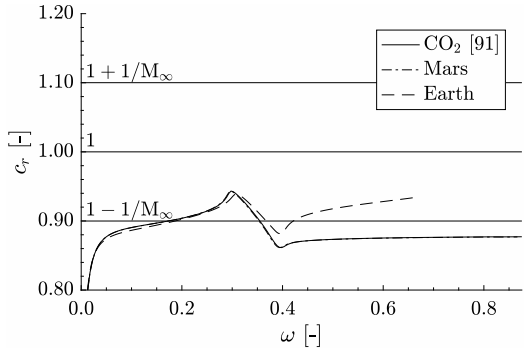

(a) Phase speed distributions versus the non–dimensional angular disturbance frequency

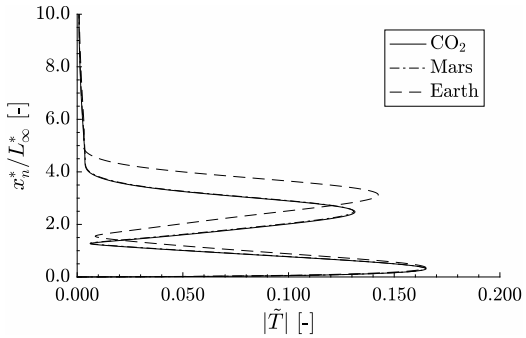

(b) Absolute values of the temperature eigenfunctions along the wall normal distance

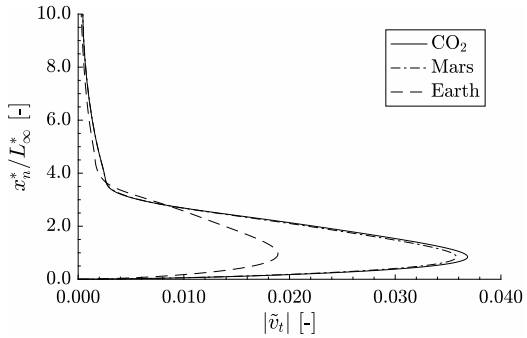

(c) Absolute values of the physical streamwise velocity eigenfunctions along the wall normal distance

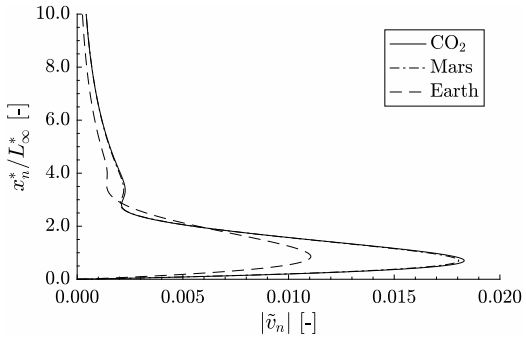

(d) Absolute values of the physical normal velocity eigenfunctions along the wall normal distance

Figure 5.21: Comparison of the LST phase speeds and eigenfunctions of the different atmospheres.

in the atmosphere has only a small effect on the result. In contrast, the eigenfunctions for the Earth atmosphere show different values along the wall normal distance. Additionally, it can be recognized that the asymptotic decay of the eigenfunctions in the Earth atmosphere arise at a greater distance from the wall which is caused by the greater boundary–layer thickness, where the values can be found in Tab. 5.4.

In Tab. 5.5, the N–factors of the LST and LPSE calculations considering the three different atmospheres are presented. Firstly, it can be recognized that the disturbance frequencies at the laminar–turbulent transition onset location show the

Table 5.4: Boundary–layer thicknesses for the different atmospheres at $x_a^* = 0.576$ m.

Atmosphere	δ^*/L_∞^* [-]	δ^* [mm]
CO_2	3.2462	1.4697
Mars	3.2812	1.4857
Earth	3.9244	1.7768

Table 5.5: N–factors at the laminar–turbulent transition onset location $x_a^* = 0.5325$ m for the different atmospheres.

Atmosphere	LST f^* [kHz]	LST N [-]	LPSE f^* [kHz]	LPSE N [-]
CO_2	480	6.15	540	7.88
Mars	480	6.22	540	7.93
Earth	620	3.61	620	4.78

same values for the CO_2 and Mars calculations. In contrast, in case of considering the Earth atmosphere, the disturbance frequency is larger. This trend can be recognized in both, the LST and the LPSE, calculations. Further, it can be recognized that the disturbance frequencies show higher values comparing the LPSE with the LST calculations in the CO_2 and Mars case, whereas, in the Earth atmosphere, the disturbance frequency remains the same. By comparing the N–factors of the CO_2 and the Mars atmosphere, which show similar values, again it can be noticed that the experimental investigation of Hollis et al. under CO_2 atmosphere conditions is a good representation of the Mars atmosphere. Lastly, the stabilizing effect of the Earth atmosphere compared to the CO_2 and the Mars atmosphere can be recognized also in the N–factors at the transition onset location. Thus, requiring the same Mach number, Reynolds number and temperature in the free–stream and the transition N–factor of the CO_2 atmosphere, the laminar–turbulent transition occurs further upstream in the CO_2 and the Mars atmosphere compared to the Earth atmosphere by applying a thermo–chemical equilibrium gas model.

5.5 Shot 4 in CO_2 Atmosphere

5.5.1 Laminar Base–Flow Results

To examine the influence of the free–stream Reynolds number on the same blunted cone geometry, in this section, the Shot 4 condition of Hollis et al. [28] will be investigated. The geometry consists of the same geometrical parameters as for the previous test cases but with the free–stream parameters in Tab. 5.6. It can be recognized that this test case is characterized by a significantly higher Reynolds number compared to the Shot 2 conditions, whereas only moderate differences occur in the Mach number

Table 5.6: Free-stream conditions for the blunted cone of Hollis et al. under the Shot 4 conditions [28].

M_∞	Re_∞	p_∞^* [Pa]	T_∞^* [K]	ρ_∞^* [kg/m^3]
9.59	13167	3433	478	0.03802

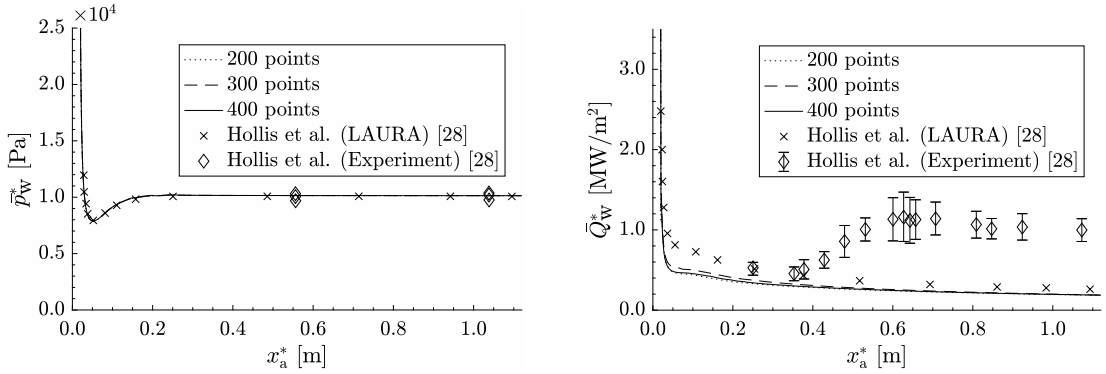

(a) Wall pressure distribution (b) Wall heat flux distribution

Figure 5.22: Wall distributions along x^*_a of the Shot 4 blunted cone.

and the temperature. In the calculations, analogous to the previous test cases, the thin–layer Navier–Stokes equations were solved with an isothermal wall temperature of $\bar{T}^*_w = 300$K. Further, the thermo–chemical equilibrium gas model for pure CO_2 was applied and a laminar axisymmetric flow was assumed. Additionally, the same grid distributions, consisting of 300 points in the streamwise direction and 300/350/400 grid points in the wall normal direction, were used.

In Fig. 5.22, the base–flow results are compared to the experimental and numerical results, computed with LAURA, of [28]. Additionally, the current results of the different grid distributions are compared with each other. The wall pressure distributions along x^*_a, presented in Fig. 5.22a, show similar distributions for the different number of grid points. Further, comparing the results with the referenced experimental and numerical results, a good agreement was found along the entire cone surface. In case of the heat flux at the wall, presented in Fig. 5.22b along x^*_a, again similar results with respect to the different grid point distributions are observed with only small differences at the nose–cone junction. Thus, the result containing 400 grid

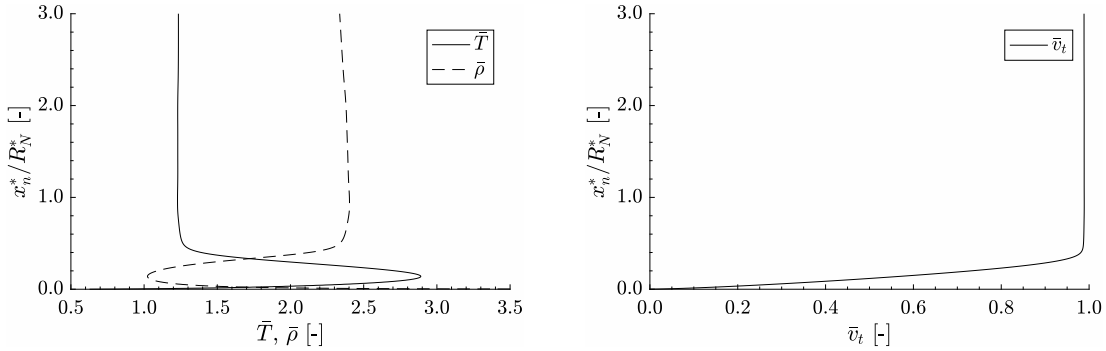

(a) Temperature and density (b) Physical streamwise velocity component

Figure 5.23: Wall normal distributions along the wall normal distance of the Shot 4 blunted cone at $x^*_a = 0.372$ m.

points in the wall normal direction was used for the further investigations and the following boundary–layer stability calculations. In comparison with the referenced experimental and numerical results, similar observations can be made as for the Shot 2 test case. Respectively, the wall heat flux is under–predicted in the current computation which is caused by the thermo–chemical equilibrium gas model, where the explanation of the phenomenon was given in Sec. 5.1.1. Nevertheless, the result is used for the boundary–layer stability calculations due to the currently unavailable thermo–chemical non–equilibrium gas model in the solvers.

Lastly, in Fig. 5.23, the non–dimensional wall normal profiles of the base–flow solution at $x_a^* = 0.372$ m, used for the LST computations in the next section, are presented. The temperature and density distributions in Fig. 5.23a as well as the physical streamwise velocity distribution in Fig. 5.23b show non–oscillatory profiles and, thus, the LST computations were performed with this base–flow result and the results are presented in the following.

5.5.2 Boundary–Layer Stability Results

The boundary–layer stability calculations of the Shot 4 test case were firstly performed at $x_a^* = 0.372$ m, approximately at the laminar–turbulent transition onset location, applying the LST, where the Chebyshev spectral collocation method and the non–reflecting boundary condition at the outer boundary were applied. Further, the stability grid consisted of 350/400/450/500 grid points in the wall normal direction. The calculations were performed upstream of the location of the Shot 2 test case because the laminar–turbulent transition onset location can be found further upstream. In Fig. 5.22b, the rise in the heat flux was found at $x_a^* = 0.353$ m, respectively at $s^* = 0.33687$ m.

Comparing the growth rate distributions versus the disturbance frequency for the different number of grid points in Fig. 5.24a, a good agreement can be observed between the results. Thus, similar to the other test cases, a grid point distribution containing 400 grid points in the wall normal direction was chosen for the further

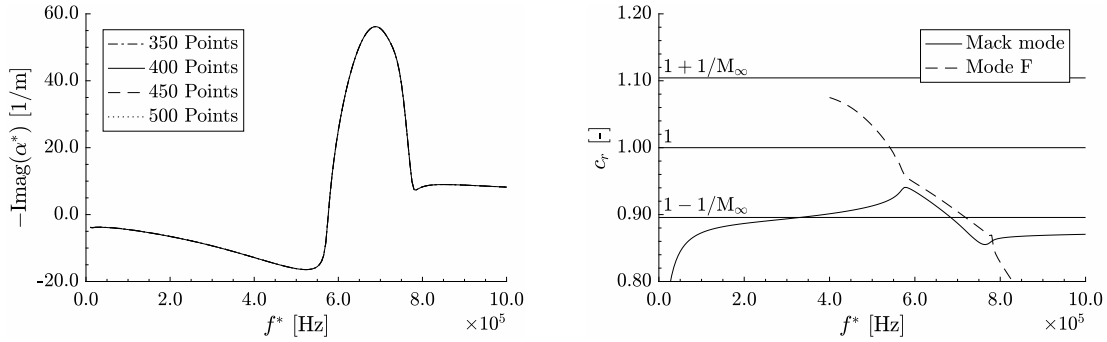

(a) Growth rate distribution versus the disturbance frequency

(b) Phase speed distribution versus the disturbance frequency

Figure 5.24: LST calculations at $x_a = 0.372$ m for the Shot 4 blunted cone.

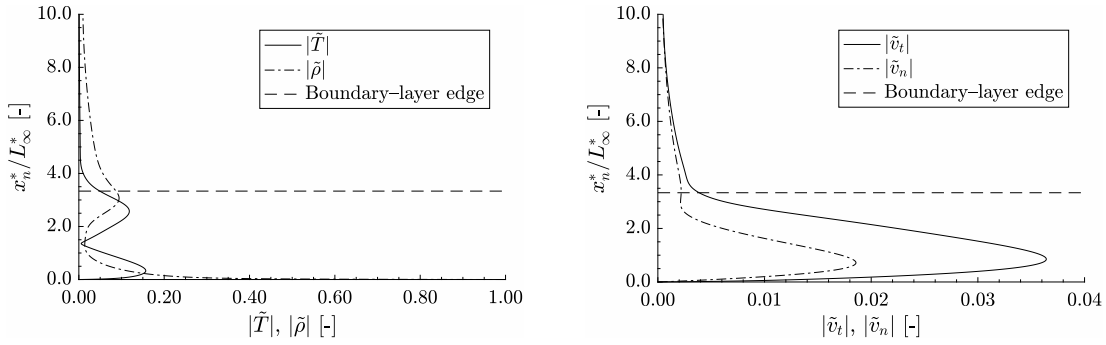

(a) Temperature and density

(b) Physical streamwise and normal velocity

Figure 5.25: Absolute values of the eigenfunctions along the wall normal distance of the Shot 4 test case at $x_a^* = 0.353$ m.

investigations. The overall distribution of the growth rate, further, is qualitatively comparable to the Shot 2 test case but with a shift to higher disturbance frequencies and with greater values for the growth rate. In the distribution, the second Mack mode can be found with a maximum of $\sigma^* = 56.191/\text{m}$ at $f^* = 690$ kHz. For lower disturbance frequencies, the growth rate becomes stable, respectively, no unstable first mode can be found. For higher disturbance frequencies, also in this case, the growth rate decreases but remains unstable up to high disturbance frequencies. The phase speed distribution versus the disturbance frequency in Fig. 5.24b also shows a qualitatively similar distribution compared to the Shot 2 test case but also with a shift to higher frequencies. The Mack mode, arising from the slow acoustic spectrum, converts from a first mode to a second mode at the synchronization point with the fast mode (Mode F) at $f^* = 777$ kHz with $c_r = 0.8609$. With an increasing disturbance frequency, the values of the phase speed remain below the acoustic branch as observed for the Shot 2 test case.

Lastly, in Fig. 5.25, the absolute values of the eigenfunctions are presented along the non–dimensional wall normal distance. Comparable to the Shot 2 test case, the oscillatory behavior inside the boundary–layer of the density and temperature distributions in Fig. 5.25a and of the physical velocity component distributions in Fig. 5.25b can be observed along with the asymptotic decay in the inviscid region.

To investigate the evolution of the instabilities along the blunted cone under the Shot 4 test conditions, LST calculations were performed along the geometry. The resulting growth rates and the N–factors along the cone arclength are presented in Fig. 5.26 for disturbance frequencies from $f^* = 620$ kHz to $f^* = 840$ kHz with $\Delta f^* = 20$ kHz. The growth rates in Fig. 5.26a again show qualitatively similar distributions compared to the Shot 2 test case with an unstable behavior up to the end of the geometry for all disturbance frequencies. Nevertheless, the growth rates are greater and the neutral points move upstream with respect to the Shot 2 test case. Due to the unstable growth rate along the entire geometry, the calculated N–factor distributions along the cone surface in Fig. 5.26b grow up to the end of the

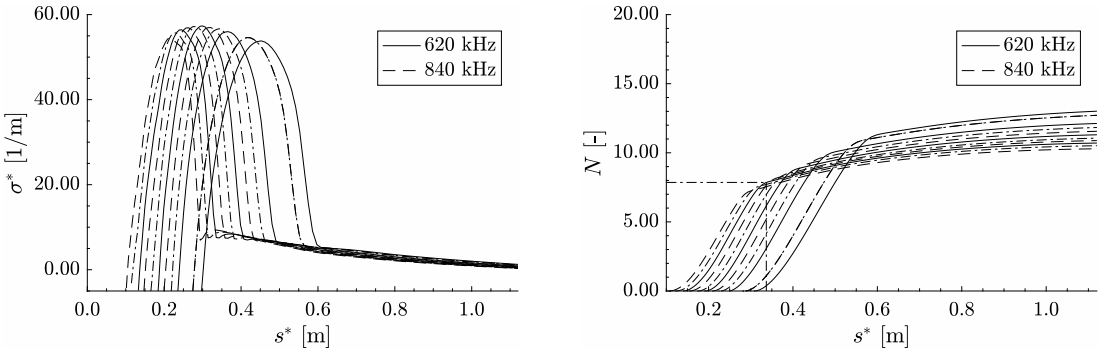

(a) Growth rate distributions

(b) N–factor distributions

Figure 5.26: LST calculations along the arclength of the Shot 4 blunted cone.

geometry. Finally, at the laminar–turbulent transition onset location $x_a^* = 0.353$ m, an N–factor of $N = 7.86$ for a frequency of $f^* = 800$ kHz was found.

Lastly, LPSE calculations were performed for this test case but no satisfactory results were calculated, respectively, non–physically high N–factors were determined for the high disturbance frequencies. This issue likely arose due to the neutral point location close to the blunt nose in the current test case. In case of the LPSE, this neutral point location moves further upstream compared to the LST and, thus, small inaccuracies in the base–flow solution at the junction between the nose and the cone could lead to inaccurate LPSE calculations. Due to this issue, the LPSE results are not presented in this work. Therefore, the comparison with respect to the free–stream Reynolds number in the next section will only be made with regard to the LST results.

5.6 Influence of the Free–Stream Reynolds number on the Boundary–Layer Stability

In this section a comparison between the boundary–layer stability results of the Shot 2 test case in Sec. 5.1 and the Shot 4 test case will be made. Due to the LST calculations at different locations and the absence of a LPSE calculation of the Shot 4 test case, only the LST calculations along the geometry are compared. In Tab. 5.7, the laminar–turbulent transition onset locations, the disturbance frequencies of the most amplified disturbance and the N–factors are shown for the two cases. It can be seen that the N–factor shows a higher value in the Shot 4 test case compared to the Shot 2 case, respectively, for the higher free–stream Reynolds number and nearly the same Mach number and free–stream temperature, at the transition onset location which can be found further upstream compared to the Shot 2 test case. Further, the disturbance frequency also shows a higher value in the Shot 4 case. These greater values are, due to the same geometry and gas model, mainly caused by the higher Reynolds number of the Shot 4 test case which corresponds with the observations of

[83] and [86] outlined in the introduction, namely, the higher disturbance frequencies for the most amplified disturbance and the upstream movement of the transition onset location with an increase of the Reynolds number.

Table 5.7: N–factors at the laminar–turbulent transition onset location for the Shot 2 and Shot 4 test case.

Test case	x_a^* of transition onset [m]	f^* [kHz]	N [-]
Shot 2	0.5325	480	6.15
Shot 4	0.353	800	7.86

Chapter 6

Conclusion and Outlook

The aim of this work was to perform first investigations of the laminar–turbulent transition of a blunted cone in the Mars atmosphere. To perform a comparison and to investigate the influence of the atmosphere on the transition, the calculations were performed in a pure CO_2 environment, in the Mars atmosphere and the Earth atmosphere. Further, a first calculation and investigation on the influence of the free–stream conditions was performed.

To enable the investigations, two solvers were developed and implemented in this work. The first solver is the compressible Navier–Stokes solver CONSST3D. This solver was developed to calculate the laminar base–flow solution which serves as the input flow–field for the boundary–layer stability calculations. As the boundary–layer stability calculations require an adequate base–flow solution with respect not only to the flow variables but also with respect to their spatial first and second derivatives, the focus in the laminar base–flow solver development was in the numerical methods selection and the adequate flow–field calculation. To perform the boundary–layer stability calculations, the second solver COSTAS was developed and implemented. This solver is capable of solving the linear stability theory and the linear parabolized stability equations. Analogous to CONSST3D, the perfect gas and the thermo–chemical equilibrium gas model were implemented into the solver. The latter was additionally implemented, in contrast to, e.g., [24] and [42], to account for the high temperature thermo–chemical effects which have a significant influence in the investigated test cases.

After the successful implementation of the two solvers, two test cases were selected for validation purposes to show the capability of the solvers to accurately calculate the laminar base–flow and the boundary–layer stability. The first test case was the Stetson Mach 8 blunted cone which was chosen for the validation of the solvers in the perfect gas regime. By comparing the current results with results found in literature, a good agreement was observed between the base–flow solutions and the boundary–layer stability results. The second test case for the validation in the thermo–chemical equilibrium gas regime was a Mach 10 flat plate. Also in this case, the base–flow result and the boundary–layer stability result were in good agreement with the numerical results found in literature.

With the validated solvers, thereafter, the boundary–layer stability investigations and comparisons between different atmospheres and free–stream conditions, assuming a gas in thermo–chemical equilibrium, were performed. Therefore, the experimentally and numerically investigated blunted cone in a pure CO_2 atmosphere under the Shot 2 test conditions of Hollis et al. [28] was chosen and calculations in a CO_2 atmosphere, the Mars atmosphere and the Earth atmosphere were performed by requiring similar free-stream conditions. By comparing the base–flow result in the CO_2 atmosphere of this work with the experimental and numerical results of Hollis et al. [28], it was found that the thermo–chemical equilibrium gas model in the current investigations did not reflect the real thermo–chemical effects of the experiment due to the under–prediction of the wall heat flux in the current results. Nevertheless, because a good agreement between the wall pressure distributions along the cone was observed and because currently no thermo–chemical non–equilibrium gas model is implemented in CONSST3D and COSTAS, the investigations in this work were performed with the current numerical implementation of the solvers. Two main observations were made with regard to the base–flow results in this work by comparing the base–flow results in the Mars atmosphere and the Earth atmosphere with the result in the CO_2 atmosphere. Firstly, the additional consideration of the small amount of N_2 in the Mars atmosphere had no significant influence on the non–dimensional wall distributions. Secondly, it was found that the Earth atmosphere significantly increases the non–dimensional wall heat flux and pressure which was concluded to be mainly caused by the consideration of only diatomic gases in the Earth atmosphere in contrast to the additional triatomic CO_2 in the CO_2 atmosphere and the Mars atmosphere. With these calculated base–flow solutions, firstly, the boundary–layer stability calculations were performed by applying the LST around the experimentally measured transition onset location. The results in the CO_2 atmosphere showed an unstable second Mack mode and a stable first mode. Further, an unstable behavior of the disturbances up to high frequencies was found without a conversion to a third mode which could not be observed in the validation test cases. Similar observations with regard to the growth rate were made in the Mars atmosphere test case, whereas the results in the Earth atmosphere showed a different behavior, namely, the growth rate becomes and remains stable for high frequencies. Finally, by comparing the non–dimensional growth rates over the non–dimensional angular frequency at the transition onset location, it was observed that the maximum of the growth rates in the different atmospheres occurred at nearly the same non–dimensional angular frequency. Only the non–dimensional growth rates differ, where the maximum growth rates in the CO_2 atmosphere and the Mars atmosphere showed similar values with a slightly smaller value in the Mars atmosphere but the Earth atmosphere showed a significantly smaller value compared to the other two atmospheres. To investigate the downstream evolution of the disturbances, LST and LPSE calculations were performed along the cone in the different atmospheres. Similar observations compared to the observations of the LST at the transition onset location were made. Firstly, the N–factor at the transition onset location shows similar values for the CO_2 and the Mars atmosphere for the same disturbance frequency of the most amplified distur-

bance, where in this case the CO_2 atmosphere showed slightly smaller values. This is contrary to the values of the growth rate in the LST calculations at the transition onset location and could be caused by small inaccuracies in the base–flow solutions. Secondly, compared to the two other atmospheres, the N–factor of the result in the Earth atmosphere is smaller in the LST and LPSE at a higher disturbance frequency of the most amplified disturbance. Thus, with respect to the boundary–layer stability results, two main conclusions can be formulated. Firstly, due to the similar results in the CO_2 atmosphere and the Mars atmosphere, the experimental investigations of Hollis et al. [28], considering pure CO_2, match the conditions in the Mars atmosphere well. Secondly, the destabilizing effect of the CO_2 atmosphere and the Mars atmosphere compared to the Earth atmosphere by assuming gases in thermo–chemical equilibrium was observed which corresponds to studies found in literature.

Lastly, an investigation on the influence of the free–stream conditions on the boundary–layer stability was performed by calculating the same blunted cone geometry under the Shot 4 free–stream conditions of Hollis et al. [28] in the CO_2 atmosphere. By comparing the LST result with result of the Shot 2 test case, it was found that the maximum value of the disturbance growth rate at approximately the experimentally measured transition onset location showed significantly greater values for the second Mack mode at a higher disturbance frequency. Additionally, in the LST calculations along the cone, a higher N–factor compared to the Shot 2 test case was determined at the transition onset location. The LPSE calculations were not presented in this work because of the unsatisfactory results, respectively, non–physically high N–factors, which likely arose due to the transition onset location close to the nose of the computed geometry and possible small inaccuracies in the flow field at the nose–cone junction. Overall, by comparing these results to the Shot 2 test case, the higher free–stream conditions, mainly the Reynolds number, resulted in higher growth rates and a higher transition onset N–factor, in agreement with observations made by other researchers for the Earth atmosphere.

With respect to the results presented in this work, further investigations can be performed on the current test cases and additional influences can be considered in further studies. Firstly, to validate the appearance of the unstable behavior of the Mack mode up to high frequencies in the pure CO_2 test case and the test case considering the Mars atmosphere, the calculations should be performed with an additional boundary–layer stability solver. Secondly, the test cases in this work could be calculated with a thermo–chemical non–equilibrium gas model to better represent the thermo–chemical effects of the experimental results. Besides further investigations on the actual test case, investigations on the influence parameters of the boundary–layer transition, as outlined in the introduction, could be performed. These investigations could consist of further calculations on the influence of the free–stream parameters, as well as on the nose bluntness, the wall cooling and the angle of attack. Further, the investigations on different free–stream parameters should contain real flight conditions that appear during re–entry maneuvers into the Mars atmosphere. Additionally, the non–linear terms in the parabolized stability equations could be considered in further studies to account for the non–linear effects in the boundary–layer transition.

Bibliography

[1] Anderson, E., Bai, Z., Bischof, S. C., Blackford, S., Demmel, J., Dongarra, J., Du Croz, J., Greenbaum, A., Hammarling, S., McKenney, A., and Sorensen, D. *LAPACK Users' Guide*. 3rd ed. Philadelphia, Pennsylvania: Society for Industrial and Applied Mathematics, 1999.

[2] Anderson, J. D. , Jr. *Hypersonic and High–Temperature Gas Dynamics*. 2nd ed. Reston, Virginia: AIAA, 2006.

[3] Andersson, P., Henningson, D. S., and Hanifi, A. "On a stabilization procedure for the parabolic stability equations". In: *Journal of Engineering Mathematics* 33 (1998), pp. 311–332. DOI: 10.1023/A:1004367704897.

[4] Aris, R. *Vectors, Tensors and the Basic Equations of Fluid Mechanics*. Dover Books on Mathematics. New York: Dover Publications, 1990.

[5] Billig, F. S. "Shock–Wave Shapes around Spherical– and Cylindrical–Nosed Bodies". In: *Journal of Spacecraft and Rockets* 4.6 (1967), pp. 822–823. DOI: 10.2514/3.28969.

[6] Blazek, J. *Computational Fluid Dynamics: Principles and Applications*. 2nd ed. Oxford: Elsevier Science, 2005.

[7] Buelow, P. E. O., Venkateswaran, S., and Merkle, C. L. "Effect of Grid Aspect Ratio on Convergence". In: *AIAA Journal* 32.12 (1994), pp. 2401–2408. DOI: 10.2514/3.12306.

[8] Chang, C.–L. *Langley Stability and Transition Analysis Code (LASTRAC) Version 1.2 User Manual*. NASA TM–2004–213233, 2004.

[9] Chang, C.–L. and Malik, M. R. "Oblique–mode breakdown and secondary instability in supersonic boundary layers". In: *Journal of Fluid Mechanics* 273 (1994), pp. 323–360. DOI: 10.1017/S0022112094001965.

[10] Chang, C.–L., Malik, M. R., Erlebacher, G., and Hussaini, M. Y. "Compressible Stability of Growing Boundary Layers Using Parabolized Stability Equations". In: *22nd Fluid Dynamics, Plasma Dynamics and Lasers Conference*. Honolulu, Hawaii: AIAA, June 1991. DOI: 10.2514/6.1991-1636.

[11] Chang, C.–L., Malik, M. R., and Hussaini, M. Y. "Effects of Shock on the Stability of Hypersonic Boundary Layers". In: *21st Fluid Dynamics, Plasma Dynamics and Lasers Conference*. Seattle, Washington: AIAA, June 1990. DOI: 10.2514/6.1990-1448.

[12] Chang, C.–L., Vinh, H., and Malik, M. R. "Hypersonic Boundary–Layer Stability with Chemical Reactions using PSE". In: *28th Fluid Dynamics Conference*. Snowmass Village, Colorado: AIAA, June 1997. DOI: 10.2514/6.1997-2012.

[13] Ericsson, L. E. "Effect of Nose Bluntness and Cone Angle on Slender–Vehicle Transition". In: *AIAA Journal* 26.10 (1988), pp. 1168–1174. DOI: 10.2514/3.10024.

[14] Esfahanian, V. "Computation and Stability Analysis of Laminar Flow over a Blunt Cone in Hypersonic Flow". PhD thesis. The Ohio State University, 1991.

[15] Esfahanian, V. and Hejranfar, K. "Accuracy of Parabolized Navier–Stokes Schemes for Stability Analysis of Hypersonic Axisymmetric Flows". In: *AIAA Journal* 40.7 (2002), pp. 1311–1322. DOI: 10.2514/2.1820.

[16] Farley, K. A., Williford, K. H., Stack, K. M., Bhartia, R., Chen, A., de la Torre, M., Hand, K., Goreva, Y., Herd, C. D. K., Hueso, R., Liu, Y., Maki, J. N., Martinez, G., Moeller, R. C., Nelessen, A., Newman, C. E., Nunes, D., Ponce, A., Spanovich, N., Willis, P. A., Beegle, L. W., Bell, J. F., Brown, A. J., Hamran, S.–E., Hurowitz, J. A., Maurice, S., Paige, D. A., Rodriguez-Manfredi, J. A., Schulte, M., and Wiens, R. C. "Mars 2020 Mission Overview". In: *Space Science Reviews* 216 (2020), pp. 1–41. DOI: 10.1007/s11214-020-00762-y.

[17] Fasel, H., Thumm, A., and Bestek, H. "Direct numerical simulation of transition in supersonic boundary layers: oblique breakdown". In: *Transitional and Turbulent Compressible Flows - 1993*. American Society of Mechanical Engineers, Fluids Engineering Division (Publication) FED. Publ by ASME, 1993, pp. 77–92.

[18] Fedorov, A. "Transition and Stability of High–Speed Boundary Layers". In: *Annual Review of Fluid Mechanics* 43.1 (2011), pp. 79–95. DOI: 10.1146/annurev-fluid-122109-160750.

[19] Fedorov, A. V., Soudakov, V. G., and Leyva, I. A. "Stability analysis of high–speed boundary–layer flow with gas injection". In: *7th AIAA Theoretical Fluid Mechanics Conference*. Atlanta, Georgia: AIAA, June 2014. DOI: 10.2514/6.2014-2498.

[20] Gao, B. and Park, S. O. "Compressible Parabolized Stability Equation in Curvilinear Coordinate System and Integration". In: *KSAS International Journal* 7.2 (2006), pp. 155–174.

[21] Gordon, S. and McBride, B. J. "Computer Program for Calculation of Complex Chemical Equilibrium Compositions and Applications, I. Analysis". In: *NASA Reference Publication 1311* (1994).

[22] Grotzinger, J. P., Crisp, J., Vasavada, A. R., Anderson, R. C., Baker, C. J., Barry, R., Blake, D. F., Conrad, P., Edgett, K. S., Ferdowski, B., Gellert, R., Gilbert, J. B., Golombek, M., Gómez-Elvira, J., Hassler, D. M., Jandura, L., Litvak, M., Mahaffy, P., Maki, J., Meyer, M., Malin, M. C., Mitrofanov, I., Simmonds, J. J., Vaniman, D., Welch, R. V., and Wiens, R. C. "Mars Science Laboratory Mission and Science Investigation". In: *Space Science Reviews* 170.1 (2012), pp. 5–56.

[23] Harder, R. L. and Desmarais, R. N. "Interpolation Using Surface Splines". In: *Journal of Aircraft* 9.2 (1972), pp. 189–191. DOI: 10.2514/3.44330.

[24] Hein, S. "Nonlinear Nonlocal Transition Analysis". PhD thesis. Universität Stuttgart, 2005.

[25] Herbert, T. "Secondary Instability of Boundary Layers". In: *Annual Review of Fluid Mechanics* 20.1 (1988), pp. 487–526. DOI: 10.1146/annurev.fl.20.010188.002415.

[26] Hirschel, E. H. *Basics of Aerothermodynamics*. Berlin, Heidelberg: Springer, 2005.

[27] Hirschel, E. H. and Kordulla, W. *Shear Flow in Surface–Oriented Coordinates*. Notes on Numerical Fluid Mechanics, vol. 4. Braunschweig: Vieweg, 1981.

[28] Hollis, B. R., Barnhardt, M. D., Maclean, M., Dufrene, A., and Wadhams, T. "Turbulent Aeroheating Measurements on a 7–Deg Cone in High–Enthalpy CO2 Flow". In: *Journal of Thermophysics and Heat Transfer* 33.1 (2019), pp. 216–224.

[29] Hollis, B. R., Liechty, D. S., Wright, M. J., Holden, M. S., Wadhams, T. P., MacLean, M., and Dyakonov, A. "Transition Onset and Turbulent Heating Measurements for the Mars Science Laboratory Entry Vehicle". In: *43rd AIAA Aerospace Sciences Meeting and Exhibit*. Reno, Nevada: AIAA, Jan. 2005. DOI: 10.2514/6.2005-1437.

[30] Hollis, B. R., Prabhu, D. K., Maclean, M., and Dufrene, A. "Blunt–Body Aerothermodynamic Database from High–Enthalpy Carbon–Dioxide Testing in an Expansion Tunnel". In: *Journal of Thermophysics and Heat Transfer* 31.3 (2017), pp. 712–731. DOI: 10.2514/1.T5019.

[31] Hudson, M. L., Chokani, N., and Candler, G. V. "Linear Stability of Hypersonic Flow in Thermochemical Nonequilibrium". In: *AIAA Journal* 35.6 (1997), pp. 958–964. DOI: 10.2514/2.204.

[32] Jewell, J. S. and Kimmel, R. L. "Boundary-Layer Stability Analysis for Stetson's Mach 6 Blunt-Cone Experiments". In: *Journal of Spacecraft and Rockets* 54.1 (2017), pp. 258–265. DOI: 10.2514/1.A33619.

[33] Johnson, C. B., Stainback, P. C., Wicker, K. C., and Boney, L. R. "Boundary–Layer Edge Conditions and Transition Reynolds Number Data for a Flight Test at Mach 20 (Reentry F)". In: *NASA TM X–2584* (1972).

[34] Johnson, H. B. and Candler, G. V. "Hypersonic Boundary Layer Stability Analysis Using PSE–Chem". In: *35th AIAA Fluid Dynamics Conference and Exhibit*. Toronto, Ontario, Canada: AIAA, June 2005. DOI: 10.2514/6.2005-5023.

[35] Johnson, H. B. and Candler, G. V. "PSE Analysis of Reacting Hypersonic Boundary Layer Transition". In: *30th AIAA Fluid Dynamics Conference*. Norfolk, Virginia: AIAA, June 1999. DOI: 10.2514/6.1999-3793.

[36] Johnson, H. B., Candler, G. V., and Wright, M. J. "Boundary Layer Stability Analysis of Mars Science Laboratory Aeroshell". In: *44th AIAA Aerospace Sciences Meeting and Exhibit*. Reno, Nevada: AIAA, Jan. 2006. DOI: 10.2514/6.2006-920.

[37] Kemm, F. "A comparative study of TVD–limiters–well–known limiters and an introduction of new ones". In: *International Journal for Numerical Methods in Fluids* 67.4 (2011), pp. 404–440. DOI: 10.1002/fld.2357.

[38] Kim, K. H., Kim, C., and Rho, O.–H. "Methods for the Accurate Computations of Hypersonic Flows: I. AUSMPW+ Scheme". In: *Journal of Computational Physics* 174.1 (2001), pp. 38–80. DOI: 10.1006/jcph.2001.6873.

[39] Klebanoff, P. S., Tidstrom, K. D., and Sargent, L. M. "The three–dimensional nature of boundary–layer instability". In: *Journal of Fluid Mechanics* 12.1 (1962), pp. 1–34. DOI: 10.1017/S0022112062000014.

[40] Kline, H. L., Chang, C.–L., and Li, F. "Boundary Layer Stability and Transition in a Chemically Reacting Martian Atmosphere using LASTRAC". In: *22nd AIAA International Space Planes and Hypersonics Systems and Technologies Conference*. Orlando, Florida: AIAA, Sept. 2018. DOI: 10.2514/6.2018-5206.

[41] Kline, H. L., Chang, C.–L., and Li, F. "Hypersonic Chemically Reacting Boundary–Layer Stability using LASTRAC". In: *2018 Fluid Dynamics Conference*. Atlanta, Georgia: AIAA, June 2018. DOI: 10.2514/6.2018-3699.

[42] Kufner, E. "Numerische Untersuchungen der Strömungsinstabilitäten an spitzen und stumpfen Kegeln bei hypersonischen Machzahlen". PhD thesis. Universität Stuttgart, 1995.

[43] Kufner, E., Dallmann, U., and Stilla, J. "Instability of Hypersonic Flow Past Blunt Cones - Effects of Mean Flow Variations". In: *23rd Fluid Dynamics, Plasmadynamics, and Lasers Conference*. Orlando, Florida: AIAA, July 1993. DOI: 10.2514/6.1993-2983.

[44] Landmann, B., Haselbacher, A., Chao, J., and Yu, C. "Characteristic Boundary Condtitions for Compressible Viscous Flows on Curvilinear Grids". In: *48th AIAA Aerospace Sciences Meeting Including the New Horizons Forum and Aerospace Exposition*. Orlando, Florida: AIAA, Jan. 2010. DOI: 10.2514/6.2010-1084.

[45] Lee, J.–H. *Hypersonic Three–Dimensional Nonequilibrium Boundary–Layer Equations in Generalized Curvilinear Coordinates*. NASA Contractor Report 185677, 1993.

[46] Leyva, I. A., Laurence, S., Beierholm, A. W.–K., Hornung, H. G., Wagnild, R., and Candler, G. "Transition delay in hypervelocity boundary layers by means of CO2/acoustic instability interactions". In: *47th AIAA Aerospace Sciences Meeting including The New Horizons Forum and Aerospace Exposition*. Orlando, Florida: AIAA, Jan. 2009. DOI: 10.2514/6.2009-1287.

[47] Li, F. and Malik, M. R. "Mathematical Nature of Parabolized Stability Equations". In: *Laminar–Turbulent Transition*. Ed. by Kobayashi, R. Berlin, Heidelberg: Springer, 1995, pp. 205–212.

[48] Li, F. and Malik, M. R. "On the Nature of PSE Approximation". In: *Theoretical and Computational Fluid Dynamics* 8 (1996), pp. 253–273. DOI: 10.1007/BF00639695.

[49] Liang, X., Li, X., Fu, D., and Ma, Y. "Effects of wall temperature on boundary layer stability over a blunt cone at Mach 7.99". In: *Computers & Fluids* 39.2 (2010), pp. 359–371. DOI: 10.1016/j.compfluid.2009.09.015.

[50] Liou, M.–S. "A sequel to AUSM, Part II: AUSM+–up for all speeds". In: *Journal of Computational Physics* 214.1 (2006), pp. 137–170. DOI: 10.1016/j.jcp.2005.09.020.

[51] Liou, M.–S. "A Sequel to AUSM: AUSM+". In: *Journal of Computational Physics* 129.2 (1996), pp. 364–382. DOI: 10.1006/jcph.1996.0256.

[52] Luo, H, Baum, J. D., and Löhner, R. "A Fast, Matrix-free Implicit Method for Compressible Flows on Unstructured Grids". In: *Journal of Computational Physics* 146.2 (1998), pp. 664–690. DOI: 10.1006/jcph.1998.6076.

[53] Mack, L. M. "Boundary–Layer Linear Stability Theory". In: *Special course on stability and transition of laminar flow, AGARD Report* 709 (1984).

[54] Malik, M. R. "Hypersonic Flight Transition Data Analysis Using Parabolized Stability Equations with Chemistry Effects". In: *Journal of Spacecraft and Rockets* 40.3 (2003), pp. 332–344. DOI: 10.2514/2.3968.

[55] Malik, M. R. "Numerical Methods for Hypersonic Boundary Layer Stability". In: *Journal of Computational Physics* 86.2 (1990), pp. 376–413. DOI: 10.1016/0021-9991(90)90106-B.

[56] Malik, M. R. and Anderson, E. C. "Real gas effects on hypersonic boundary-layer stability". In: *Physics of Fluids A: Fluid Dynamics* 3.5 (1991), pp. 803–821. DOI: 10.1063/1.858012.

[57] Malik, M. R., Spall, R. E., and Chang, C.–L. "Effect of Nose Bluntness on Boundary Layer Stability and Transition". In: *28th Aerospace Sciences Meeting*. Reno, Nevada: AIAA, Jan. 1990. DOI: 10.2514/6.1990-112.

[58] Marxen, O., Magin, T., Iaccarino, G., and Shaqfeh, E. S. G. "A high–order numerical method to study hypersonic boundary–layer instability including high–temperature gas effects". In: *Physics of Fluids* 23.8 (2011). DOI: 10.1063/1.3614526.

[59] McBride, B. J., Zehe, M. J., and Gordon, S. *NASA Glenn Coefficients for Calculating Thermodynamic Properties of Individual Species*. NASA/TP–2002–211556, 2002.

[60] Mohamed, K. and Paraschivoiu, M. "Real Gas Numerical Simulation of Hydrogen Flows". In: *2nd International Energy Conversion Engineering Conference*. Providence, Rhode Island: AIAA, Aug. 2004. DOI: 10.2514/6.2004-5607.

[61] Moretti, G. and Abbett, M. "A Time–Dependent Computational Method for Blunt Body Flows". In: *AIAA Journal* 4.12 (1966), pp. 2136–2141. DOI: 10.2514/3.3867.

[62] Mortensen, C. H. "Effects of Thermochemical Nonequilibrium on Hypersonic Boundary–Layer Instability in the Presence of Surface Ablation or Isolated Two–Dimensional Roughness". PhD thesis. University of California, Los Angeles, 2015.

[63] Mortensen, C. H. and Zhong, X. "Real–Gas and Surface–Ablation Effects on Hypersonic Boundary–Layer Instability over a Blunt Cone". In: *AIAA Journal* 54.3 (2016), pp. 976–994. DOI: 10.2514/1.J054404.

[64] Mundt, Ch., Keraus, R., and Fischer, J. "New, accurate, vectorized approximations of state surfaces for the thermodynamic and transport properties of equilibrium air". In: *Zeitschrift für Flugwissenschaften und Weltraumforschung* 15 (1991), pp. 179–184.

[65] Obayashi, S. and Guruswamy, G. P. "Convergence Acceleration of a Navier–Stokes Solver for Efficient Static Aeroelastic Computations". In: *AIAA Journal* 33.6 (1995), pp. 1134–1141. DOI: 10.2514/3.12533.

[66] Palmer, G. and Venkatapathy, E. "Effective Treatment of the Singular Line Boundary Problem for Three–Dimensional Grids". In: *AIAA Journal* 31.10 (1993), pp. 1757–1758. DOI: 10.2514/3.11845.

[67] Panaras, A. G. *Boundary–Layer Equations in Generalized Curvilinear Coordinates*. NASA TM–100003, 1987.

[68] Pfitzner, M. "A 3–D Non–Equilibrium Shock–Fitting Algorithm Using Effective Rankine–Hugoniot Relations". In: *22nd Fluid Dynamics, Plasma Dynamics and Lasers Conference*. Honolulu, Hawaii: AIAA, June 1991. DOI: 10.2514/6.1991-1467.

[69] Pinna, F. "Numerical study of stability of flows from low to high Mach number". PhD thesis. Universitá "La Sapienza" di Roma, 2015.

[70] Pinna, F. and Groot, K. J. "Automatic Derivation of Stability Equations in Arbitrary Coordinates and Different Flow Regimes". In: *44th AIAA Fluid Dynamics Conference*. Atlanta, Georgia: AIAA, June 2014. DOI: 10.2514/6.2014-2634.

[71] Pletcher, R. H., Tannehill, J. C., and Anderson, D. A. *Computational Fluid Mechanics and Heat Transfer*. 3rd ed. Boca Raton: CRC Press, Taylor & Francis Group, 2013.

[72] Poinsot, T. J. and Lele, S. K. "Boundary Conditions for Direct Simulations of Compressible Viscous Flows". In: *Journal of Computational Physics* 101.1 (1992), pp. 104–129. DOI: 10.1016/0021-9991(92)90046-2.

[73] Rawat, P. S. and Zhong, X. "On high–order shock–fitting and front–tracking schemes for numerical simulation of shock—disturbance interactions". In: *Journal of Computational Physics* 229.19 (2010), pp. 6744–6780. DOI: 10.1016/j.jcp.2010.05.021.

[74] Riedelbauch, S. "Aerothermodynamische Eigenschaften von Hyperschallströmungen über strahlungsadiabate Oberflächen". PhD thesis. Technische Universität München, 1991.

[75] Roe, P. L. "Characteristic–Based Schemes for the Euler Equations". In: *Annual Review of Fluid Mechanics* 18.1 (1986), pp. 337–365. DOI: 10.1146/annurev.fl.18.010186.002005.

[76] Rosenboom, I., Hein, S., and Dallmann, U. "Influence of Nose Bluntness on Boundary–Layer Instabilities in Hypersonic Cone Flows". In: *30th Fluid Dynamics Conference*. Norfolk, Virginia: AIAA, June 1999. DOI: 10.2514/6.1999-3591.

[77] Schlichting, H. and Gersten, K. *Grenzschicht–Theorie*. 10th ed. Berlin, Heidelberg: Springer, 2006. DOI: 10.1007/3-540-32985-4.

[78] Schneider, S. P. *Lecture notes of A&AE 624, Laminar-Turbulent Transition*. School of Aeronautics and Astronautics, Purdue University, 2016.

[79] Schrauf, G. "An efficient solver of the eigenvalue problem of the linear stability equations for three dimensional, compressible boundary–layer flows". In: *DGLR–Bericht* 88-05 (1988), pp. 27–38.

[80] Simen, M. "Local and Non–Local Stability Theory of Spatially Varying Flows". In: *Instability, Transition, and Turbulence. ICASE NASA LaRC Series*. Ed. by Hussaini, M. Y., Kumar, A., and Streett, C. L. New York, NY: Springer New York, 1992, pp. 181–201. DOI: 10.1007/978-1-4612-2956-8_18.

[81] Smith, A. M. O. and Gamberoni, N. *Transition, Pressure Gradient and Stability Theory*. El Segundo, California: Douglas Aircraft Co. Rep. ES 26388, 1956.

[82] Softley, E. J., Graber, B. C., and Zempel, R. E. "Experimental Observation of Transition of the Hypersonic Boundary Layer". In: *AIAA Journal* 7.2 (1969), pp. 257–263. DOI: 10.2514/3.5083.

[83] Stainback, P. C. *Effect of unit Reynolds number, nose bluntness, angle of attack, and roughness on transition on a 5° half–angle cone at Mach 8.* NASA TN D–4961, 1969.

[84] Stetson, K. F., Thompson, E. R., Donaldson, J. C., and Siler, L. G. "Laminar Boundary Layer Stability Experiments on a Cone at Mach 8, Part 1: Sharp Cone". In: *16th Fluid and Plasmadynamics Conference*. Danvers, Massachusetts: AIAA, July 1983. DOI: 10.2514/6.1983-1761.

[85] Stetson, K. F., Thompson, E. R., Donaldson, J. C., and Siler, L. G. "Laminar Boundary Layer Stability Experiments on a Cone at Mach 8, Part 2: Blunt Cone". In: *AlAA 22nd Aerospace Sciences Meeting*. Reno, Nevada: AIAA, Jan. 1984. DOI: 10.2514/6.1984-6.

[86] Stetson, K. F., Thompson, E. R., Donaldson, J. C., and Siler, L. G. "Laminar Boundary Layer Stability Experiments on a Cone at Mach 8, Part 4: On Unit Reynolds Number and Environmental Effects". In: *4th Joint Fluid Mechanics, Plasma Dynamics and Lasers Conference*. Atlanta, Georgia: AIAA, May 1986. DOI: 10.2514/6.1986-1087.

[87] Stetson, K. F., Thompson, E. R., Donaldson, J. C., and Siler, L. G. "Laminar Boundary Layer Stability Experiments on a Cone at Mach 8. Part 5: Tests with a Cooled Model". In: *20th Fluid Dynamics, Plasma Dynamics and Lasers Conference*. Buffalo, New York: AIAA, June 1989. DOI: 10.2514/6.1989-1895.

[88] Stilla, J. "Engineering Transition Prediction for a Hypersonic Axisymmetric Boundary Layer". In: *Journal of Aircraft* 31.6 (1994), pp. 1358–1364. DOI: 10.2514/3.46659.

[89] Stuckert, G. and Reed, H. L. "Linear Disturbances in Hypersonic, Chemically Reacting Shock Layers". In: *AIAA Journal* 32.7 (1994), pp. 1384–1393. DOI: 10.2514/3.12206.

[90] Teschner, F. and Mundt, Ch. "Fully conservative overset mesh to overcome the blunt body metric singularity in finite difference methods". In: *Shock Waves* 32 (2022), pp. 295–312. DOI: 10.1007/s00193-022-01078-2.

[91] Teschner, F. and Mundt, Ch. "Investigations of the Laminar-Turbulent Boundary-Layer Transition of a Blunted Cone in the Mars Atmosphere". In: *2nd International Conference on Flight Vehicles, Aerothermodynamics and Re-entry Missions & Engineering (FAR)*. Heilbronn, Germany: ESA, June 2022.

[92] Teschner, F. and Mundt, Ch. "Numerical Boundary-Layer Stability Unstable First Mode Detection for the Reentry-F Cone". In: *Journal of Spacecraft and Rockets* 60.2 (2023), pp. 427–436. DOI: 10.2514/1.A35467.

[93] Thompson, K. W. "Time Dependent Boundary Conditions for Hyperbolic Systems". In: *Journal of Computational Physics* 68.1 (1987), pp. 1–24. DOI: 10.1016/0021-9991(87)90041-6.

[94] Tisseur, F. and Meerbergen, K. "The Quadratic Eigenvalue Problem". In: *SIAM Review* 43.2 (2001), pp. 235–286.

[95] U.S. Congress. *S.442 - 115th Congress (2017-2018): National Aeronautics and Space Administration Transition Authorization Act of 2017*. https://www.congress.gov/bill/115th-congress/senate-bill/442 (2022-18-07).

[96] van Albada, G. D., van Leer, B., and Roberts, W. W., Jr. "A Comparative Study of Computational Methods in Cosmic Gas Dynamics". In: *Upwind and High–Resolution Schemes*. Ed. by Hussaini, M. Y., van Leer, B., and Van Rosendale, J. Berlin, Heidelberg: Springer, 1997, pp. 95–103. DOI: 10.1007/978-3-642-60543-7_6.

[97] Van Ingen, J. L. *A Suggested Semi-Empirical Method for the Calculation of the Boundary Layer Transition Region*. Delft: Delft University of Technology, Aerospace Engineering, Report VTH-74, 1956.

[98] Vinokur, M. "On One–Dimensional Stretching Functions for Finite–Difference Calculations". In: *Journal of Computational Physics* 50.2 (1983), pp. 215–234. DOI: 10.1016/0021-9991(83)90065-7.

[99] Wagnild, R. M., Candler, G. V., Leyva, I. A., Jewell, J. S., and Hornung, H. G. "Carbon Dioxide Injection for Hypervelocity Boundary Layer Stability". In: *48th AIAA Aerospace Sciences Meeting Including the New Horizons Forum and Aerospace Exposition*. Orlando, Florida: AIAA, Jan. 2010. DOI: 10.2514/6.2010-1244.

[100] White, F. M. *Viscous Fluid Flow*. 3rd ed. New York: McGraw–Hill, 2006.

[101] Whitfield, D. L. and Janus, J. M. "Three–Dimensional Unsteady Euler Equations Solution Using Flux Vector Splitting". In: *17th Fluid Dynamics, Plasma Dynamics, and Lasers Conference*. Snowmass, Colorado: AIAA, June 1984. DOI: 10.2514/6.1984-1552.

[102] Yee, H. C. *On the Implementation of a Class of Upwind Schemes for System of Hyperbolic Conservation Laws*. NASA TM–86839, 1985.

[103] Yoon, S. and Jameson, A. "Lower–Upper Symmetric–Gauss–Seidel Method for the Euler and Navier–Stokes Equations". In: *AIAA Journal* 26.9 (1988), pp. 1025–1026. DOI: 10.2514/3.10007.

[104] Zanus, L., Miró Miró, F., and Pinna, F. "Parabolized stability analysis of chemically reacting boundary–layer flows in equilibrium conditions". In: *Proceedings of the Institution of Mechanical Engineers, Part G: Journal of Aerospace Engineering* 234.1 (2020), pp. 79–95. DOI: 10.1177/0954410019839894.

[105] Zhong, X. and Ma, Y. "Boundary–layer receptivity of Mach 7.99 flow over a blunt cone to free–stream acoustic waves". In: *Journal of Fluid Mechanics* 556 (2006), pp. 55–103. DOI: 10.1017/S0022112006009293.

Appendix A

Inviscid Flux Jacobians

A.1 Perfect Gas

The inviscid flux Jacobians in the perfect gas case for the implicit terms of the LU-SGS scheme are defined by

$$A,B,C = J^{-1}\begin{bmatrix} 0 & k_x & k_y & k_z & 0 \\ k_x\frac{\gamma-1}{2}|V|^2 - uv_k & k_x(2-\gamma)u + v_k & k_yu - k_x(\gamma-1)v & k_zu - k_x(\gamma-1)w & k_x(\gamma-1) \\ k_y\frac{\gamma-1}{2}|V|^2 - vv_k & k_xv - k_y(\gamma-1)u & k_y(2-\gamma)v + v_k & k_zv - k_y(\gamma-1)w & k_y(\gamma-1) \\ k_z\frac{\gamma-1}{2}|V|^2 - wv_k & k_xw - k_z(\gamma-1)u & k_yw - k_z(\gamma-1)v & k_z(2-\gamma)w + v_k & k_z(\gamma-1) \\ \left(2\frac{\gamma-1}{2}|V|^2 - \frac{\gamma e}{\rho}\right)v_k & k_x\left(\frac{\gamma e}{\rho} - \frac{\gamma-1}{2}|V|^2\right) - (\gamma-1)uv_k & k_y\left(\frac{\gamma e}{\rho} - \frac{\gamma-1}{2}|V|^2\right) - (\gamma-1)vv_k & k_z\left(\frac{\gamma e}{\rho} - \frac{\gamma-1}{2}|V|^2\right) - (\gamma-1)wv_k & \gamma v_k \end{bmatrix}, \tag{A.1}$$

where $|V|^2 = u^2 + v^2 + w^2$, $v_k = k_xu + k_yv + k_zw$ and $k = \xi$, ζ, η depending on the respective flux [101].

A.2 Thermo-Chemical Equilibrium

In case of calculations in thermo–chemical equilibrium, the inviscid flux Jacobians for the implicit terms of the LU-SGS scheme read

$$A,B,C = J^{-1}\begin{bmatrix} 0 & k_x & k_y & k_z & 0 \\ k_x\left(c^2-\frac{\partial p/\partial\epsilon}{\rho}\left(H_t-|V|^2\right)\right)-uv_k & k_x\left(u-\frac{u\partial p/\partial\epsilon}{\rho}\right)+v_k & k_yu-k_x\frac{v\partial p/\partial\epsilon}{\rho} & k_zu-k_x\frac{w\partial p/\partial\epsilon}{\rho} & k_x\frac{\partial p/\partial\epsilon}{\rho} \\ k_y\left(c^2-\frac{\partial p/\partial\epsilon}{\rho}\left(H_t-|V|^2\right)\right)-vv_k & k_xv-k_y\frac{u\partial p/\partial\epsilon}{\rho} & k_y\left(v-\frac{v\partial p/\partial\epsilon}{\rho}\right)+v_k & k_zv-k_y\frac{w\partial p/\partial\epsilon}{\rho} & k_y\frac{\partial p/\partial\epsilon}{\rho} \\ k_z\left(c^2-\frac{\partial p/\partial\epsilon}{\rho}\left(H_t-|V|^2\right)\right)-wv_k & k_xw-k_z\frac{u\partial p/\partial\epsilon}{\rho} & k_yw-k_z\frac{v\partial p/\partial\epsilon}{\rho} & k_z\left(w-\frac{w\partial p/\partial\epsilon}{\rho}\right)+v_k & k_z\frac{\partial p/\partial\epsilon}{\rho} \\ \left(\left(c^2-H_t\right)-\frac{\partial p/\partial\epsilon}{\rho}\left(H_t-|V|^2\right)\right)v_k & k_xH_t-\frac{u\partial p/\partial\epsilon}{\rho}v_k & k_yH_t-\frac{v\partial p/\partial\epsilon}{\rho}v_k & k_zH_t-\frac{w\partial p/\partial\epsilon}{\rho}v_k & \left(1+\frac{\partial p/\partial\epsilon}{\rho}\right)v_k \end{bmatrix}, \quad \text{(A.2)}$$

where $|V|^2 = u^2 + v^2 + w^2$, $v_k = k_x u + k_y v + k_z w$ and $k = \xi$, ζ, η depending on the respective flux [60].

Appendix B

Transformation Matrices between the Conservative and the Primitive State Vector

B.1 Perfect Gas

In case of a perfect gas, the matrix describing the derivative of the primitive variables with respect to the conservative variables is given by

$$\boldsymbol{M}^{-1} = \frac{\partial \mathbf{q}}{\partial \mathbf{Q}} \begin{bmatrix} 1 & 0 & 0 & 0 & 0 \\ -\frac{u}{\rho} & \frac{1}{\rho} & 0 & 0 & 0 \\ -\frac{v}{\rho} & 0 & \frac{1}{\rho} & 0 & 0 \\ -\frac{w}{\rho} & 0 & 0 & \frac{1}{\rho} & 0 \\ \frac{\gamma-1}{2}|V|^2 & -(\gamma-1)u & -(\gamma-1)v & -(\gamma-1)w & \gamma-1 \end{bmatrix} \tag{B.1}$$

[44].

B.2 Thermo-Chemical Equilibrium

In case of calculations considering a thermo–chemical equilibrium gas model the matrix is given by

$$\boldsymbol{M}^{-1} = \frac{\partial \mathbf{q}}{\partial \mathbf{Q}} \begin{bmatrix} 1 & 0 & 0 & 0 & 0 \\ -\frac{u}{\rho} & \frac{1}{\rho} & 0 & 0 & 0 \\ -\frac{v}{\rho} & 0 & \frac{1}{\rho} & 0 & 0 \\ -\frac{w}{\rho} & 0 & 0 & \frac{1}{\rho} & 0 \\ c^2 + \frac{\partial p/\partial \epsilon}{\rho}(|V|^2 - H_t) & -\frac{\partial p/\partial \epsilon}{\rho}u & -\frac{\partial p/\partial \epsilon}{\rho}v & -\frac{\partial p/\partial \epsilon}{\rho}w & \frac{\partial p/\partial \epsilon}{\rho} \end{bmatrix} \tag{B.2}$$

[60]. In both cases $|V|^2 = u^2 + v^2 + w^2$.